Automated determination of crystal orientations from electron backscattering patterns

Lassen, Niels Christian Krieger; Conradsen, Knut; Juul Jensen, Dorte

Publication date:
1994

Document Version
Publisher's PDF, also known as Version of record

Automated Determination of Crystal Orientations from Electron Backscattering Patterns

Niels Christian Krieger Lassen

Lyngby 1994

IMM-PHD-1994-3

IMM

ISSN 0909-3192

Trykt af IMM - DTU
Bogbinder Hans Meyer

Parts of the work presented in this thesis have previously been published in:

Krieger Lassen, N. C., Juul Jensen, D. & Conradsen, K. (1992). Image processing procedures for analysis of electron back scattering patterns. *Scanning Microscopy*, **6**, pp.115-121.

Krieger Lassen, N. C. (1992). Automatic crystal orientation determination from EBSPs. *Micron and Microscopica Acta*, **23**, pp.191-192.

Krieger Lassen, N. C. & Juul Jensen D. (1993). Automatic local texture measurements by EBSP. *Materials Science Forum*, **113-115**, pp.679-684.

Krieger Lassen, N. C. & Bilde-Sørensen, J. B. (1993). Calibration of an electron back-scattering pattern set-up. *Journal of Microscopy*, **170**, pp.125-129.

Krieger Lassen, N. C., Juul Jensen, D. & Conradsen, K. (1993). Automatic recognition of deformed and recrystallized regions in partly recrystallized samples using electron back scattering patterns. *ICOTOM 10*, Ed. H. J. Bunge, in press.

Krieger Lassen, N. C., Juul Jensen, D. & Conradsen, K. (1994). On the statistical analysis of orientation data. *Acta Crystallographica* A, accepted for publication.

Preface

This thesis has been prepared at the Materials Department, Risø National Laboratory, and at the Institute of Mathematical Modelling, the Technical University of Denmark, in partial fulfillment of the requirements for the degree of Doctor of Philosophy in engineering.

The main focus of the work presented in this thesis is on the development of a fully automated system for measuring local lattice orientations in polycrystalline materials using electron backscattering patterns. Methodology and nomenclature from scientific fields such as mathematical statistics, digital image processing, materials science, and crystallography are applied in the thesis to a varying degree. It is implied that the reader has a basic knowledge of at least some of these areas.

Lyngby, June 1994

Niels Christian Krieger Lassen

Acknowledgements

The author would like to express his sincere appreciation to Dr. Dorte Juul Jensen and Professor Knut Conradsen for their encouraging and extremely competent guidance during the course of this work. I am also grateful for the excellent research facilities provided at the Materials Department by Dr. Niels Hansen and at the Institute of Mathematical Modelling by Professor Knut Conradsen.

I wish to thank my colleagues at the Materials Department of Risø for contributing to a pleasant and inspiring scientific and social environment. In particular, I am grateful to Dr. Jørgen B. Bilde-Sørensen for excellent guidance, helpful discussions and engaging collaboration on the development of the calibration routine.

I would also like to thank my colleagues at the Image Analysis Group of the Institute of Mathematical Modelling for providing inspiration and being extremely helpful. In particular, I wish to express my gratitude to Dr. Jens Michael Carstensen for his guidance and good fellowship and to Dr. Michael Grunkin and Dr. Rasmus Larsen for inspiration and pleasant collaboration.

Finally, I want to acknowledge the Danish Research Academy and the Risø National Laboratory for providing me with financial support and equipment to accomplish this project.

Summary

The electron backscattering pattern (EBSP) technique is widely accepted as being an extremely powerful tool for measuring the crystallographic orientation of individual crystallites in polycrystalline materials. Procedures which allow crystal orientations to be calculated on the basis of the position of the bands or the zone axes of EBSPs have existed for several years now. Until recently, however, the localization of either the bands or the zone axes of EBSPs has required the valuable time and attention of a human operator, thus obviously limiting the amounts of orientation data that can be collected by this method.

This thesis describes the development and implementation of a system which enables crystallographic orientations to be obtained fully automatically through the use of computerized analysis and interpretation of EBSPs. More specifically, this thesis will describe the design of a pattern recognition procedure which enables 8 to 12 bands to be localized in typical EBSPs from a modern system. It will be described, how these automatically localized bands can be indexed and used for optimal estimation of the unknown crystal orientations.

A necessary prerequisite for precise determination of crystallographic orientations from EBSPs is accurate knowledge of three calibration parameters which describe the position of the point from which the patterns are emitted relative to the phosphor screen on which they are recorded. This thesis will describe a novel method by which these calibration parameters can be estimated with high precision.

The quality of EBSPs provides important information about the reliability of the measured crystal orientations and about the perfection of the lattice in which the pattern is generated. A measure which allows the quality

of EBSPs to be evaluated quantitatively is therefore described.

Presently, little is known about the uncertainty of the lattice orientations which can be measured from EBSPs. This subject will be discussed in detail in this thesis. With the application of newly developed statistical methods for analyzing orientation data it will be shown how the relative precision of lattice orientations measured from EBSPs can be described. By applying this methodology to a large number of EBSPs of varying quality it is demonstrated that the precision of automatically measured crystal orientations is comparable to the precision obtained, when the positions of four to five bands are supplied by an experienced and careful operator.

Resumé

Den såkaldte "electron backscattering pattern" (EBSP) teknik er almindeligt anerkendt som en meget slagkraftig metode til bestemmelse af den krystallografiske orientering af de enkelte krystaller i polykrystallinske materialler. Procedurer, der muliggør bestemmelsen af krystalorienteringer på basis af positionerne af båndene eller zoneakserne i diffraktionsmønstrene, har eksisteret i flere år. Indtil for nylig har lokaliseringen af enten båndene eller zoneakserne i EBSP mønstrene imidlertidigt været varetaget af en optrænet operatør, hvilket har sat naturlige begrænsninger for den mængde af krystalorienterings data, der har kunnet opsamles med denne teknik.

Denne afhandling beskriver udviklingen og implementeringen af et system, der ved hjælp af en fuldstænding computerstyret analyse og fortolkning af de digitaliserede EBSP billeder, muliggør fuldautomatisk bestemmelse af krystallografiske orienteringer. Mere specifikt, vil der i denne afhandling blive beskrevet en mønstergenkendelsesprocedure, der er i stand til at lokalisere fra 8 til 12 bånd i typiske EBSP billeder fra et moderne system. Det vil blive beskrevet, hvordan disse automatisk lokaliserede bånd kan indiceres, og hvorledes den ukendte krystallografiske orientering herefter kan estimeres optimalt.

En nødvendig forudsætning for at opnå en præcis bestemmelse af krystalorienteringer fra EBSP billeder er adgangen til præcise estimater af tre kalibreringsparametre, der beskriver positionen af det punkt, hvorfra diffraktionsmønstret stammer i forhold til den fosforskærm, hvorpå det er blevet registreret. Denne afhandling vil beskrive en helt ny metode, hvorved disse tre kalibreringsparametre kan estimeres med høj præcision.

Kvaliteten af EBSP billederne indeholder vigtig information om pålideligheden af de målte krystalorienteringer og om graden af perfektion

af det krystalgitter, hvori diffraktionsmønstret er blevet genereret. Et mål, der tilvejebringer et kvantitativt mål for kvaliteten af EBSP billeder, er derfor beskrevet i denne afhandling.

På nærværende tidspunkt vides der kun lidt om den præcision, hvormed krystalorienteringer kan bestemmes eller rettere måles på basis af EBSP billeder. Præcisionen af EBSP teknikken vil derfor blive diskuteret indgående i denne afhandling. Ved anvendelse af nyligt udviklede statistiske metoder til analyse af orienteringsdata, vil det her blive vist, hvorledes den relative præcision af krystalorienteringer målt fra EBSP billeder kan beskrives. Denne præcisionsbeskrivelse er blevet anvendt på et stort antal diffraktionsmønstre af varierende kvalitet, og det vil blive demonstreret, at præcisionen af automatisk målte krystalorienteringer er sammenlignelig med den præcision, der kan opnås, når fire til fem bånd bliver omhyggeligt lokaliseret af en erfaren og omhyggelig operatør.

Contents

Chapter 1

Introduction

Many materials of great technological importance, notably metals and ceramics, are polycrystalline. It has long been known that the properties and behavior of polycrystals are strongly dependent on the orientation and arrangement of the individual crystallites within the polycrystalline aggregate. When all possible crystallite orientations do not occur with the same frequency, and one or several preferred orientations exist, the polycrystalline material is said to have a *texture*. Since many of the properties of single crystals are directionally dependent, there exists a strong correlation between texture and polycrystal properties. Knowledge of this correlation has made it possible, to some extent, to tailor material properties for specific needs, by controlling the texture of the material through appropriate processing.

Texture is well quantified using the orientation distribution function (ODF), which describes the volume fraction of crystals with a specific orientation. The ODF is traditionally calculated from pole figures, determined experimentally by x-ray or neutron diffraction, and thus obtained from tens of thousands of crystallites. While the ODF has been quite successful in describing the correlation between texture and properties it also has a serious limitation. It contains no information about the spatial arrangement of the crystallites and the intercrystalline structure of the material. To further the understanding of the macroscopic effects of texture, it is necessary to obtain

this spatial information and determine what is know as the *microtexture*: Spatially specific texture measured on an individual orientation basis. The possibility to measure the orientation of individual crystals, the microtexture, obviously allows a much more detailed image of the polycrystal to be obtained than the *macrotexture* described through the ODF. Not only will this more detailed image further the understanding of correlations between texture and polycrystal properties, but it is likely also to greatly improve the understanding of phenomena such as recrystallization, recovery and grain growth. The ability to directly link features of the microstructure, such as grain shape and size, with grain orientation, is extremely useful in the studies of the aforementioned phenomena. Furthermore, in studies of the relationship between neighboring grains, sometimes referred to as the *mesotexture*, and grain boundary geometry, it is essential to be able to measure the microtexture.

There are currently several techniques available for measuring the orientation of individual crystallites, though only three or four of them are frequently used. These techniques are all based on the diffraction of either x-rays or electrons. For overviews, the reader is referred to Randle (1992), Juul Jensen (1993), Schwarzer (1990), Humphreys (1988) and Dingley (1981). The techniques based on x-rays, the back-reflection Laue method and the micro Kossel x-ray diffraction (MKXD) technique, all suffer from poor spatial resolution (~10μm), slow recording of the diffraction pattern, and require specialized equipment, but offer instead a relatively low sensitivity to lattice imperfections and a high precision of the measured orientations. The microtexture techniques based on electron diffraction are by far the most widely used, partly because electrons are easier to focus than x-rays. In the transmission electron microscope (TEM) the techniques based on Kikuchi diffraction patterns, the micro diffraction (MD) and convergent beam electron diffraction (CBED) techniques offer a very good spatial resolution (~10nm for MD, ~1nm for CBED), a low sensitivity to strain and high precision orientation measurements. However, the TEM-based techniques all suffer from complicated and tedious specimen preparation and offer only a very small sample area which greatly limits the number of crystal orientations that can be collected from the microstructure (the problem regarding the small sample area may partly be overcome in the future with the development of

new specimen preparation techniques; Klepeis, Benedict & Anderson, 1988). These drawbacks are not, to the same extent, found in the microtexture techniques that are available in the scanning electron microscope (SEM). The selected area channeling pattern (SACP) technique, which suffers from a rather poor spatial resolution (~30μm; ~5μm using dynamic focusing), was previously quite widely used, but it is now largely being superseded by the electron backscattering pattern (EBSP) technique. The main advantages of the EBSP technique, in comparison with the SACP technique, are a much better spatial resolution (~0.5μm), easier specimen preparation, smaller sensitivity to crystal imperfections (the dislocation density) and a diffraction pattern which is easier to interpret because of a larger angular coverage.

The EBSP technique is now widely accepted as being the most powerful method for measuring microtexture. Its main advantages are shortly summarized below:

- High spatial resolution (~0.5μm)
- High precision of measured orientations (~0.5°)
- Large sample area of bulk specimen (~100mm^2)
- Concurrent microstructure imaging possible
- Fairly uncomplicated specimen preparation
- Rapid measurements of crystal orientations through on-line analysis

In 1987, Dingley and co-workers introduced an on-line computer-assisted method for obtaining crystal orientations from EBSPs (Dingley, Longden, Weinbren & Alderman, 1987). Even though this semi-automatic technique, and similar ones developed later (Schmidt, Bilde-Sørensen & Juul Jensen, 1991) provides a rapid and convenient means for measuring microtexture, the need for a trained operator puts restrictions on the amount of data which can be obtained. For many types of investigations, it is necessary to measure the orientation of several hundreds or even thousands of crystallites in order to get statistical reliability. In such cases, there is an obvious need for a fully automatic procedure which replaces the operator by a computer. Even in cases where the type of investigation requires operator involvement (for example when studying a partly recrystallized sample) it is extremely convenient to let

a computer take care of all the calculations.

The work presented in this thesis was initiated by a desire to develop a fully automated system for measuring microtexture on the basis of EBSPs. In a semi-automatic system the operator must perform the following three tasks:

A. Move the stage or the electron beam to the desired location
B. Localize the bands in the digitized EBSP
C. Check the proposed band indexing

Thus, to obtain a fully automatic system, procedures which will allow a computer to perform these three tasks must be developed. While it is fairly easy to make the computer control a motorized stage (task A above), task B is far more difficult for a computer to perform, and requires the development of appropriate pattern recognition procedures. In a semi-automatic system for analyzing EBSPs, the operator has the important task of checking the proposed band indexing. In order to make the computer perform this task, it is necessary to modify the indexing techniques that are used in semi-automatic systems.

The following chapters of this thesis will describe the development, implementation and evaluation of a fully automated system for EBSP analysis. In chapter 2 the EBSP technique is described, including its historical background, the set-up, the working conditions of the system and the formation of EBSPs. Chapter 3 describes how crystal orientations can be determined from EBSPs, how the bands are being indexed and how the system is calibrated. Pattern recognition procedures which enable the bands of EBSPs to be localized and thus allows a fully automatic system to be obtained, is the main subject of chapter 4. In addition, chapter 4 describes a quantitative measure for the quality of digitized EBSPs. The possibility of applying this measure in investigations of partly recrystalized samples is also discussed in this chapter. Chapter 5 contains a discussion of the precision by which crystal orientations can be determined from EBSPs. In particular, results on the relative precision of both manually and automatically analyzed EBSPs are presented and compared. The influence of the pattern quality and the number of bands on the relative precision of measured crystal orientations is also

demonstrated in this chapter. The work and the results presented in this thesis are summarized in the final conclusion of chapter 6.

Chapter 2

The EBSP Technique

2.1 Historical Background

The observation of electron backscattering patterns was first reported by Alam, Blackman & Pashley (1954), who referred to them as high-angle Kikuchi patterns. Using a highly specialized instrument they were able to record these patterns on an electron sensitive film. In the 1970's a series of papers by Venables and co-workers (Venables & Harland, 1973; Venables, 1976; Venables & bin-Jaya, 1977) described how the patterns could be obtained in the SEM and used for determination of crystallite orientations. The patterns, now termed electron backscattering patterns, were recorded on a fluorescent phosphor screen placed in the specimen chamber and viewed by a low-light TV camera. The EBSPs were then photographed directly from the screen on which the video signal was displayed and analyzed on the basis of this photograph. Obviously, the determination of crystal orientations with such a system was slow and inconvenient.

A major advance towards faster and more user-friendly microtexture determination took place in the 1980's, when Dingley and co-workers developed an EBSP system which allowed real-time imaging of the patterns and computer-aided calculation of the crystal orientations (Dingley, Longden, Weinbren & Alderman, 1987). In this system the patterns are still recorded

on a phosphor screen and viewed by a low-light TV camera, but the video signal is now send through a frame store unit for temporal image averaging. This averaging improves the signal to noise ratio of the recorded pattern. The video signal is then send to a computer controlled frame-grabber in such a way that the patterns can be digitized and accessed by the computer. A trained operator must then point out the positions of two zone axes and supply their indices as input to a computer program. On the basis of this input the computer calculates the crystal orientation and then allows the user to verify the solution by displaying the position and indices of a number of low index zone axes. A disadvantage of the software developed by Dingley and co-workers is the requirement of a trained and experienced operator who must be able to recognize the appearance of certain low index zone axes in the EBSP.

The procedure developed by Schmidt and co-workers (Juul Jensen & Schmidt, 1990; Schmidt, Bilde-Sørensen & Juul Jensen, 1991) represents an important step towards faster and more user-friendly determination of crystal orientations from EBSPs. In this procedure the operator must supply the positions of at least two bands in the pattern. On the basis of the band positions and on a precalculated look-up table, the program suggests a probable indexing and displays the corresponding simulated pattern on top of the actual EBSP. The operator must then accept or reject the proposed solution by visually comparing the simulated pattern with the real one. This procedure requires very little training of the operator, and the corresponding computer program is able to analyze the patterns from materials of all crystal structures. Furthermore, it is an important advantage of the procedure that it is based on the position of bands, since the bands are easier to localize through digital image processing techniques.

2.2 The EBSP Set-up

The set-up of a typical EBSP system is illustrated in figure 2.2.1. To obtain an EBSP, the scanning electron microscope, in our system a JEOL JSM-840, is operated in spot mode so that a stationary beam of primary

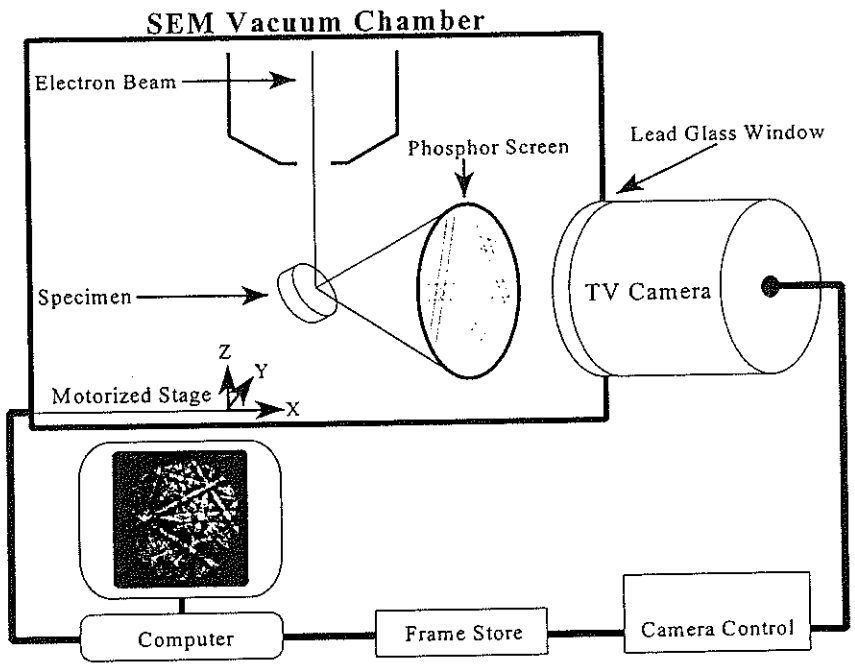

Figure 2.2.1 Illustration of the components in a typical modern EBSP system.

electrons is focused on a small area of the specimen. The electrons interact with the specimen, and a fraction of these are diffracted by the regular arrangement of atoms. Some of the backscattered electrons then collide with a fluorescent phosphor screen from which a light signal is emitted. To maximize the fraction of backscattered electrons the specimen must be tilted so that the angle between the specimen normal and the incident beam is at least 60°. The light signal from the phosphor screen has a very low intensity ($\sim 10^{-3}$ lux), and must therefore be viewed by an extremely sensitive camera. Traditionally, Silicon Intensified Target (SIT) cameras have been used for this purpose, but these are probably soon to be replaced by CCD (Charge Coupled Device) cameras, due to the rapid development in this technology. CCD cameras, though presently not quite as sensitive as the SIT type, offer better resolution and geometric image distortions are eliminated (Hjelen &

Qvale, 1993). These distortions are introduced by the camera lens installed in front of the SIT camera. An alternative way of removing such distortions is by using a fiber optic bundle to directly link the phosphor screen to the SIT camera (Kunze, Wright, Adams & Dingley, 1992). From the TV camera the video signal is send to a frame store device which digitizes the signal and performs temporal averaging to reduce the effect of random noise. The improved video signal is then again digitized by a frame grabber card installed on a computer. Many modern frame grabbers offer temporal image averaging and future EBSP systems will therefore not need a separate frame store unit. The digitized EBSP can now be accessed by the computer and used in either a semiautomatic computer program that requires operator involvement, or in a fully automated program, that performs all the required pattern analysis. Finally, in a fully automated system, the computer must control the position on the specimen from where the pattern is obtained. In our system this is accomplished by interfacing the computer with a motorized stage which is able to move the specimen independently in the microscope x, y and z directions.

The position of the phosphor screen relative to specimen surface affects both the quality and general appearance of the recorded EBSP. In our set-up, the camera and the phosphor screen are mounted in the side port of the JEOL JSM-840 and positioned so that the plane of the phosphor screen is parallel to the incoming electron beam. This geometrical arrangement, illustrated in figure 2.2.2, was designed by Hjelen (1990) and produces patterns with a very good contrast. As illustrated in figure 2.2.2., the phosphor screen is rotated around both the microscope y direction (the tilt angle, usually 70°) and the microscope z direction (~19°). In an alternative set-up the phosphor screen and the specimen surface are parallel (the camera and the phosphor screen are mounted in the rear port of the SEM), but this configuration results in patterns of a lower quality.

The angle covered by the EBSP depends on the size of the phosphor screen and its position relative to the source point. In the configuration illustrated above the angle captured by the screen will vary slightly in different directions across the screen, but a reasonable measure for this angle is 2·atan(r/R), where r is the radius of the phosphor screen and R is its

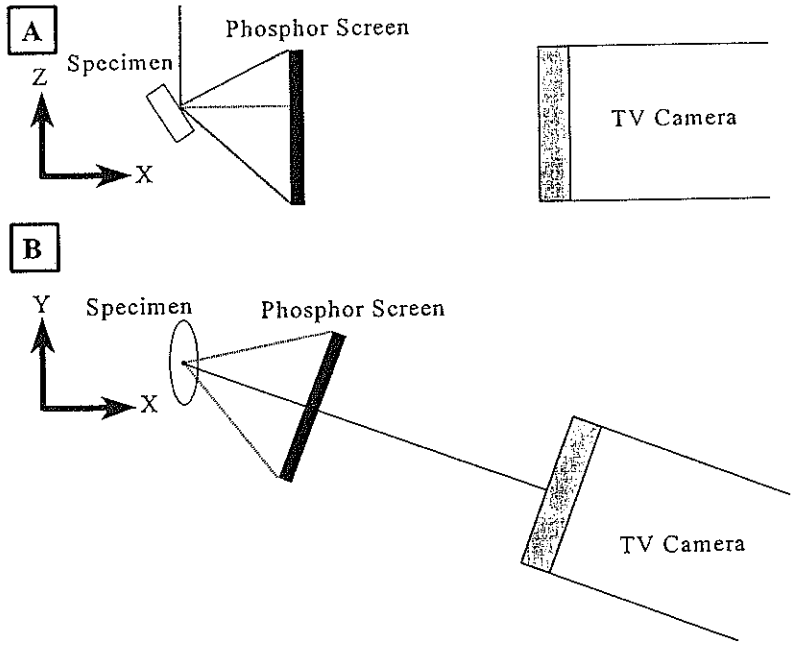

Figure 2.2.2 The geometrical arrangement of the specimen, phosphor screen and TV camera. A) Viewed in microscope y direction. B) Viewed in microscope z direction (from the electron beam).

distance from the source point. The values for our system are approximately r/R=25mm/35mm resulting in an angular coverage of 71.1°. This large angle makes interpretation of the patterns easier, and is an important advantage of the EBSP technique as compared with other microtexture techniques available in electron microscopes.

2.3 Obtaining EBSPs in the SEM

The backscattered electrons that form the electron backscattering pattern originate from a small volume below the specimen surface. The depth of this volume is of the order of 20nm when the electrons are accelerated over

20kV, and this very thin layer at the specimen surface must be clean and with a relatively low dislocation density in order to obtain EBSPs. For metallic materials this is usually accomplished by a mechanical polishing followed by electropolishing. Generally, the specimen preparation required to obtain EBSPs from polycrystals is relatively simple, as compared with the other techniques for microtexture determination. Note also, that specimen preparation techniques suitable for TEM samples, are usually also well suited for EBSP. For a short overview on specimen preparation the reader is referred to Randle (1992).

The operating conditions of the microscope strongly affect both the quality of the backscattered patterns and the size of the volume from which they originate. The size of the volume in which the backscattered electrons are generated, is directly related to the spatial resolution of the EBSP technique. This spatial resolution is usually defined and measured as the distance over which two patterns overlap, when the electron beam is moved across a well defined grain boundary. Since the specimen is tilted at least 60°, one would expect the resolution to be anisotropic and worst in the direction perpendicular to the tilt axis (the microscope y direction in our set-up as seen in figure 2.2.2). This turns out to be the case, and at a tilt angle of 70° the resolution is about 3 times worse in the direction perpendicular to the tilt axis compared with the resolution parallel to the axis. The factor 3 agrees well with what one would predict from a simple geometrical argument, since the beam diameter at the specimen surface will be 1/cos(tilt angle) larger perpendicular to the tilt axis than parallel to the axis. Hjelen (1990) has made a comprehensive study, though limited to aluminium, on the correlations between the spatial resolution, denoted d, and different parameters describing the operating conditions of the SEM. The effect of these parameters is shortly described in the following:

Accelerating Voltage - As the accelerating voltage and thereby the energy of the primary electrons is increased, d also increases rapidly (the resolution decreases). However, at low voltages, the patterns become noisy and less visible, probably due to a smaller gain from the phosphor screen. Hjelen (1990) proposed 20kV as a good compromise between resolution and pattern

quality for aluminium. For materials with higher atomic numbers the fraction of backscattered electrons becomes larger, and it may be advantageous to use a lower accelerating voltage. Patterns have been observed with voltages down to 4kV (Dingley, 1984).

Beam Current - The effect of increasing the current of the electron beam is an increased pattern quality, but a lower spatial resolution (d increases). The increasing value of d is expected, since the diameter of the beam is proportional to the square root of the beam current. For aluminium, Hjelen (1990) proposes 5nA as an appropriate value.

Tilt Angle - As mentioned above, the specimen must be tilted in order to obtain a reasonably large fraction of backscattered electrons. Patterns have been observed with tilt angles down to 45° (Venables & Harland, 1973), but usually the angle must be in the range 65-85° for good contrast to be obtained. Above 85° the elongation of the probe along the specimen surface results in diffuse patterns (Dingley, 1984). The spatial resolution in the direction perpendicular to the tilt axis decreases with increasing tilt angle, whereas the resolution in the direction of the tilt axis is unaffected by the angle. Hjelen (1990) proposes 70° as a good compromise for aluminium, but it may be advantageous to reduce the tilt angle for materials of higher atomic number.

Working Distance - Since the diameter of the electron beam is approximately proportional to the working distance, it is no surprise that the spatial resolution decreases as the working distance increases. The shortest working distance allowed in a JEOL JSM-840 at 70° tilt angle is 15mm, and since this is also the only working distance at which the dynamic focusing (and tilt correction if available) works without distortions, there is really no option here.

Final Lens Aperture - As the aperture of the final objective lens, and therfore also the divergens of the electron beam, is increased, the spatial resolution decreases. Hjelen (1990) suggests that this effect is caused by spherical

aberration, and proposes the use of the smallest possible aperture.

Using the operating conditions proposed by Hjelen (1990) for an aluminium sample, the spatial resolution in the tilt axis direction is reported to be ~250nm and perpendicular to the tilt axis ~670nm. These data were obtained using a standard W-filament. Harland, Akhter & Venables (1981) have reported a resolution of 20×80nm from nickel at 30kV and 75° tilt angle in a SEM equipped with a field emission gun.

2.4 The formation of EBSPs

Electron backscattering patterns are intimately related to Kikuchi patterns and the EBSP technique is therefore often referred to as backscatter Kikuchi diffraction (BKD). An EBSP is formed when a stationary electron beam is focussed on a small area of a crystalline material. As the beam enters the sample the electrons are subject to a diffuse inelastic scattering in all directions. The atomic planes of the crystalline material are thus showered by electrons arriving from all directions, and therefore also by electrons which fulfil the Bragg law

$$n\lambda = 2d_{hkl}\sin\theta, \qquad (2.4.1)$$

where θ is the Bragg angle, λ is the electron wavelength, n is an integer (the order of reflection) and d_{hkl} is the interplanar spacing for crystal planes with Miller indices (hkl). Electrons which impinge on a particular set of parallel crystal planes at the Bragg angle will be elastically scattered and form two cones of diffracted electrons as illustrated in figure 2.4.1. Similar cones are observed in Kossel diffraction of x-rays, and the cones are therefore sometimes referred to as Kossel cones. As illustrated in figure 2.4.1, the two cones of reflected electrons are symmetric about the reflecting crystal plane and separated by twice the Bragg angle. Even though this pair of cones will be recorded on the phosphor screen as hyperbolas, the Bragg angle is so small (~0.5°) and the opening angle of the cones (90°−θ) so large that the

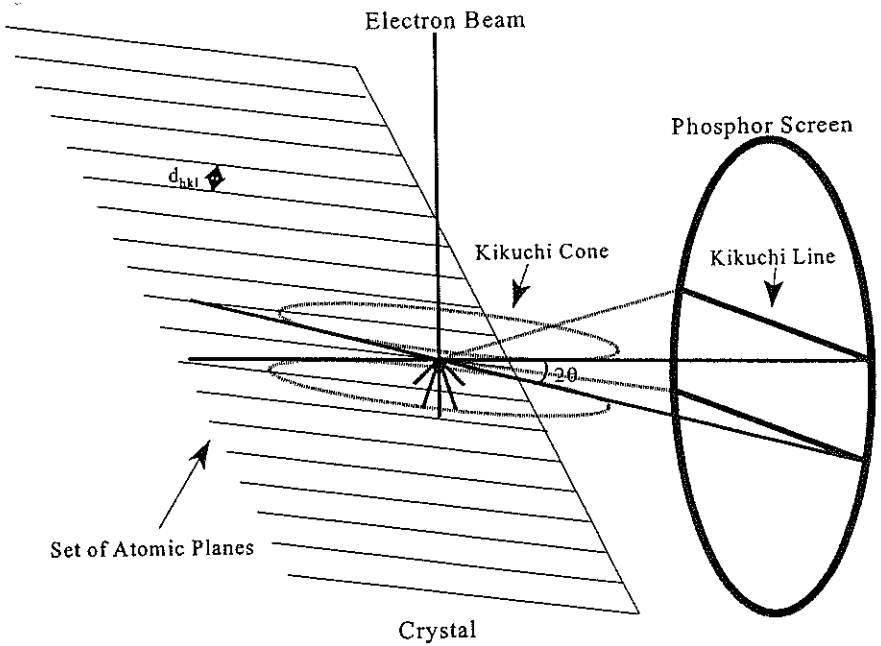

Figure 2.4.1 The formation of backscattered Kikuchi lines.

hyperbolas are essentially seen as two straight parallel lines known as Kikuchi lines. Each pair of Kikuchi lines are the result of diffraction from a particular plane in the crystal, and the intersection of the plane with the screen is a line which is located very close to the center between the two Kikuchi lines. The distance between a pair of Kikuchi lines is a function of the Bragg angle which again is inversely proportional to the interplanar spacing d_{hkl} as seen from equation (2.4.1) since $\sin\theta \approx \theta$ for small θ. A typical EBSP of good quality is shown in figure 2.4.2. It consists of bright bands on a diffuse background of non-uniform intensity. The background signal is produced by inelastically scattered electrons, and the non-uniform intensity is partly inherent to the set-up and the camera system and partly caused by the topography of the specimen surface. As seen from figure 2.4.2., the sharp Kikuchi lines that are observed in the TEM are not present in EBSPs. Instead, the Kikuchi lines are indirectly observed as the two relatively sharp boarders

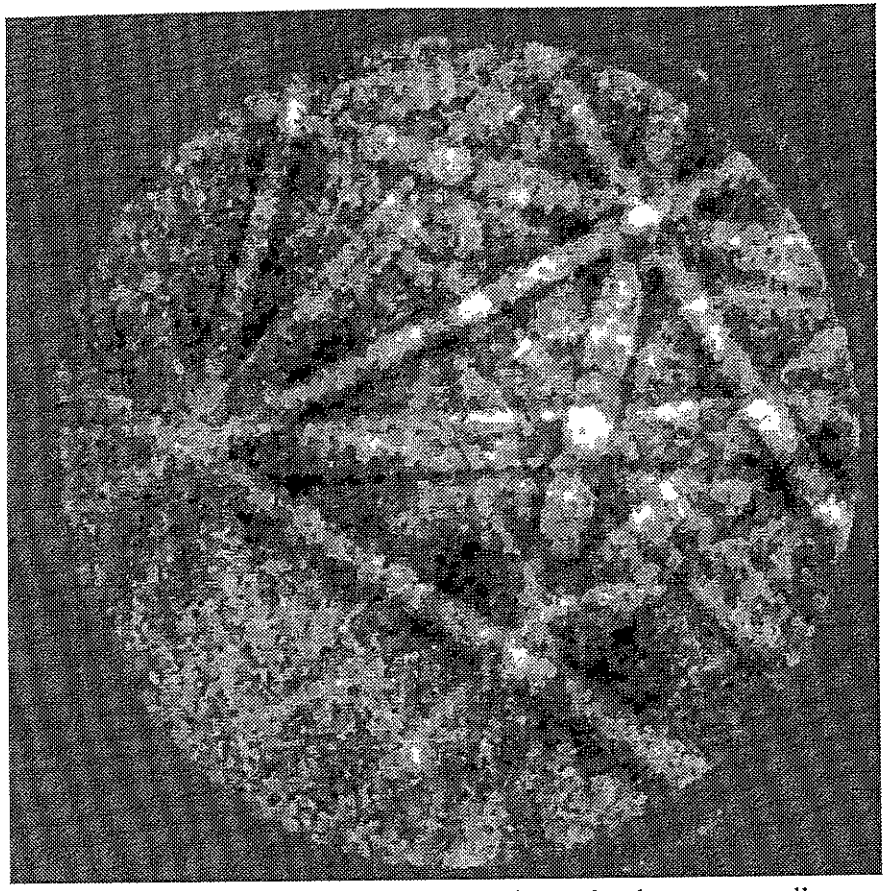

Figure 2.4.2 EBSP from pure Copper. The image has been temporally averaged and a background has been subtracted (400×400 pixels).

of the bright bands, i. e. as the two lines at which the intensity of the bands drop off rapidly. The image formation process described above and illustrated in figure 2.4.1 is obviously rather simplified and does not account for the observation of bright bands in EBSPs. These so-called *excess* bands are also observed in the TEM though they are far less visible than in EBSPs. It is quite complicated to describe the mechanisms leading to the formation of bands in Kikuchi patterns, and interested readers are referred to the introduction given by Joy, Newbury & Davidson (1982). The effect which forms the band

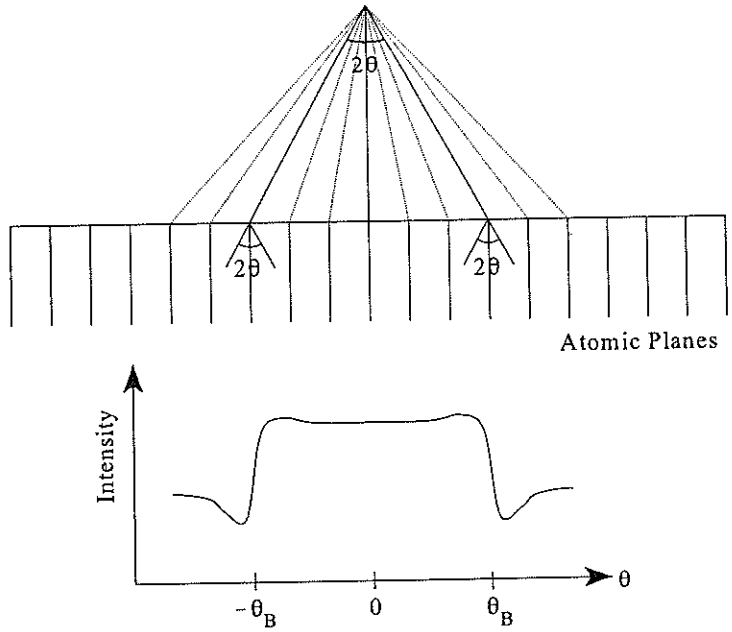

Figure 2.4.3 The formation of excess bands in EBSPs.

structure is known as the channeling effect, because it may be visualized through the existence of channels around the atomic planes in which the electrons can travel more easily (this way of visualizing the effect can, however, be somewhat misleading, since it would predict a smaller intensity of backscattered electrons within the Bragg angle; in fact the reverse is observed, i. e. a larger intensity within the Bragg angle). The result of the channeling effect is illustrated in figure 2.4.3. For angles smaller than the Bragg angle θ_B the multiple scattering events interfere to produce an enhanced signal of backscattered electrons. At the Bragg angle the backscattered signal drops off very fast, and for angles larger than θ_B the signal first reaches a minimum value and then flats out. The idealized band profile illustrated in figure 2.4.3 agrees well with what is observed in typical EBSPs and with the theory developed (Joy, Newbury & Davidson, 1982).

The intensity of a particular band relative to the intensities of other

bands can be predicted from the so-called structure factor F. It may be shown (see e. g. Eddington, 1975) that the intensity I of the band originating from lattice plane (hkl) is approximately proportional to the square of the structure factor

$$I \propto |F_{hkl}|^2 = \left[\sum_i f_i(hkl)\cos[2\pi(hx_i + ky_i + lz_i)]\right]^2 + \left[\sum_i f_i(hkl)\sin[2\pi(hx_i + ky_i + lz_i)]\right]^2, \quad (2.4.2)$$

where the summation is taken over all atoms in the unit cell, (x_i,y_i,z_i) is the relative position of atom i and $f_i(hkl)$ is the atomic form factor, which again depends on the interplanar spacing d_{hkl}. The equation above is extremely useful in the process of assigning Miller indices (hkl) to the bands in EBSPs, because it allows one to predict which bands are the most prominent in the patterns from a given material.

Chapter 3

Crystal Orientations from EBSPs

3.1 The Orientation Determination Problem

The orientation of a three dimensional object such as a crystal can be rigidly described by the rotation between two standard (rectangular and right-handed) Cartesian coordinate systems: A system $(O_u,\hat{\mathbf{u}}_1,\hat{\mathbf{u}}_2,\hat{\mathbf{u}}_3)$ fixed to the object and a system $(O_w,\hat{\mathbf{w}}_1,\hat{\mathbf{w}}_2,\hat{\mathbf{w}}_3)$ fixed to the "world", the reference frame. The base vectors $\hat{\mathbf{u}}_i$ and $\hat{\mathbf{w}}_i$ of the two frames are orthonormal (orthogonal and of unit length) and since we are only interested in the rotation between the frames (not translation), they can be assumed to have a common origin O. In the studies of crystal orientations, the axes $\hat{\mathbf{u}}_i$ of the system fixed to the crystal, shortly denoted U, are chosen parallel to appropriate crystallographic directions, e.g. in the case of cubic symmetry parallel to the cube edges [100], [010] and [001]. For non-cubic crystals, it is necessary (or at least extremely convenient) to refer and transform all crystallographic directions to a cubic basis as described by Young & Lytton (1972) or by Boisen & Gibbs (1985). The axes $\hat{\mathbf{w}}_i$ of the reference frame, shortly denoted W, are usually chosen parallel to appropriate directions suggested by the external shape of the sample, e. g. in the case of a rolled sheet parallel to the rolling direction (RD), the transverse direction (TD) and the normal direction (ND) respectively. The orientation of the crystal is then described by the matrix, commonly denoted

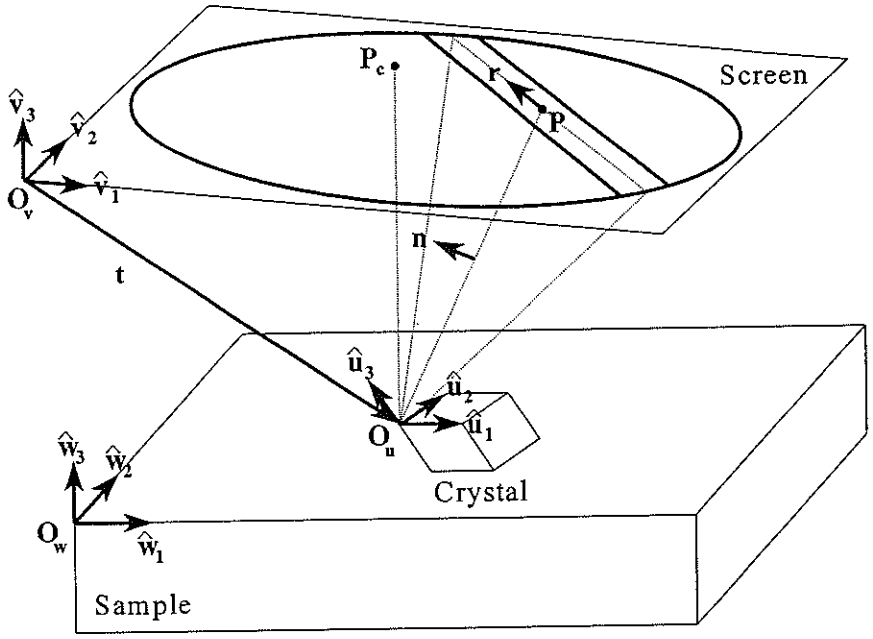

Figure 3.1.1 Coordinate systems and geometrical relationships in the EBSP set-up. See the text for further explanation.

g, which rotates the reference or sample system W into the object or crystal system U, so that the coordinates of an arbitrary vector **p** measured in the two coordinate system are related through

$$[\mathbf{p}]_U = \mathbf{g}[\mathbf{p}]_W = \begin{bmatrix} | & | & | \\ [\hat{\mathbf{w}}_1]_U & [\hat{\mathbf{w}}_2]_U & [\hat{\mathbf{w}}_3]_U \\ | & | & | \end{bmatrix} [\mathbf{p}]_W . \qquad (3.1.1)$$

Here $[\mathbf{p}]_U$ and $[\mathbf{p}]_W$ are the coordinates of vector **p** measured in U and W respectively, and **g** is a 3×3 matrix whose columns contain the coordinates of the axes of the sample frame measured in the crystal frame. The matrix **g** is orthogonal, $\mathbf{g}^T\mathbf{g} = \mathbf{g}\mathbf{g}^T = \mathbf{I}$ ($\mathbf{g}^T$ is the transpose of **g**, **I** is the 3×3 identity matrix) and its determinant det(**g**) = 1. The collection of all 3×3 orthogonal

matrices with determinant 1, forms a group (because the product of two rotation matrices is a rotation matrix, and because each rotation has an inverse) known as the *special orthogonal group* SO(3). An excellent reference on the basic properties of rotations is Altmann (1986).

In order to determine crystal orientations from EBSPs, a coordinate system $(O_v,\hat{v}_1,\hat{v}_2,\hat{v}_3)$ fixed to the pattern must be introduced in addition to the sample frame W and the crystal frame U. These coordinate systems and the geometrical relations in an EBSP set-up are sketched in figure 3.1.1. The unit vector **n** in figure 3.1.1 represents the normal to a crystal plane, whose trace can observed in the EBSP as a diffracted band. In accordance with equation (3.1.1), the orientation matrix **g** links the coordinates of **n** measured in frame U with the coordinates of **n** measured in W through the relation $[\mathbf{n}]_U = \mathbf{g}[\mathbf{n}]_W$. Let the matrix which describes the rotation from the crystal frame U into the pattern frame V be denoted **X**, and let the matrix **Y** describe the rotation from pattern frame V into the sample frame W. The coordinates of **n** measured in U, V and W are then linked by the relations

$$\begin{aligned} [\mathbf{n}]_V &= \mathbf{X}[\mathbf{n}]_U \\ [\mathbf{n}]_W &= \mathbf{Y}[\mathbf{n}]_V . \end{aligned} \qquad (3.1.2)$$

From equation (3.1.2), $[\mathbf{n}]_U = \mathbf{X}^T[\mathbf{n}]_V = \mathbf{X}^T\mathbf{Y}^T[\mathbf{n}]_W$, so that the crystal orientation matrix **g** can be found from

$$\mathbf{g} = \mathbf{X}^T\mathbf{Y}^T = (\mathbf{Y}\mathbf{X})^T \qquad (3.1.3)$$

The rotation matrix Y which describes the rotation between the sample frame and the pattern frame, may be regarded as a set-up constant, since it is unaffected by the local lattice orientation and only depends on the geometrical arrangement of the phosphor screen relative to the specimen. Obviously, the rotation **Y** is constant for a given sample positioned in the microscope, and the relative orientations between pairs of crystallites are therefore unaffected by it. Precise knowledge of the rotation **Y** is, however, required in cases where absolute crystallite orientations (the orientation relative to the sample system) are important. It is commonly assumed that **Y**

is constant and does not vary when different samples are being analyzed in the microscope. This assumption can only be approximately true, since it requires that the samples are positioned with their external axes (e.g. RD, TD and ND) pointing in exactly the same directions relative to some fixed axes (typically the microscope stage directions). In principle, the rotation **Y** between the sample system and the pattern system can be determined from parameters describing the EBSP set-up (tilt angle, the angle between the microscopy y direction and the screen normal, see figure 2.2.2). However, these parameters are difficult to measure and their values are not very reliable, and it is therefore better to determine **Y** by using a calibration crystal of known orientation. By using a crystal of known orientation **g** (we have used a ⟨001⟩ cleaved silicon single crystal) carefully aligned in the microscope, **Y** can be found from equation (3.3.1), $\mathbf{Y} = (\mathbf{Xg})^T = \mathbf{g}^T\mathbf{X}^T$, where the rotation matrix **X** is found as described later in this section. The calibration crystal of known orientation is then taken out of the microscope, the EBSP set-up disassembled, the crystal remounted and inserted into the microscope again. With the calibration crystal again carefully aligned with respect to the microscope directions, **Y** is recalculated as described above. This procedure is repeated as many times as time allows and the average rotation ⟨**Y**⟩ may then be calculated as described in Krieger Lassen, Juul Jensen & Conradsen (1994). Such a procedure provides important information about the precision of **Y** and thus on the absolute precision of crystal orientations determined from EBSPs (see also chapter 5).

The rotation matrix X which describes the rotation between the crystal and the pattern frame is far more interesting than the **Y** matrix, since it describes the orientation of the crystallites with respect to the pattern frame. The coordinates of the crystal plane normal **n** (see figure 3.1.1) measured in the crystal frame U are linked to coordinates of **n** measured in the pattern frame V through $[\mathbf{n}]_V = \mathbf{X}[\mathbf{n}]_U$. In order to determine **X** the coordinates of at least two crystal plane normals $\mathbf{n}_i$, i = 1,...,N (N≥2), must be measured in both the crystal and the pattern frame. The coordinates of the crystal plane normals $\mathbf{n}_i$ measured in the crystal frame U are found from the indexing procedure described in section (3.4). It is assumed here that the indexing problem has been solved, and Miller indices $(h_i k_i l_i)$ has been assigned to N bands observed

in the EBSP. The coordinates of crystal plane normal **n** in frame U are then found as

$$[\mathbf{n}]_U = \frac{1}{\sqrt{h^2 + k^2 + l^2}} \begin{bmatrix} h \\ k \\ l \end{bmatrix}. \qquad (3.1.4)$$

This equation is only valid for cubic crystals, and the reader is referred to Young & Lytton (1972) or Boisen & Gibbs (1985) for the general case. To understand the calculation of the coordinates of **n** in frame V, figure 3.1.1 must be studied in more detail. Note that the origin of the crystal frame O_U has been made to coincide with the source point P_S, the point on the surface at which the EBSP is emitted. The vector **t** in figure 3.1.1 represents the translation $O_V O_U$ from the pattern frame to the crystal frame. The significance of **t** may be clarified by the following relation,

$$\begin{aligned} [\mathbf{t}]_V &= [O_V P_C]_V + [P_C P_S]_V \\ &= \begin{bmatrix} x_0 \\ y_0 \\ 0 \end{bmatrix} + \begin{bmatrix} 0 \\ 0 \\ -R \end{bmatrix} = \begin{bmatrix} x_0 \\ y_0 \\ -R \end{bmatrix}, \end{aligned} \qquad (3.1.5)$$

which shows that **t** describes the position of the pattern center P_C $(x_0,y_0,0)$ (the foot of the perpendicular from the source point P_S to the phosphor screen) and the distance R from the source point to the pattern center. The coordinates of the translation vector measured in the pattern system $[\mathbf{t}]_V$ are thus simply the parameters which are found by the process of EBSP calibration. The calibration problem is the subject of section 3.3, and it will be assumed here that this problem has been solved and that $[\mathbf{t}]_V$ is known. In figure 3.1.1 the position of the band corresponding to a particular crystal plane normal **n** is described by a point P on the center line of the band and by a unit vector **r** pointing in the direction of the line. Since **n** is perpendicular to both **r** ($\mathbf{n}^T\mathbf{r} = 0$) and to $P_S P = O_V P - \mathbf{t}$ ($\mathbf{n}^T(O_V P - \mathbf{t}) = 0$), the coordinates of **n** measured in the pattern system can be found from

$$[\mathbf{n}]_V = \frac{[\mathbf{r}]_V \times ([O_V P]_V - [\mathbf{t}]_V)}{|[\mathbf{r}]_V \times ([O_V P]_V - [\mathbf{t}]_V)|}. \qquad (3.1.6)$$

Assume now that the positions of N bands in an EBSP have been found and that the corresponding crystal plane normals in the pattern system $[\mathbf{n}]_V$ have been calculated from equation (3.1.6). Assume also that the bands have been indexed and that the crystal plane normals in the crystal system $[\mathbf{n}]_U$ have been calculated from equation (3.1.4) or a more general expression. If for convenience the vector $[\mathbf{n}]_V$ is denoted $\mathbf{v}$ and $[\mathbf{n}]_U$ is denoted $\mathbf{u}$, N pairs of vectors $(\mathbf{u}_i,\mathbf{v}_i)$ are now available. The aim is now to determine the rotation matrix $\mathbf{X}\in SO(3)$ which simultaneously fulfils the N equations, $\mathbf{v}_i = \mathbf{X}\mathbf{u}_i$, i=1,...,N, where N≥2. Unfortunately, no such $\mathbf{X}$ exists due to errors in $\mathbf{v}_i$, and $\mathbf{X}$ must therefore be estimated from the data $(\mathbf{u}_i,\mathbf{v}_i)$, by minimizing some appropriate measure of the total error. This problem of fitting unit vectors to a rotation matrix, has been named *spherical regression* by Chang (1986) because of the obvious similarity to other regression problems, e. g. the familiar linear regression problem. An introduction to this and related problems can be found in Krieger Lassen, Juul Jensen & Conradsen (1994). An obvious choice for a measure of the total error is the familiar sum of squared errors SSE(X) defined by

$$\mathrm{SSE}(\mathbf{X}) = \sum_{i=1}^{N} |\mathbf{v}_i - \mathbf{X}\mathbf{u}_i|^2, \qquad (3.1.7)$$

and the rotation matrix $\hat{\mathbf{X}}$ which minimizes SSE(X) is naturally denoted the least squares estimate of $\mathbf{X}$. Note that $\sum|\mathbf{v}_i-\mathbf{X}\mathbf{u}_i|^2 = \sum(\mathbf{v}_i-\mathbf{X}\mathbf{u}_i)^T(\mathbf{v}_i-\mathbf{X}\mathbf{u}_i) = \sum(1+1-2\mathbf{v}_i^T\mathbf{X}\mathbf{u}_i) = 2N-2\sum\mathbf{v}_i^T\mathbf{X}\mathbf{u} = 2N-2\sum\cos\epsilon_i$, where ϵ_i is the angular distance or error between $\mathbf{v}_i$ and $\mathbf{X}\mathbf{u}_i$, so that the least squares estimate maximizes the sum of cosines of the angular error ϵ_i. The estimate $\hat{\mathbf{X}}$ of $\mathbf{X}$ can be found from the singular value decomposition (see f.ex. Golub & Van Loan, 1983) of the following 3 x 3 cross-product matrix A,

$$\mathbf{A} = \frac{1}{N}\sum_{i=1}^{N}\mathbf{u}_i\mathbf{v}_i^T = \mathbf{O}_1\Lambda\mathbf{O}_2^T. \qquad (3.1.8)$$

The right-hand-side of equation (3.1.8) represents the singular value decomposition of $\mathbf{A}$, arranged so that $\mathbf{O}_1, \mathbf{O}_2 \in SO(3)$ and $\Lambda = \mathrm{diag}(\lambda_1,\lambda_2,\lambda_3)$ (a diagonal 3×3 matrix) with $\lambda_1 \geq \lambda_2 \geq |\lambda_3|$. If at most one of the singular values λ_i equals zero, the least squares estimate of $\mathbf{X}$ is uniquely given by

$$\hat{\mathbf{X}} = \mathbf{O}_2\mathbf{O}_1^T. \qquad (3.1.9)$$

Routines for performing the singular value decomposition (SVD) can be found in many standard mathematical routine libraries (e. g. in the LINPACK, IMSL or NAG packages) and may also be found in the book by Press, Flannery, Teukolsky & Vetterling (1988). Even though the spherical regression procedure described above was first presented by MacKenzie (1957), it appears to be unknown in the community dealing with crystal orientation determination from EBSPs and other Kikuchi patterns.

A procedure for determination of the crystal orientation g from a particular EBSP has been presented above. However, one practical problem concerning the orientation of the crystals remains; the existence of symmetrically equivalent orientations. Due to the symmetry of the crystal, there exists a number of orientations $\mathbf{g}^e$ which are physically indistinguishable and correspond to exactly the same EBSP. For a cubic crystal, for example, the $\hat{\mathbf{u}}_1$ axis may assume 6 different directions, $\hat{\mathbf{u}}_2$ is then restricted to 4 different directions and $\hat{\mathbf{u}}_3$ is fixed as $\hat{\mathbf{u}}_1\times\hat{\mathbf{u}}_2$. Thus there are 4·6=24 g matrices that represent exactly the same physical orientation of a cubic crystal. Due to this ambiguity of the orientation matrix, it is desirable to have a criteria for choosing a unique g matrix among the 24 equivalent ones. Such a criteria has been proposed by Schmidt & Olesen (1989) and is based on the so-called *elementary pattern of the sphere* (EPS) which again may be represented as an area on a stereographic projection. The size and position of this "unit" area depends on the Laue group to which the material belongs, and for a cubic crystal belonging to group m3m (e. g. aluminium)

the area is bordered by the poles [001] - [1$\bar{1}$1] - [101] - [111] in the stereographic projection. For the bordering poles corresponding to other Laue groups see Schmidt & Olesen (1989). As the unique orientation matrix g among all equivalent orientation matrices $\mathbf{g}^c$, the one which has the coordinate vector $[\hat{\mathbf{v}}_3]_U$ confined within the bordering poles is chosen. The coordinates of the pattern frame z axis $\hat{\mathbf{v}}_3$ measured in the crystal frame $[\hat{\mathbf{v}}_3]_U$ can be found as the third column of the rotation matrix $\mathbf{X}^T$ or as the third row of $\mathbf{X}$. Obviously, the symmetry of the crystal is reflected in the rotation matrix $\mathbf{X}$ (and g), whereas symmetries of the sample are reflected in the rotation matrix Y (and g). In the case of a rolled sheet the $\hat{\mathbf{w}}_1$ axis may point in either the +RD or -RD direction, the $\hat{\mathbf{w}}_3$ axes in either the +ND or -ND direction and $\hat{\mathbf{w}}_2$ is then fixed as $\hat{\mathbf{w}}_3 \times \hat{\mathbf{w}}_1$. Hence, for a rolled sheet, 4 symmetrically equivalent rotation matrices $\mathbf{Y}^c$ exist, and the total number of equivalent orientation matrices $\mathbf{g}^c$ for a rolled cubic material is thus 4·24=96.

3.2 Calibration of an EBSP Set-up

The calibration of an EBSP set-up consists of determination of the pattern center P_C and the distance R from the source point P_S to the screen (see figure 3.1.1). As explained in the preceding section, the calibration parameters may conveniently be expressed as the coordinates of a vector t which represents the position of the source point P_S relative to the pattern frame V. Precise knowledge of the calibration parameters, the coordinates of t, is essential if precise crystal orientation measurements are required. Not only does the precision of these parameters affect the precision of orientation measurements, but it also affects the possibility of obtaining a correct indexing of the bands. Hence, if the parameters are far from their correct values, the indexing procedure is likely to fail, which of course will result in a completely wrong crystal orientation.

Many calibration procedures have been proposed in the literature, see Randle (1992) for an overview. Venables & bin-Jaya (1977) developed two methods in which the shadows cast by specially designed objects placed in

front of the phosphor screen were used to determine the calibration parameters. In one method a circular mask was mounted in front of, and concentric to, the screen; in the other three spherical balls were employed. An accuracy of ±0.1mm for the position of the source point was reported; this corresponds to a relative precision of 0.1/25= 0.4%, since the diameter of the phosphor screen was 25mm. The need for these highly specialized attachments to the EBSP set-up was eliminated in the calibration procedure which was later developed by Dingley & Baba-Kishi (1986). This method, which is still commonly used, is based on the pattern obtained from a special calibration specimen, a silicon single crystal with surface normal parallel to [001] and the [110] crystal direction made to lie parallel to microscope y direction. Depending upon the set-up of the phosphor screen with respect to the specimen surface, the pattern center may be found directly as the position of a particular zone axis (the [001] zone axis if the phosphor screen is parallel to the sample, the [114] zone axis if the sample is tilted 19.47° with respect to the screen surface). The source point to screen distance is then calculated from the distance between the pattern center and another zone axis and the angle between the two corresponding crystal directions (for details see e. g. Randle, 1992). Dingley & Baba-Kishi (1986) reported the accuracy of the source point determination to be 0.5%, but it is not clear from their paper what this relative precision is relative to. An alternative calibration method based on the shadows cast by two pairs of crossing wires has been developed by Day (1994). The two pairs of crossing wires are mounted at different positions in front of the phosphor screen, so that the direction defined by the two crossing points is exactly normal to the screen (an illustration can be found in Randle, 1992). The pattern center can then be found as the intersection point of the shadow lines when the crosswire shadows are superposed. The author has no detailed knowledge of this calibration procedure and its performance, but it is reported by Randle (1992) to be very precise. Finally, if the phosphor screen can be moved accurately in the direction of the screen normal, patterns obtained at different screen positions can be used for determination of the calibration parameters (Hjelen, Ørsund, Hoel, Runde, Furu & Nes, 1993). When the screen is retracted from its normal position the pattern center P_C will remain stationary, whereas all other

points will move away from P_C. By tracing the position of several points in patterns obtained at different positions, the pattern center can be located. The source point to screen distance can then be calculated from the positions of two zone axes and their corresponding indices. According to Hjelen (private communications), this method is not very precise and needs further development.

An obvious drawback of all the shadow casting calibration methods presented above is, besides the need for specialized set-up attachments, of course the shadows themselves. The shadows remove a fraction of the information in the EBSP and will inevitably have a negative effect on the performance of any image processing routine developed for automatic band localization. Unfortunately, the classical method based on a silicon crystal of known orientation can not be applied directly in our set-up, due to special geometrical arrangement of the phosphor screen relative to the specimen (figure 2.2.2). These problems were the motivation for the calibration procedure presented by Krieger Lassen & Bilde-Sørensen (1993). This calibration procedure will be described in detail in the following, along with recent extensions and developments.

The calibration procedure proposed by Krieger Lassen & Bilde-Sørensen (1993) uses the positions and indices of at least four zone axes to calculate the position of the pattern center and source point to screen distance. The coordinates of the pattern center P_C with respect to the pattern frame V are $[O_VP_C]_V = (x_0,y_0,0)$ and the distance from the source point P_S to the pattern center is $|P_SP_C| = R$. The vector describing the translation between the pattern frame V and the crystal frame U (see figure 3.1.1) is $\mathbf{t} = O_VP_S$, so that its coordinates measured in V are $[\mathbf{t}]_V = [O_VP_S]_V = [O_VP_C]_V+[P_CP_S]_V = (x_0,y_0,0) + R\cdot(0,0,-1) = (x_0,y_0,-R)$. The calibration problem can then be described in mathematical terms, as the problem of determining the coordinates of the source point P_S with respect to the pattern frame, or equivalently the coordinates of the translation vector $\mathbf{t}$. Let the points P_i, $i=1,...,N$, represent the positions of N zone axes in the pattern, and let the unit vectors pointing from the source point to the zone axes P_SP_i be denoted $\mathbf{p}_i=P_SP_i/|P_SP_i|$. It is now assumed that the indices of the zone axes $[u_iv_iw_i]$ are known, and hence the coordinates of $\mathbf{p}_i$ measured in the crystal frame are

given by

$$[\mathbf{p}_i]_U = \frac{1}{\sqrt{u_i^2 + v_i^2 + w_i^2}} \begin{bmatrix} u_i \\ v_i \\ w_i \end{bmatrix}. \qquad (3.2.1)$$

For non-cubic crystals the crystallographic directions $[u_iv_iw_i]$ must first be transformed to a standard cubic basis before the normalization in equation (3.2.1) is performed (see e. g. Young & Lytton, 1972). The same unit vectors $\mathbf{p}_i$ measured in the pattern frame V can be found from

$$[\mathbf{p}_i]_V = \frac{[O_VP_i]_V - [\mathbf{t}]_V}{|[O_VP_i]_V - [\mathbf{t}]_V|}, \qquad (3.2.2)$$

and are related to $[\mathbf{p}_i]_U$ by the rotation matrix $\mathbf{X}$, $[\mathbf{p}_i]_V = \mathbf{X}[\mathbf{p}_i]_U$. With knowledge of the calibration parameters $[\mathbf{t}]_V$ and the positions $[O_VP_i]_V$ and indices $[u_iv_iw_i]$ of at least two zone axes, the coordinate vectors $[\mathbf{p}_i]_U$ and $[\mathbf{p}_i]_V$ can be found from equations (3.2.1-2), and the rotation matrix $\mathbf{X}$ may then be calculated as described in section 3.1.

The calibration problem may now be stated as the problem of determining $[\mathbf{t}]_V$ without any knowledge about the rotation matrix $\mathbf{X}$, since $\mathbf{X}$ is obviously dependent on $[\mathbf{t}]_V$. The idea presented in Krieger Lassen & Bilde-Sørensen (1993) is to utilize the fact that the angles between pairs of zone axis vectors $(\mathbf{p}_i,\mathbf{p}_j)$ are the same in the crystal frame U and in the pattern frame V, i. e.

$$[\mathbf{p}_i]_V^T[\mathbf{p}_j]_V = (\mathbf{X}[\mathbf{p}_i]_U)^T(\mathbf{X}[\mathbf{p}_j]_U) = [\mathbf{p}_i]_U^T\mathbf{X}^T\mathbf{X}[\mathbf{p}_j]_U = [\mathbf{p}_i]_U^T[\mathbf{p}_j]_U. \qquad (3.2.3)$$

The left-hand-side of this equation is dependent on $[\mathbf{t}]_V$, whereas the right-hand-side is known. Equation (3.2.3) thus represents an equation with three unknowns $[\mathbf{t}]_V = (x_0,y_0,-R)$. If the positions and indices of N zone axes are known, a total of $N\cdot(N-1)/2$ equations of the form (3.2.3) are available; one for each zone axes pair (i,j). Due to inevitable errors in the position of the zone axes $[O_VP_i]_V$ and therefore in $[\mathbf{p}_i]_V$ (equation 3.2.2) it will, however, not

be possible to find parameters $[t]_V$, which will simultaneously satisfy all of these N·(N−1)/2 equations. Instead the calibration parameters will be found as the vector $[\hat{t}]_V$ which minimizes the following sum of squared errors,

$$SSE(t) = \sum_{(i,j)} |[p_i]_V^T [p_j]_V - [p_i]_U^T [p_j]_U|^2$$

$$= \sum_{(i,j)} \left| \frac{([O_V P_i]_V - [t]_V)^T}{|[O_V P_i]_V - [t]_V|} \cdot \frac{([O_V P_j]_V - [t]_V)}{|[O_V P_j]_V - [t]_V|} - [p_i]_U^T [p_j]_U \right|^2, \quad (3.2.4)$$

where the summation is taken over all zone axes pair (i,j). The following procedure for obtaining the calibration parameters can be described:

1. An EBSP of high quality is obtained from an arbitrary specimen.

2. A number of the zone axes are indexed in some way and the vectors $[p_i]_U$ calculated from equation (3.2.1).

3. The positions of the indexed zone axes $[O_V P_i]_V$ are found by an operator.

4. The calibration parameters may then be found as the coordinates of the vector $[\hat{t}]_V$, which minimizes the sum given in equation (3.2.4).

Note that EBSPs from any specimen may be used in this calibration procedure, as long as the quality of the pattern allows at least four zone axes to be recognized and located with a reasonable precision. The pattern must then be indexed in some way; e. g. with the aid of Kikuchi maps or by using the EBSP indexing software if a reasonable guess for the true calibration parameters is available (this is typically the case, unless the EBSP set-up has changed drastically). The locations of the indexed zone axes are simply found by superimposing a cursor onto the digitized EBSP and then let a trained operator point them out. The minimization of the sum in equation (3.2.4) with respect to $[t]_U$ can be performed by many different numerical procedures; such procedures can be found in all standard mathematical routine libraries. We have found that the minimization procedure known as Powell's method

(see e. g. Press *et al.*, 1988) performs well with this specific problem and is both very precise and relatively fast.

It is of course vital for the success of this calibration procedure that there is a unique global minimum to the minimization problem of equation (3.2.4). Fortunately, this is in general the case when at least four zone axes are used. The existence of a global minimum was tested by starting off the minimization procedure at several different starting points and checking for convergence to the same solution, within machine accuracy. With only three zone axes as input to the procedure, it was observed that several minima existed, each providing a perfect fit, SSE(t)=0 (within machine accuracy). This fact indicates that the three equations (3.2.2) have several exact solutions when three zone axes are used, N=3. With four zone axes as input, a unique solution was found unless three of the zone axis were on a common line, which means that three of the vectors p_i lie in a common plane, i. e. are linearly dependent. The situation for N=5 is quite similar, i. e. a unique solution exists unless four of the zone axes are collinear. With six or more zone axes N≥5, it is very unlikely that (N-1) of the zone axes lie on a common line, and so, in practice, there will always be a unique solution to the calibration problem. These conditions for obtaining a unique solution to the calibration problem are based purely on observations of the behavior of equation (3.2.3), and it would be desirable to have a better theoretical understanding of the mathematical properties of this minimization problem. It was recently found by the author of this thesis that a problem which is mathematical equivalent to the calibration problem, arises in machine vision and automated cartography. In automated cartography the equivalent problem is referred to as the *location determination problem* (Fischler & Bolles, 1981), and in machine vision the problem is referred to as the *camera calibration problem* (see e. g. Holt & Netravali, 1991). Fishler & Bolles (1981) showed that in general there are four solutions to the calibration problem when three zone axes are used, and they derived the corresponding solutions. They also showed that a unique solution exists when four zone axes are used, provided that no more than two of the zone axes lie on a single line. These results were verified by Holt & Netravali (1991), who also presented a more formal mathematical formulation of the problem. It should

also be noted here that the calibration problem has a close relationship to a special data analysis method know as *procrustes analysis* often used in the psychological literature (see e. g. Goodall, 1991). It seems likely that important information related to the calibration procedure presented by Krieger Lassen & Bilde–Sørensen (1993), may be obtained by studying the relevant literature on camera calibration, cartography, and procrustes analysis.

To test the performance of the calibration procedure described above, 10 high quality EBSPs from pure copper were obtained and indexed with the indexing software. The patterns were from crystallites of orientations well spread in the orientation space SO(3). For each pattern, the calibration procedure was repeated 10 times using the same collection of zone axes. As many zone axes as possible were used, as long as their positions were relatively well defined, and the zone axes were generally chosen to be well spread over the pattern. From 9 to 13 zone axes were used for the different EBSPs. The observed spread in the values of the calibration parameters $[\mathbf{t}]_V = (x_0, y_0, -R)$ is relatively small (the standard deviation is in the order of 1 pixel), when the same pattern is used repeatedly with the same set of zone axes. The average of the calibration parameters were then calculated for each of the 10 patterns and the result are given below in table 3.2.1.

EBSP	X_0	Y_0	R
1	192.5	350.2	258.8
2	190.1	350.2	259.1
3	190.2	349.2	261.0
4	195.3	351.5	259.2
5	194.9	349.5	264.3
6	194.7	352.5	260.5
7	192.1	352.7	258.9
8	195.4	349.7	263.3
9	189.7	345.3	262.8
10	191.3	352.6	257.1
Mean	192.6	350.3	260.5
Standard Dev.	2.30	2.21	2.32
Precision (95%)	±1.6	±1.6	±1.7

Table 3.2.1 The calibration parameters determined on the basis of 10 EBSPs from pure copper. For each pattern, the calibration paramters were determined 10 times by repeatedly localizing the same set of 9 to 13 zone axes. The table lists the average values of the 10 measurements; see text for further details.

The last row lists the uncertainties of the average of the calibration parameters (x_0, y_0, R) as 95% confidence intervals, assuming normality of the observation. The estimated calibration parameters are measured in pixels, and since the diameter of the phosphor screen is about 380 pixels, the relative precision may be defined as 1.6/380 = 0.42%. This compares well with what has been reported for other calibration procedures (Venables & bin-Jaya; 1977; Dingley & Baba-Kishi; 1986). It is very complicated to described how the uncertainties in the calibration parameter affect the uncertainty of the

rotation matrix **X** (see section 5 for a discussion on precision). However, the angle between the vectors $P_SP_C = (0,0,R)$ and $P_SP_C^* = (\Delta x_0,\Delta y_0,R)$ may provide some measure of the angular precision, $\Delta\omega = \text{acos}(R/(\Delta x_0^2+\Delta y_0^2+R^2)^{1/2}) = \text{acos}(260.5/(1.6^2+1.6^2+260.5^2)^{1/2}) = 0.50°$. Obviously, the precision increases if more patterns are used in the calibration process, and if the errors can be assumed to follow normal distributions, the uncertainties will be ~1.1 pixels when 20 EBSPs are used. The relative precision would then be 1.1/380 = 0.29% and the angular precision $\Delta\omega = \text{acos}(260.5/(1.1^2+1.1^2+260.5^2)^{1/2}) = 0.34°$.

It is quite obvious that the calibration procedure presented above could easily be modified to use crystallographic planes instead of zone axes. The benefit from using planes instead of zone axes is that bands are easier to localize by image processing routines, and that a fully automated calibration procedure may therefore be obtained. Let the unit vectors $\mathbf{n}_i$, i=1,...,N, represent the normals to N planes observed in the pattern as bands, and let the known indices of the plane be $(h_ik_il_i)$, so that the coordinates of $\mathbf{n}_i$ measured in the crystal frame are given by

$$[\mathbf{n}_i]_U = \frac{1}{\sqrt{h_i^2 + k_i^2 + l_i^2}}\begin{bmatrix} h_i \\ k_i \\ l_i \end{bmatrix}. \qquad (3.2.5)$$

For non-cubic crystals the crystallographic planes $(h_ik_il_i)$ must be transformed to a standard cubic basis (see e. g. Young & Lytton, 1972). The same unit vectors $\mathbf{n}_i$ measured in the pattern frame V can be found from

$$[\mathbf{n}_i]_V = \frac{[\mathbf{r}_i]_V\times([O_VP_i]_V - [\mathbf{t}]_V)}{|[\mathbf{r}_i]_V\times([O_VP_i]_V - [\mathbf{t}]_V)|}, \qquad (3.2.6)$$

where $\mathbf{r}_i$ and O_VP_i describe the direction and position of the band i (see figure 3.1.1). The coordinate vectors $[\mathbf{n}_i]_V$ and $[\mathbf{n}_i]_U$ are related by the rotation matrix **X** by $[\mathbf{n}_i]_V = \mathbf{X}[\mathbf{n}_i]$.

As described above, the calibration problem may now be stated as the

problem of determining $[\mathbf{t}]_V$ without any knowledge about the rotation matrix **X**. This problem may be solved by utilizing the fact that the angles between pairs of crystal normal vectors $(\mathbf{n}_i,\mathbf{n}_j)$ are the same in the crystal frame U and in the pattern frame V, i. e. $[\mathbf{n}_i]_V^T[\mathbf{n}_j]_V = [\mathbf{n}_i]_U^T[\mathbf{n}_i]_U$. Since the left-hand-side of this expression is dependent on $[\mathbf{t}]_V$ whereas the right-hand-side is known it represents one equation with the three unknowns $[\mathbf{t}]_V = (x_0,y_0,-R)$. Given the positions and indices of N bands, $N\cdot(N-1)/2$ equations of the form $[\mathbf{n}_i]_V^T[\mathbf{n}_j]_V = [\mathbf{n}_i]_U^T[\mathbf{n}_i]_U$ are available; one for each band pair (i,j). Due to inevitable errors in the position of the bands, these equations cannot be solved simultaneously, and the calibration parameters will therefore be found as the vector $[\hat{\mathbf{t}}]_V$ which minimizes the sum of squared errors,

$$SSE(\mathbf{t}) = \sum_{(i,j)} |[\mathbf{n}_i]_V^T[\mathbf{n}_j]_V - [\mathbf{n}_i]_U^T[\mathbf{n}_j]_U|^2 \qquad (3.2.7)$$

$$= \sum_{(i,j)} \left| \frac{([\mathbf{r}_i]_V\times([O_VP_i]_V - [\mathbf{t}]_V))^T}{|[\mathbf{r}_i]_V\times([O_VP_i]_V - [\mathbf{t}]_V)|} \cdot \frac{([\mathbf{r}_j]_V\times([O_VP_j]_V - [\mathbf{t}]_V))}{|[\mathbf{r}_j]_V\times([O_VP_j]_V - [\mathbf{t}]_V|)} - [\mathbf{n}_i]_U^T[\mathbf{n}_j]_U \right|^2,$$

where the summation is taken over all unique band pairs (i,j). A procedure for obtaining the calibration parameters from indexed bands can now be described:

1. An EBSP of good quality is obtained from an arbitrary specimen.

2. A number of the bands are indexed in some way and the vectors $[\mathbf{n}_i]_U$ calculated from equation (3.2.5).

3. The directions $[\mathbf{r}_i]_V$ and positions $[O_VP_i]_V$ of the indexed bands are found by an operator or an image processing procedure.

4. The calibration parameters may then be found as the coordinates of the vector $[\hat{\mathbf{t}}]_V$, which minimizes the sum given in equation (3.2.7).

The indexing of the bands can be performed by the EBSP indexing software, when a rough guess for the true calibration parameters are available (this is

usually the case, unless the set-up geometry has been changed drastically), or with the aid of maps. The minimization of the expression in equation (3.2.7) is again performed by some appropriate numerical procedure, e. g. the Powell's method used above in the zone axes case.

It was described above for the calibration procedure based on zone axes that three zone axes were not enough to ensure a unique minimum and thus a unique set of calibration parameters. As expected, the same holds for the calibration procedure based on bands, and therefore at least four bands are required for uniqueness. With four bands used as input to the procedure, a unique solution was in general found, unless three of the bands had a common intersection point (a zone axis), which means that three of the vectors $\mathbf{n}_i$ lie in a common plane, i. e. are linearly dependent. In more general terms, it was observed that with $N \geq 4$ bands used as input, a unique solution was always found, unless (N-1) of the bands intersected in a common point. This fully agrees with the observations made in the zone axes case.

The performance of the calibration procedure based on the positions and indices of bands was tested with the same 10 EBSPs used for testing the procedure based on zone axes. As before, the calibration procedure was repeated 10 times for each pattern using the same collection of bands. As many bands as possible were used, as long as their positions were relatively well defined; from 11 to 13 bands were used for the different EBSPs. The observed spread in the values of the calibration parameters $[\mathbf{t}]_V = (x_0, y_0, -R)$ was slightly larger (the standard deviation was of the order of 1.3 pixel) than observed for zone axes, when the same pattern was used repeatedly with the same set of bands. The average of the calibration parameters was then calculated for each of the 10 patterns and the result is given below in table 3.2.2.

EBSP	X_0	Y_0	R
1	189.6	348.3	259.4
2	191.5	351.7	263.8
3	192.5	347.9	259.9
4	190.9	347.2	263.3
5	196.9	349.0	262.0
6	192.2	349.1	260.3
7	191.1	350.4	261.1
8	192.7	354.2	258.8
9	193.4	350.0	258.0
10	189.9	348.1	260.7
Mean	192.1	349.6	260.7
Standard Dev.	2.08	2.10	1.88
Precision (95%)	±1.5	±1.5	±1.3

Table 3.2.2 The calibration parameters determined on the basis of 10 EBSPs from pure copper. For each pattern, the calibration paramters were determined 10 times by repeatedly localizing the same set of 11 to 13 bands. The table lists the average values of the 10 measurements; see text for further details.

When compared with the results given in table 3.2.1 for calibration using zone axes, it is observed that the difference in the estimated calibration parameters is small and safely within the 95% confidence limits. The standard deviations and therefore also the confidence limits (again based on a normal distribution assumption) are almost the same for the two procedures, and it is therefore not possible - with the data presented - to draw any conclusions regarding possible differences in the precision of the two procedures.

Even though it would be desirable to perform a more thorough statistical investigation of the precision of the calibration procedures introduced above, the data presented clearly indicate that high precision estimates of the calibration parameters can be obtained. There are several important advantages of these two equivalent approaches to calibration. First of all, no special standard specimens or specialized attachments to the EBSP set-up are required. Secondly, the procedure can be used on any EBSP system, regardless of the geometrical set-up, contrary to the procedure based on a silicon crystal (Dingley & Baba-Kishi, 1986). Finally, with the aid of image processing procedures designed for band localization, it is possible to obtain a fully automatic calibration procedure. It is obviously very convenient to have such an automatic procedure, but its usefulness may be discussed, since the EBSP system is usually only calibrated when the geometry of the set-up has changed (which seldomly occurs). It must be noted that the calibration parameters change when the source point moves relative to phosphor screen, i. e. when the specimen is moved in the microscope x direction (see figure 2.2.2). However, since the electron beam then moves out of focus, it is necessary to correct for this by moving the specimen an appropriate amount in the z direction, and thus the calibration parameter remains unchanged. As a final note on this novel approach to the calibration of an EBSP set-up, it is important to realize the influence of image distortions, introduced by the camera lens installed in front of the SIT camera. The author believes that a relatively large part of the variations seen in the estimated calibration parameters when different patterns are used for calibration is due to such distortions. Eliminating these distortions would improve not only the calibration accuracy but also the overall accuracy of orientation measurements.

3.3 Automated Indexing of EBSP Bands

Given the positions of N bands in an EBSP and the calibration parameters $[\mathbf{t}]_V$, the object is now to determine which crystal planes the bands were diffracted from. Crystal planes are traditionally described by Miller

indices (hkl) and the problem of assigning Miller indices to them is referred to as the indexing problem. There is a simple correspondence between the Miller indices (hkl) of a plane and the crystal plane normal $[\mathbf{n}]_U$ as described by equation (3.2.5) (and the comment below it), and the determination of the vectors $[\mathbf{n}_i]_U$ will therefore also be referred to as indexing. To solve the indexing problem the following types of information can be used:

1. From the positions of the N bands and the calibration parameters the crystal plane normals referred to the pattern frame $[\mathbf{n}_i]_V$ can be calculated from equation (3.2.6). The angle between a pair of crystal plane normals is the same in the pattern and the crystal frame, $[\mathbf{n}_i]_V^T[\mathbf{n}_j]_V = [\mathbf{n}_i]_U^T[\mathbf{n}_j]_U$. This property is the foundation of the indexing procedure.

2. From knowledge of the material under investigation and its atomic arrangement, the intensities of bands from different crystal planes (hkl) can be predicted by considering the square of the structure factor F_{hkl} (equation 2.4.2). By only considering crystal planes which produce strong reflections and high intensity bands, the indexing problem is greatly simplified.

3. The width of the observed bands is a function of the Bragg angle θ_B which again is a function of the interplanar spacing d_{hkl} (equation 2.4.1). It is therefore possible to gain information about the indices of a band from the observed band width. However, the band widths can only be very roughly determined from EBSPs, and can therefore only serve as a guide in the indexing process. Our indexing procedure does not use band width information.

The indexing procedure described in the following is - to a large extent - based on a procedure developed and implemented by Niels Henrik Schmidt. The basic ideas of the procedure were presented in Schmidt, Bilde-Sørensen & Juul Jensen (1991). However, the original procedure has been greatly modified to accommodate for the special requirements in a fully automated system.

Based on calculations of the structure factor F_{hkl} for a specific material

(equation 2.4.2), the Miller indices (hkl) of the crystal planes which generate the brightest bands are found and saved to a file. For aluminium, for example, the file contains all planes from the families {111}, {200}, {220} and {311}. The {111} family is represented by the planes: (111), (11$\bar{1}$), (1$\bar{1}$1) and ($\bar{1}$11), since the four remaining planes are found by a change of sign. Equivalently, the {200} family is represented by 3 planes, {220} by 6 planes and {311} by 12 planes. It will be assumed that the crystal planes $(h_s k_s l_s)$ have been ordered by the index s, and the correspondingly ordered crystal plane normals are denoted $[\mathbf{n}_s^*]_U$. The normals $[\mathbf{n}_s^*]_U$ to all of the crystal planes $(h_s k_s l_s)$ are now calculated from equation (3.2.5) (or for non-cubic crystals as described in e. g. Young & Lytton, 1972), and the angles between all possible pairs of normals then found from

$$\theta_{st} = \text{acos}(|[\mathbf{n}_s^*]_U^T[\mathbf{n}_t^*]_U|). \qquad \textbf{(3.3.1)}$$

All of these angles are sorted and stored in a look-up table. In the case of aluminium, 25 bands are considered resulting in a total of 25·24/2 = 300 angles, ranging from 25.24° to 90°. All of the angles appear several times in the look-up table, indicating that several different pairs of crystal plane normals have the same angular distance.

Assume now that N crystal plane normals $[\mathbf{n}_i]_V$, i = 1,...,N, have been calculated from the calibration parameters and the positions of N bands in an EBSP (equation 3.2.6). It will also be assumed that there is a natural ordering of the bands ($[\mathbf{n}_i]_V$) as indicated by the index i. In the case where the bands have been located by an operator, i = 1 simply refers to the band located first and i = N to the band located last. In the case where an image processing procedure has located the bands, the ordering will be such that i = 1 refers to the most reliable band and i = N to the least reliable band. The indexing procedure now proceeds in the following manner:

1. Calculate the angle between the two first crystal plane normals, $\alpha = \text{acos}(|[\mathbf{n}_1]_V^T[\mathbf{n}_2]_V|)$, and find the closest matching angle $\theta \approx \alpha$ in the look-up table. As described above, there will be a small collection of different plane normal pairs $\{[\mathbf{n}_k^*]_U,[\mathbf{n}_l^*]_U\}$ that all have the same angular distance, i.e.

$\text{acos}(|[\mathbf{n}_k^*]_U^T[\mathbf{n}_l^*]_U|) = \theta$. For each of these pairs (k,l), perform the following steps:

2. Given the crystal plane normal pair $([\mathbf{n}_k^*]_U,[\mathbf{n}_l^*]_U)$ it is now possible to propose several indexing solutions; i. e. propose coordinates for $[\mathbf{n}_1]_U$ and $[\mathbf{n}_2]_U$. In principle the following eight solutions are possible: $([\mathbf{n}_1]_U,[\mathbf{n}_2]_U)=(\pm[\mathbf{n}_k^*]_U,\pm[\mathbf{n}_l^*]_U)$ and $([\mathbf{n}_1]_U,[\mathbf{n}_2]_U)=(\pm[\mathbf{n}_l^*]_U,\pm[\mathbf{n}_k^*]_U)$. However, in general only four of these solutions need to be considered: Once $[\mathbf{n}_1]_U$ has been chosen as either $\pm[\mathbf{n}_k^*]_U$ or $\pm[\mathbf{n}_l^*]_U$, $[\mathbf{n}_2]_U$ must be chosen to ensure that the sign of $[\mathbf{n}_1]_U^T[\mathbf{n}_2]_U$ equals that of $[\mathbf{n}_1]_V^T[\mathbf{n}_2]_V$. Obviously, this sign rule cannot be applied when $\mathbf{n}_1$ and $\mathbf{n}_2$ are perpendicular, $\mathbf{n}_1^T\mathbf{n}_2 = 0$, and in that case all eight indexing solutions must be tested. For each possible indexing of $([\mathbf{n}_1]_U,[\mathbf{n}_2]_U)$, perform the following steps:

3. Given the two pairs of vectors $([\mathbf{n}_1]_V,[\mathbf{n}_2]_V)$ and $([\mathbf{n}_1]_U,[\mathbf{n}_2]_U)$, the matrix **X** describing the rotation between the crystal frame U and the pattern frame V can be calculated as described in section 3.1. Initially, it is checked whether the rotation matrix **X** satisfies the uniqueness criteria described in section 3.1 (to choose among the symmetrically equivalent orientations). If this criteria is not satisfied, go back to step 2. The object is now to validate the proposed rotation matrix **X**. If only the two bands corresponding to $\mathbf{n}_1$ and $\mathbf{n}_2$ are available, the proposed solution must be validated by displaying a simulated pattern on top of the observed EBSP. This simulated pattern is generated in the following way: All the crystal plane normals from the look-up table are transformed to the pattern frame $[\mathbf{n}_s^*]_V = \mathbf{X}[\mathbf{n}_s^*]_U$; the traces of the planes can then be found from $[\mathbf{n}_s^*]_V$ and the calibration parameters $[\mathbf{t}]_V$, and are displayed in the pattern as lines. An operator must then judge the proposed rotation matrix **X** by visually comparing the simulated pattern with the real one. If more than two bands are available $[\mathbf{n}_i]_V$, i = 1,...,N (N>2), the (N-2) bands $[\mathbf{n}_i]_V$, i = 3,...,N can be used to validate **X**. This procedure, which is an addition to the original indexing procedure developed by Niels Henrik Schmidt, works as follows: For each band $[\mathbf{n}_i]_V$, find that vector **u** among all the vectors $\mathbf{u}_s = \pm[\mathbf{n}_s^*]_U$ (± the vectors in the look-up table) that minimize $|[\mathbf{n}_i]_V - \mathbf{X}\mathbf{u}_s|$, and store the minimum value in a table FIT(i). The vector **u**

represents the indexing of band i, $[\mathbf{n}_i]_U = \mathbf{u}$, and FIT(i) is a measure of how well band i fits the proposed **X**. The sum of the fit values for each band $\sum$FIT(i) is good measure for the agreement between the proposed rotation matrix **X** and the localized bands. This sum is stored for each of the proposed solutions, and the one which resulted in the smallest sum (i. e. the best fit) is accepted as the real solution. If the indexing is done semi-automatically under supervision, the operator must validate the proposed solution by comparing a simulated pattern with the real one. If the patterns do not agree (this may occasionally happen if less than four bands are used), the solution which gives the next best fit is tried, and so on. In fully automated analyses, typically eight or more bands are used, and the matrix **X** which gives the best fit will in practice always be the right solution, unless the bands are very poorly localized by the image processing. Note, that even if one or two of the automatically localized bands are totally wrong, or right but not contained in the look-up table (this happens occasionally), the right solution matrix **X** will still produce a significantly better fit to the bands, than all the wrong solutions. Note also, that this procedure allows one to disregard poorly localized bands, or bands whose indices are not found in the look-up table, since these can be distinguished by a large value for FIT(i). This is put to use in the final calculation of **X**, which is based on all bands but those that have FIT values larger than some appropriate threshold value.

The major steps of this indexing procedure are illustrated in figure 3.3.1. It was described under point 1. above, that the angle between the two first crystal plane normals $\alpha = \text{acos}(|[\mathbf{n}_1]_V^T[\mathbf{n}_2]_V|)$, was used to find the closest matching angle $\theta \approx \alpha$ in the look-up table. In practice, it may be necessary to use the look-up table not only at the closest matching angle θ, but at some appropriate interval $\pm\Delta\theta$ around θ. By increasing $\Delta\theta$, the chance of finding the right indexing solution also increases, but the drawback is, of course, that more suggestions for **X** must be considered, and the total processing time therefore also increases. If the bands are well localized and the calibration parameters are known to a high precision, the interval $\Delta\theta$ can be made very small.

When the indexing is performed on automatically detected bands, it is vital for the success of the procedure described above that the first two bands

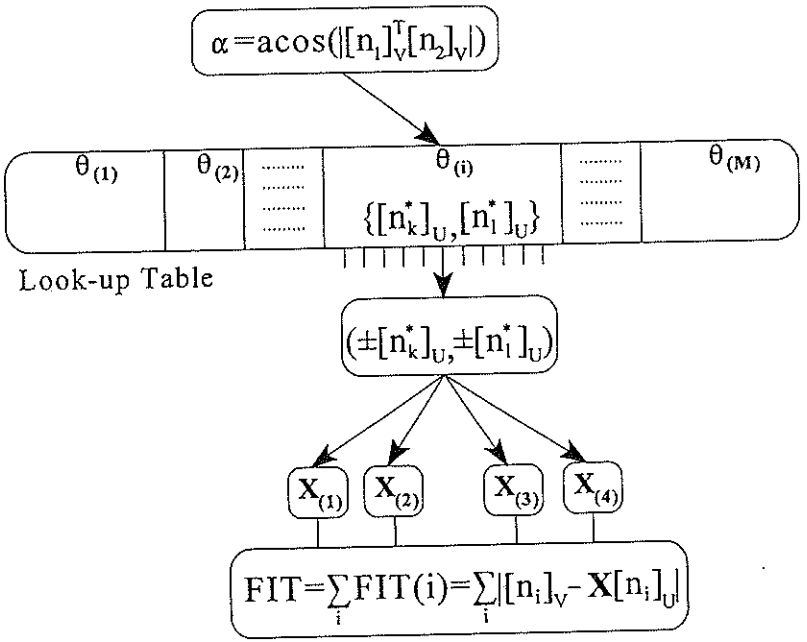

Figure 3.3.1 Schematic illustration of the EBSP indexing procedure.

($\mathbf{n}_1$ and $\mathbf{n}_2$) are rather precisely localized. Otherwise, the procedure will fail since all of the proposed rotation matrices **X** are based on $[\mathbf{n}_1]_V$ and $[\mathbf{n}_2]_V$. In very rare cases it may happen that one or even both of the two first bands, is/are very poorly localized, whereas the rest of the bands are relatively precisely localized. This rare situation may be detected automatically: If some appropriate measure of the pattern quality indicates a good pattern, but the indexing procedure finds only a very poor fit between bands and rotation matrix **X**. When this situation occurs, the crystal plane normal pair ($\mathbf{n}_1$,$\mathbf{n}_2$) should be replaced by ($\mathbf{n}_1$,$\mathbf{n}_3$) or ($\mathbf{n}_2$,$\mathbf{n}_3$), and the indexing procedure repeated.

Obviously, one could think of many modifications and alternatives to the indexing procedure presented above. However, the basic idea of using the first two bands for proposing a number of solutions, and then use the rest of the bands to evaluate these solutions, leads to an efficient and very robust (not sensitive to noisy and erroneous band localization) indexing procedure.

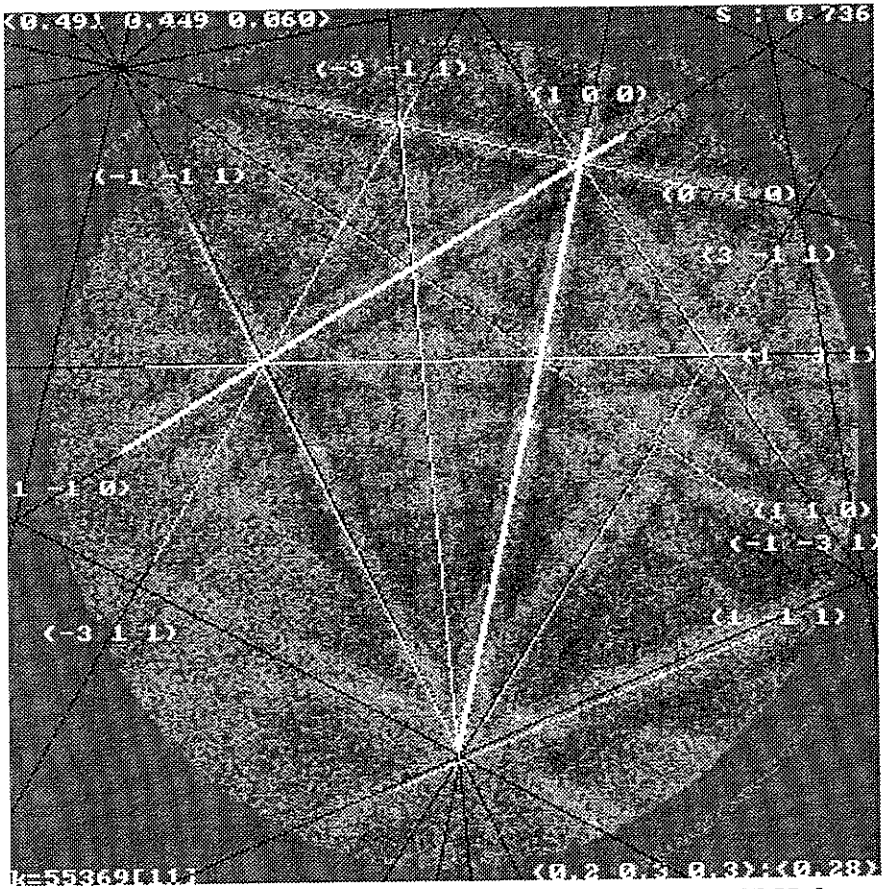

Figure 3.3.2 The indices of 11 manually localized bands in an EBSP from pure copper. The white lines represent the center lines of the bands as they have been localized by the operator, and their corresponding indices are shown in parentheses. The black lines represent the simulated pattern. See the text for further details.

Robustness to noise or errors in the position of the bands is essential in a fully automated EBSP analysis system, where erroneous bands can occur.

As an extension to the procedure, band width information can be employed as an aid in the indexing process as described by Wright & Adams (1992). They classify the bands as either thin or thick, so that - for fcc

symmetry - crystal planes from the families {111} and {200} are classified as thin and planes from families {220} and {113} are classified as thick. It may also be possible to utilize the relative band intensities to a larger extent than in the current indexing routine, where the predicted intensities are used merely to limit the number of crystal plane indices to be considered. By using the information obtained from band widths and/or intensities, indexing becomes easier and fewer possible solutions are to be considered which would speed up the indexing process.

The result of indexing 11 manually localized bands in an EBSP of high quality from pure copper is illustrated in figure 3.3.2. The white lines represent the bands which were localized by the operator, and the black lines represent a simulated pattern based on the crystal plane normals in the look-up table. The two thick white lines represent the bands which were localized first and hence used for determining all the proposed solutions. Note that the indices of the bands, displayed in figure 3.3.2 in parentheses, have been reduced by the largest common divisor; (100) and (110) in figure 3.3.2 thus actually represent reflections from the planes (200) and (220), respectively. The computational costs of the indexing procedure presented here are fairly small, and the typical processing time on a 80486/33MHZ PC is about 2 seconds.

Chapter 4

Automated EBSP Analysis

4.1 Introduction

When on-line analysis of electron backscattering patterns was introduced by Dingley *et al.* (1987), one of the reviewers of that paper, M. Brunner, asked the authors if they believed that a fully automated system could be developed. Their wise though cautious answer to this question was "..., it is not inconceivable that eventually such a system may be developed". Since then, several research groups have worked on furthering the EBSP technique, with the ultimate aim of developing such a fully automated system. The primary obstacle to this development has been the problem of designing reliable image processing routines to detect and localize either the zone axes or the band of EBSPs.

In an early attempt to obtain a fully automated system, the EBSP was compared with a large number of idealized template patterns, and the template which gave the best fit was then chosen to represent the unknown orientation (Wright, Zhao & Adams, 1991). While some promising preliminary results were obtained with this technique, it was never developed further. With the development of an indexing procedure based on the position of bands (Schmidt, Bilde-Sørensen & Juul Jensen, 1991), the main problem now became the development of a reliable technique for detecting and

localizing the center lines of EBSP bands. The first report on such a procedure was given in Juul Jensen & Schmidt (1990). In this procedure the image was first scanned to detect local maxima. The image was then divided into a number of boxes, and a line was fitted to the maxima in each box. Finally, the local lines were combined into global lines representing the center lines of the bands. With this procedure, typically only two to three bands could be detected, and the correct indexing solution, therefore, had to be obtained by checking simulated patterns against the intensities in the image.

In a fully automated system for EBSP analysis presented by Wright & Adams (1992), a line detection scheme known as the Burns algorithm (Burns, Hanson & Riseman, 1986) was employed. In this algorithm local gradient information is first obtained by convolving the image with two differential gradient edge detectors; Wright & Adams (1992) used the very popular Sobel operators (see e. g. Niblack, 1985). The local gradient magnitude and orientation is found from the convolution results, and the basic idea of the Burns algorithm is then to group pixels with similar gradient orientation into so-called line-support regions. Gradient orientation space is coarsely quantized into a small set of intervals, and all pixels are then labelled according to the interval into which the local gradient orientation falls (in practice two overlapping partitions of orientation space are needed to avoid problems introduced by the interval boundaries). A simple connected-components algorithm is then used to form distinct regions of adjacent pixels with the same orientation label, and a line is fit to each region; this can be done by a simple least-squares fit (Wright & Adams, 1992), weighted least-squares using the gradient magnitude as weight or by more sophisticated techniques (Burns *et al.*, 1986). The result of applying the Burns algorithm to an image is thus a number of straight line segments of varying lengths, located more or less precisely at the straight edges of the image, see figure 4.1.3. When applied to EBSP images, the Burns algorithm has the important advantage of relying primarily on gradient orientation and only to a lesser extent on gradient magnitude. This means that even unsharp band edges with low gradient magnitudes have a good change of being detected, as long as the gradient orientations are not varying too much along the band edge. Figure

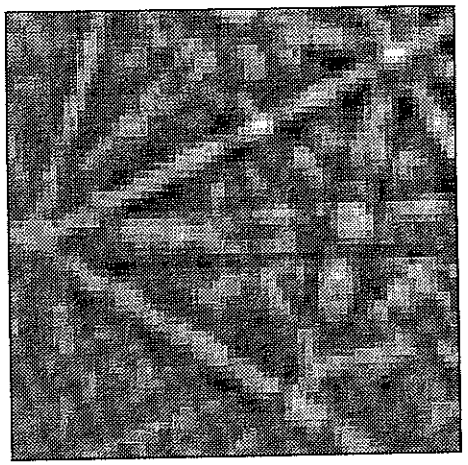

Figure 4.1.1 Typical high quality EBSP from copper.

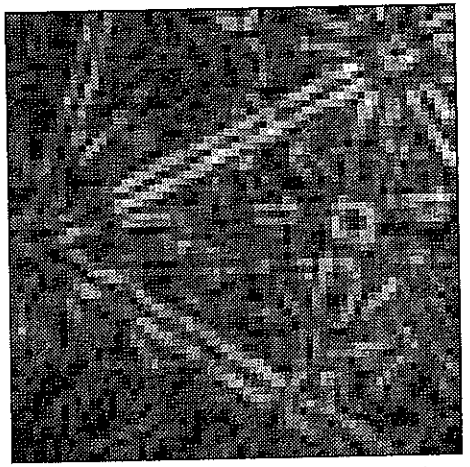

Figure 4.1.2 The gradient magnitude of the image in figure 4.1.1, based on the 3×3 Sobel operators.

4.1.1 and 4.1.2 show a typical high quality EBSP and the corresponding gradient magnitude calculated on the basis of the Sobel operators. Figure 4.1.2 illustrates that the gradient magnitude (the sharpness of the band edges)

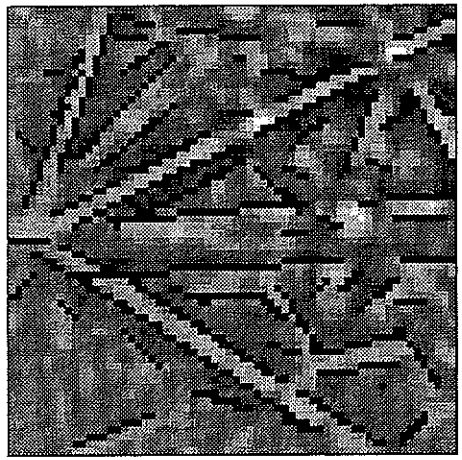

Figure 4.1.3 Straight edge segments detected by the Burns algorithm.

is very weak for all but the 3 or 4 brightest bands. An important disadvantage of the Burns algorithm, in connection with its application to EBSPs, is that it is incapable of utilizing the fact that all band edges must extend across the entire image; the detected line segments must in some way be combined into global lines. Another special feature of EBSPs is the existence of parallel straight edges at both sides of the bands. This fact cannot directly be utilized in the Burns algorithm and similar procedures based on local edge detection, and special post processing procedures must, therefore, be developed to extract parallel pairs of straight edges. Such procedures are described by Wright & Adams (1992), and are shown to be capable of providing the positions of a number of bands with a precision that ensures reliable automated orientation calculations. The typical number of bands that can be localized with this procedure has not been reported.

A completely different approach to automated band localization was presented by Krieger Lassen, Juul Jensen & Conradsen (1992). Instead of focusing on the location of bands edges, this procedure utilizes the increased intensity between the edges to directly locate the center line of the bands. By using the Hough transform (Hough, 1962) of the gray-scale EBSP image, evidence for the presence of bands is effectively and conveniently recorded

in the parameter space of the transformation. In this parameter space which represents to some precision the locations of all possible lines in the EBSP, the bands can be observed as peaks of a size that reflects the width of the corresponding bands. When the parameter space is filtered with a carefully designed "butterfly" mask, the peaks are enhanced and their centers or "focal points" become bettter localized. The center lines of the EBSP bands may then simply be found as the most prominent local maxima of the filtered parameter space, as described in Krieger Lassen *et al.* (1992). Contrary to the Burns algorithm, this procedure effectively utilizes that EBSP bands extend across the entire image, and the center lines of the bands are found in a simple and straightforward manner. The number of bands that can be reliably localized with this procedure varies with pattern quality from about 8 for low quality patterns to about 13 for high quality patterns (in some cases up to 16 reliable bands can be localized, but then - in addition to these - typically one or two non-existent bands are detected). The procedure described in Krieger Lassen *et al.* (1992), Krieger Lassen (1992), Krieger Lassen & Juul Jensen (1993), and Juul Jensen (1993) will be described in much greater detail in the following sections, along with more recent modifications, developments, and suggestions for further improvements.

Recently, the procedure originally described by Krieger Lassen *et al.* (1992) was adopted and slightly modified as described by Kunze, Wright, Adams & Dingley (1993). This paper also presents a comparasion between the Burns algorithm and the Hough transform method, with respect to their ability to correctly localize the bands of EBSPs. The two methods were reported to be almost equally reliable. Their implementation of the Hough transform procedure was, however, reported to be faster than the Burns algorithm and more robust in the case of lower quality patterns. An evaluation and comparison of the precision of the two methods has not yet been performed (see chapter 5 for a thorough discussion on precision).

4.2 Preprocessing of EBSP Images

Prior to any attempt to extract the bands of the digitized EBSP, the image must go through some initial preprocessing steps. Figure 4.2.1 shows

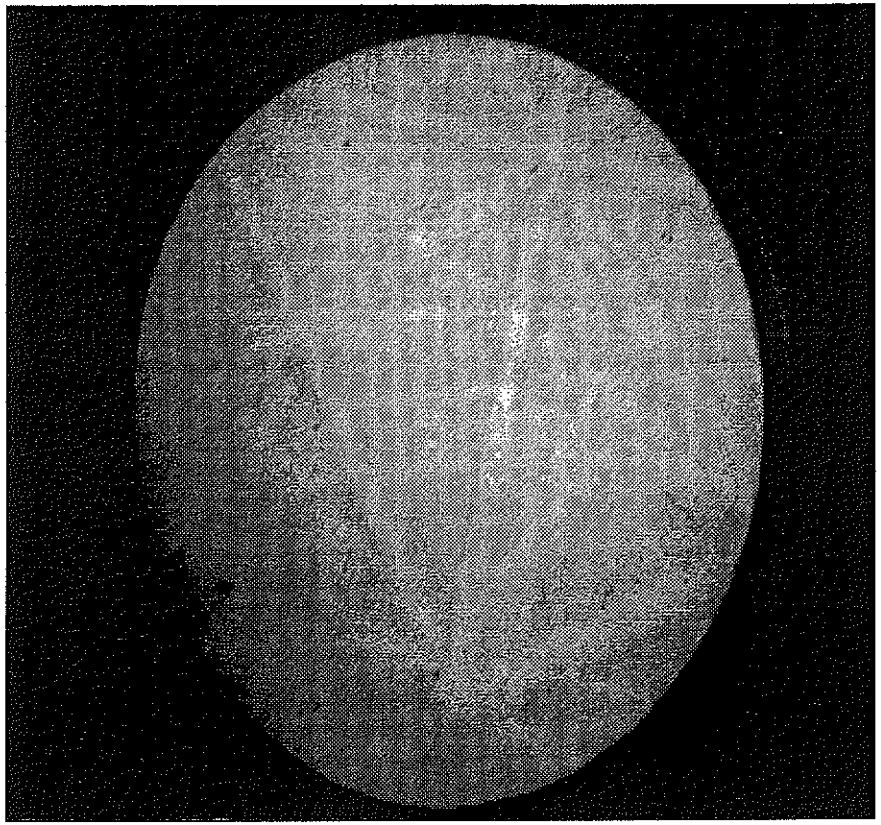

Figure 4.2.1 Raw EBSP image, digitized to 480×512 pixels.

a raw, unprocessed pattern (apart from temporal averaging), digitized to 480×512 pixels. As seen from figure 4.2.1, a substantial part of the image is not covered by pattern information from the phosphor screen, and 56 columns of pixels are therefore removed from both sides of the image. This results in an image with 480 rows and 512−2·56 = 400 columns. It can also be seen from figure 4.2.1 that the information of the raw image is partly hidden by a slow variation in the background gray level. This background variation can - to a large extent - be eliminated by subtracting a background pattern, obtained as the average of the patterns from several individual crystallites. In practice, this average pattern is obtained by operating the SEM

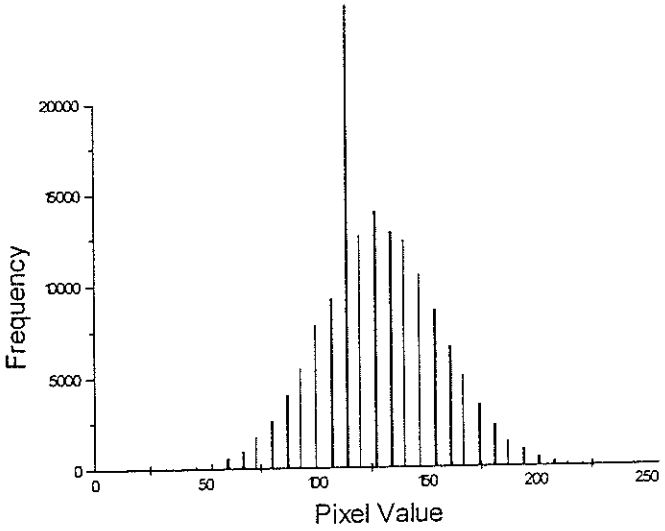

Figure 4.2.2 Histogram of pixel values after subtraction of background image and scaling.

in scanning mode, at a magnification which ensures that a sufficiently large number of crystallites is covered by the electron beam. After subtraction of the background image the pixel values are scaled to lie within the range of one byte (8 bits), i. e. from 0 to 255. The histogram of the pixel values after subtraction and scaling is shown in figure 4.2.2; the peak at pixel value 114 is caused by the pixels outside the phosphor screen. Figure 4.2.2 shows that only a very small fraction of the pixels have values smaller than ~50 and larger than ~200. The contrast of the image can therefore be increased by performing a linear stretch of the pixel values: $I' = 255 \cdot (I - I_{min})/(I_{max} - I_{min})$, where I' is the stretched pixel value, I is the old value and I_{min} and I_{max} could be chosen as 50 and 200 respectively. In practice, I_{min} and I_{max} are chosen as the values which map a certain percentage of the pixels to 0 and 255 respectively. A linear stretch with 0.05% of the pixels (96 pixels) mapped to value 0 and 0.05% mapped to value 255 ($I_{min} = 40$ and $I_{max} = 221$) leads to the histogram seen in figure 4.2.3.

The image obtained by extracting 480×400 pixels from the center of the

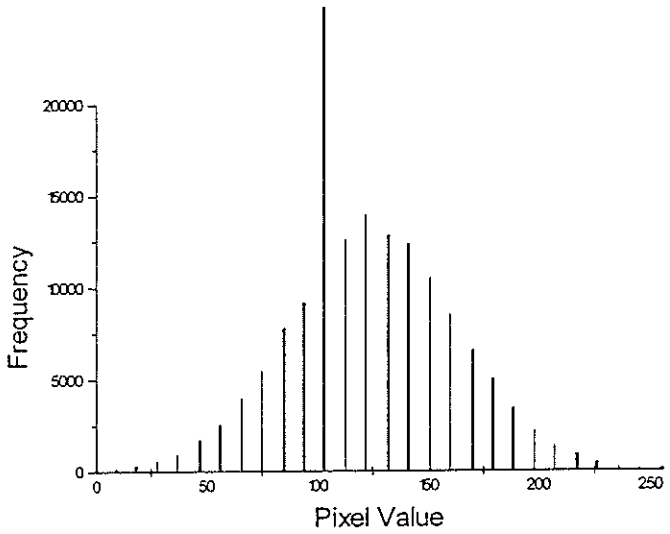

Figure 4.2.3 Histogram of pixel values after subtraction of background image, scaling and linear stretching.

original EBSP (figure 4.2.1), subtracting a background image and stretching the pixel values as described above, must now be corrected to give an aspect ratio of 1. A pixel represents a rectangular physical area □ of size $\Delta x \cdot \Delta y$, where Δx and Δy are referred to as the spatial resolution of the digitized image. The ratio $\Delta y/\Delta x$ is commonly denoted the aspect ratio of the pixels, and if this ration is not 1, the digitizing process introduces a simple distortion of the image. In figure 4.2.1 these distortions are observed as the elliptic appearance of the circular phosphor screen. In our digitizing system the aspect ratio is 1.2, and hence the distortions may be removed by resampling the 480×400 pixel image to a 400×400 pixel image (480/400 = 1.2); this may be accomplished in an efficient way by simply removing each 6'th row of pixels. The result of the preprocessing stages described above is shown in figure 4.2.4.

As the next step of the preprocessing procedure, the resolution of the image is reduced by a factor of four, from 400×400 pixels to 100×100 pixels. This is done simply by partitioning the original image into nonoverlapping

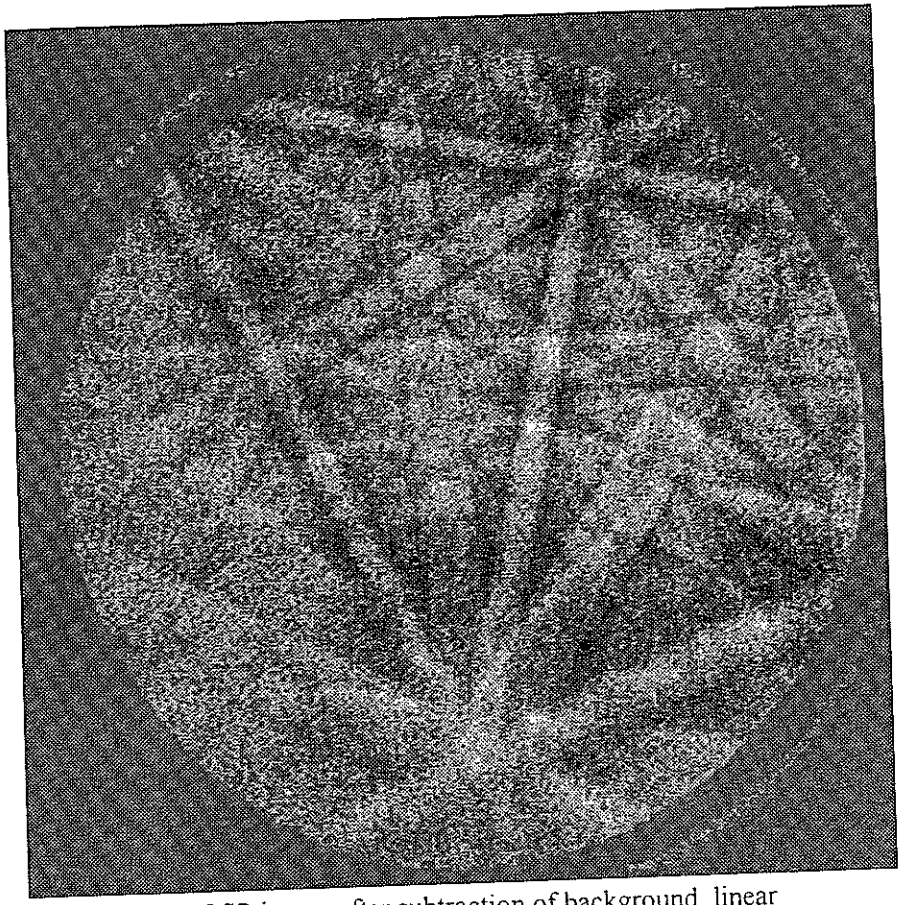

Figure 4.2.4 EBSP image after subtraction of background, linear stretching of pixel values and correction for non-square pixels (400×400 pixels).

neighborhoods of 4×4 pixels, and then replace each of these neighborhoods by a pixel, whose value is the average of the pixel values in that neighborhood; an operation known as consolidation. If the original image is represented by O(r,c), $r \in [0;399]$, $c \in [0;399]$, and the reduced image is R(r,c), $r \in [0;99]$, $c \in [0;99]$, this operation may be written as

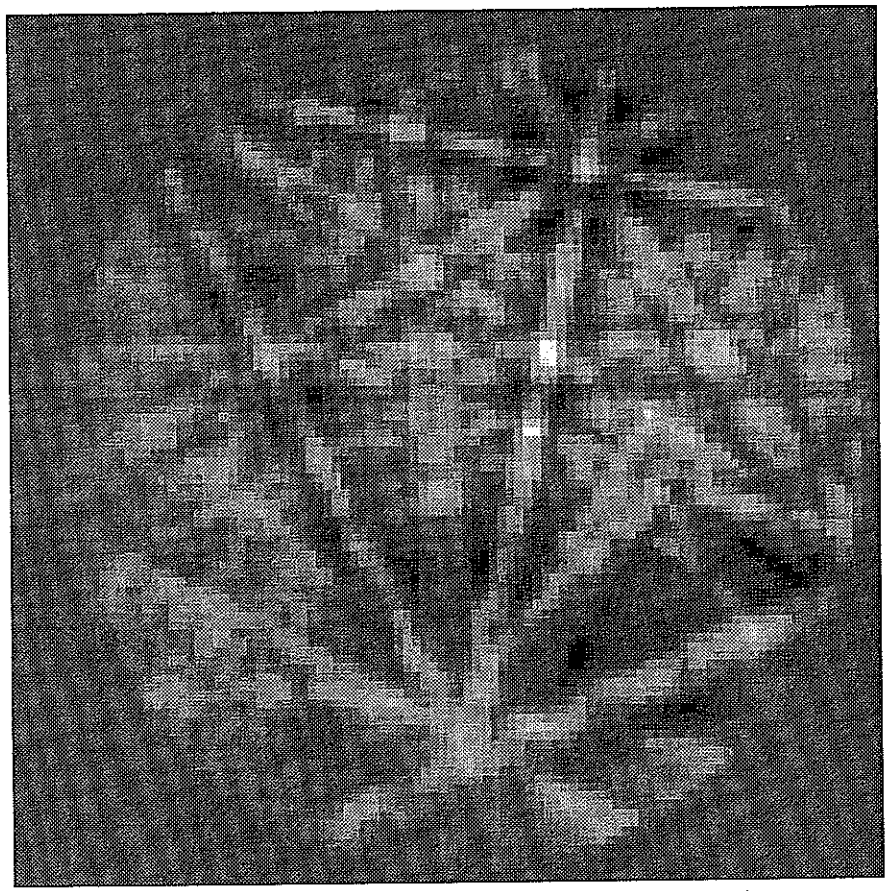

Figure 4.2.5 EBSP image of figure 4.2.4 reduced by consolidation to 100×100 pixels.

$$R(r,c) = \frac{1}{16}\sum_{i=0}^{3}\sum_{j=0}^{3} O(4\cdot r+i\,,\,4\cdot c+j). \qquad (4.2.1)$$

The image of reduced spatial resolution is given in figure 4.2.5.

There are several important reasons why reducing the resolution of a digitized EBSP is beneficial. First of all, it greatly reduces the computational costs of the subsequent calculations. Secondly, it is obvious from figure 4.2.5

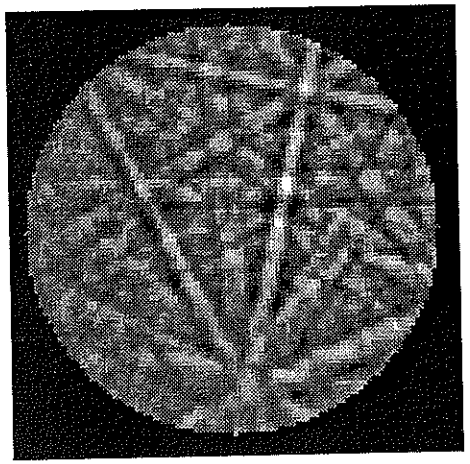

Figure 4.2.6 EBSP image after preprocessing (100×100 pixels).

that the averaging step of the consolidation process removes much of the noise observed at high resolution, figure 4.2.4. It should finally be remarked, that the scale of the image features that we seek to extract, the bands, is such that no significant information is lost as the resolution is reduced.

It is evident from figure 4.2.5 that the image still contains some variations in the background intensity level, and such variations will inevitably have a negative effect on the subsequent processing. These variations can be eliminated to a large extent by subtraction of a low-pass filtered variant of the original. While the low-pass filtering could be performed in the frequency domain (using a discrete two dimensional Fourier transform), it is faster and more convenient to create the low-pass filtered image by simple averaging of pixel values. Hence, the low-pass filtered image L(r,c) is obtained from the original image I(r,c) by averaging over neighborhoods of size N×N,

$$L(r,c) = \frac{1}{N^2}\sum_{i=-N/2}^{N/2}\sum_{j=-N/2}^{N/2} I(r+i\,,\,c+j). \qquad (4.2.2)$$

It was found that N = 11 was suitable for removing the background variations

in the reduced EBSPs (100×100 pixels), however, the value of N is not critical, and values in the range from 9 to 15 may be applied with success. As the final step in the preprocessing of digitized EBSPs the circular region of the image, which contains the pattern information, is cut out, by setting the value of all pixels outside this region to zero. These pixels carry no relevant information, and should therefore be disregarded in subsequent processing. An additional advantage of using a circular image arises in the context of the Hough transform, as described in the following sections. Figure 4.2.6 shows the end result of the preprocessing procedures described above.

4.3 The Hough Transform for Band Localization

4.3.1 Introduction and Background: The Hough and Radon Transforms

The Hough transform (HT) has been recognized as a powerful tool in shape analysis, since it was first introduced by Paul Hough in a patent filed in 1962 (Hough, 1962). It was developed in connection with the study of particle tracks through the viewing field of a bubble chamber, and the method actually represents one of the first attempts to automate a visual inspection task. Hough used the traditional slope-intercept parameterization of lines, $y=mx+c$, which suffers from an unbounded parameter space (m,c) and a singularity for vertical lines, i. e. for $m \to \infty$. This difficulty lead Duda & Hart (1972) to suggest the use of the so-called normal parameterization, which describes the position of a line by its distance ρ from the origin and the orientation θ of its normal vector; this is illustrated in figure 4.3.1.1. It is common practice to restrict θ to the interval $[0;\pi[$ so that ρ can assume both positive and negative values in the interval [-R;R], where R is the distance from the origin to the corners of the image. If the foot of the perpendicular from the origin to the line (the normal point) is in the upper half of the image then $\rho > 0$, otherwise $\rho \leq 0$. Even though many different parameterizations

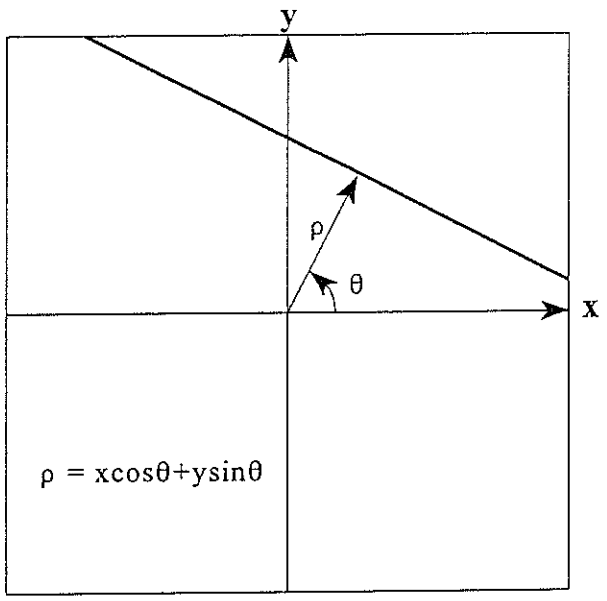

Figure 4.3.1.1 Illustration of the normal parameterization of lines.

of lines have been suggested during the years (see e. g. Risse, 1989), the normal parameterization remains by far the most widely used for line detection via the HT.

In an important paper by Deans (1981), it was pointed out that the Hough transform is actually a special case of the Radon transform (Radon, 1917); a transform which went almost unnoticed for half a century but now is being widely exploited, especially in the field of computerized tomography (Deans, 1983). The Radon transform of a function f(x,y) defined on a two-dimensional Euclidean plane is defined as

$$R(\rho,\theta) = \int_{-\infty}^{\infty}\int_{-\infty}^{\infty} f(x,y)\,\delta(\rho - x\cos\theta - y\sin\theta)\,dx\,dy, \qquad (4.3.1.1)$$

where δ is Dirac's delta function. The delta function forces integration along

the line $\rho = x\cos\theta + y\sin\theta$ (Obviously, Radon did not use Dirac's delta function in his definition of the transform; the delta function was introduced in 1945). The Radon transform yields the projections (line integrals) of the function f(x,y) along all possible lines defined by (ρ,θ). It may be shown that the Radon transform can be computed via the Fourier transform (Deans, 1983). If the continuous function f(x,y) is replaced by a discrete digital image I(x,y) and the continuous parameter space (ρ,θ) is quantized as a digital image, it may be recognized that the Hough transform is essentially a discrete version of the Radon transform. The Radon transform for shapes other than straight lines can be obtained by replacing the argument of the δ function by a function which describes that particular shape.

From the late 70's till today numerous researchers have contributed to the development of the HT and other Hough-like techniques, and comprehensive overviews of this work have been given by Illingworth & Kittler (1988) and more recently by Leavers (1993). See also the first book completely devoted to the subject by Leavers (1992). The HT was originally designed for straight line detection, but has also been successfully applied to the detection of other parameterized objects such as circles, parabolas and ellipses. In a classic paper by Ballard (1981), a Hough-like technique known as the generalized Hough transform (GHT) was developed, which is able to detect arbitrary shapes (shapes which can not be described analytically). See also the book by Ballard & Brown (1982). Probably the most desirable features of the HT is its robustness to noise and occlusion, whereas its principal disadvantages are excessive storage requirements and computational complexity. Much of the work concerning the HT has been devoted to different solutions to these problems.

4.3.2 The Hough Transform for Line Localization

The Hough transform provides an efficient and robust technique for deriving the values of parameters of a model, given a set of points that includes instances of the model. In the present case, the points are the pixels of the digitized EBSP image, and the model is a straight line parameterized by (ρ,θ) in the normal form (Duda & Hart, 1972):

$$\rho = x\cos\theta + y\sin\theta. \qquad (4.3.2.1)$$

The position of the pixels (x_i,y_i) is measured in a Cartesian coordinate system positioned with the origin at the center of the image. Consider a digitized image I(r,c) consisting of N×N pixels with the row and column indices (r,c) ranging from [0;N-1]. The center of the image can then be defined as $(r_0,c_0) = ([(N-1)/2],[(N-1)/2])$, where [z] indicates the largest integer strictly smaller than z. A pixel with row and column indices (r,c) will now be given the index $i = r\cdot N+c$ and the coordinates $(x_i,y_i) = (c-c_0,r_0-r)$.

The essential idea of the Hough transform is illustrated in figure 4.3.2.1 and figure 4.3.2.2. A point (x_i,y_i) in Cartesian coordinates is mapped to all points in the ρ-θ parameter space that specify a possible line through the point. From equation (4.3.2.1) it is evident that this set of lines is represented by a sinusoid $\rho = x_i\cos\theta + y_i\sin\theta$ in parameter space. As illustrated in figure 4.3.2.2, collinear points will map to sinusoids that intersect in a common point and the (ρ,θ) of that point gives the parameters of the line. For the purpose of calculating the Hough transform, the continuous but bounded parameter space must be quantized into an array $H(\rho_k,\theta_l)$ of size M×M. Hence the values of θ are sampled $\theta_l = l\cdot\Delta\theta$, where $\Delta\theta = \pi/M$, and the values of ρ quantized $\rho_k = \rho_0 + k\cdot\Delta\rho$, where $\Delta\rho = \sqrt{2}\cdot N/M$. It was chosen here to use a square array M×M for sampling the parameter space, as this seems appropriate for EBSP images (this is discussed in a later section). The array $H(\rho_k,\theta_l)$, which may be regarded as a digital image in its own right, is now used as an accumulator during the Hough transformation process:

For each pixel (x_i,y_i), $i = 0,\ldots,N^2-1$:
  If $I(x_i,y_i) > 0$ do:
    For each θ_l, $l = 0,\ldots,M-1$:
      Calculate $\rho_k' = x_i\cos\theta_l + y_i\sin\theta_l$
      Add $I(x_i,y_i)$ to $H(\rho_k,\theta_l)$

The value of $\rho_k' = x_i\cos\theta_l + y_i\sin\theta_l$ must be rounded to the closest value ρ_k in the accumulator $H(\rho_k,\theta_l)$.

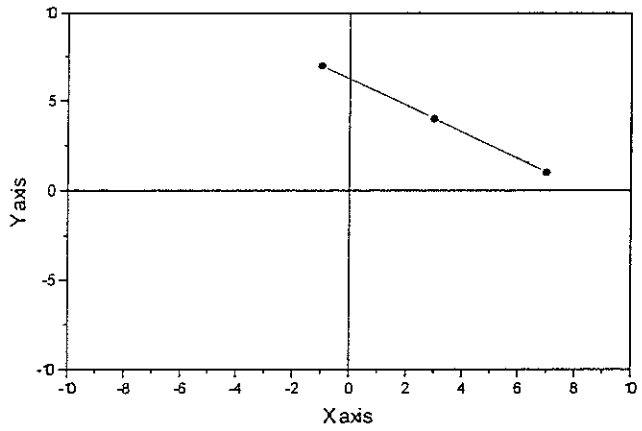

Figure 4.3.2.1 Three collinear points (x_i,y_i) in image space.

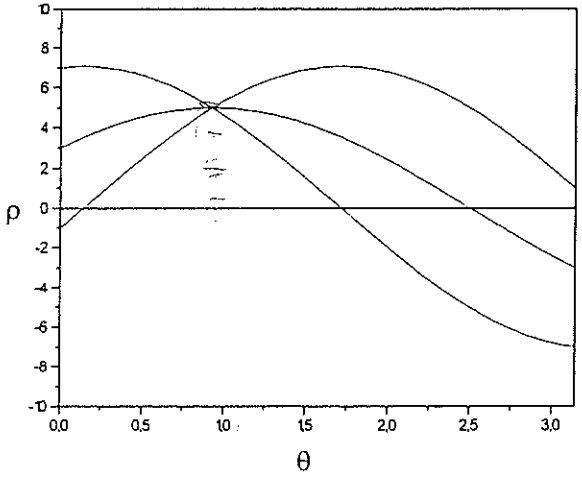

Figure 4.3.2.2 Three sinusoidal curves in Hough space corresponding to the three collinear points in figure 4.3.2.1.

In all traditional applications of the Hough transform, the input image is binary, i. e. I(x,y) = 0 or 1. This binary image is usually obtained by thresholding the output of a mask-based, edge detection operator such as the Sobel (see e. g. figure 4.1.2), so that pixels with value 1 correspond to potential edge points. The fundamental idea behind the procedure described in Krieger Lassen *et al.* (1992) is that the gray-scale pixel values I(x,y) (ranging from 0 to 255) are accumulated in the quantized Hough space, so that I(x,y) serve as a measure of evidence for a line passing through the pixel (x,y). In terms of the traditional HT of binary images, the pixel values I(x,y) serve as weigthing factors in the approach suggested by Krieger Lassen *et al.* (1992). Other authors have suggested the use of weighting factors to the contribution from each pixel (Ballard, 1981; Van Veen & Groen, 1981; Ibrahim, Ngau & Daemi, 1992), but in all of these procedures the factors are based on the magnitude of the edge gradients. Note that using the pixel values in the calculation of the HT requires more processing than the traditional HT, because more pixels are likely to have values larger than 0, and therefore must be considered in the accumulation process.

The HT is often viewed as an evidence gathering procedure. Each pixel votes for all parameter combinations that could have produced it, if it were part of a line. The votes are summed in the accumulator array, and the final totals indicate the relative likelihoods of the different lines. The HT may also be viewed from a slightly different perspective, which clarifies its connection to the Radon transform, equation (4.3.1.1). Each cell of the accumulator array $H(\rho_k,\theta_l)$ defines a line $\rho_k = x\cos\theta_l + y\sin\theta_l$ in the image plane, and the votes accumulated in $H(\rho_k,\theta_l)$ will all originate from pixels along this line. Hence $H(\rho_k,\theta_l)$ is simply the sum of pixel values I(x,y) along the line $\rho_k = x\cos\theta_l + y\sin\theta_l$; a discrete line integral or projection of I(x,y). In fact, one may use this "definition" to calculate the HT, though it is generally less efficient than the procedure given above, because the fact that many pixel values typically are zero cannot be utilized.

The procedure for calculating the Hough transform outlined above is not very computationally effective. For each pixel (x_i,y_i), $i = 0,\ldots,N^2-1$ with $I(x_i,y_i) > 0$, and for each sampled orientation θ_l, $l = 0,\ldots,M-1$, the expression $\rho_k' = x_i\cos\theta_l + y_i\sin\theta_l$ must be evaluated and the corresponding accumulator

array cell $H(\rho_k,\theta_l)$ updated. The most computationally expensive operation is by far the evaluation of $\rho_k' = x_i\cos\theta_l + y_i\sin\theta_l$, which must be performed $M \cdot N^2$ times in the worst case where $I(x_i,y_i) > 0$ for all pixels. For a typical EBSP with N = 100 and a parameter space resolution of M = 120, this basic HT algorithm requires 33.0 seconds of processing time on a 80486/33MHZ PC. A great improvement in speed can be obtained by pre-calculating the values of $\cos\theta_l$ and $\sin\theta_l$ and storing these in two floating point arrays. The total processing time of the HT is then reduced from 33.0 to 6.6 seconds. A further increase in speed can be obtained by pre-calculating the values of $x_i\cos\theta_l$ and $y_i\sin\theta_l$ and storing these in two 2D floating point arrays of size $N \cdot M$. By doing so the evaluation $\rho_k' = x_i\cos\theta_l + y_i\sin\theta_l$ is accomplished by two 2D array look-ups and one floating point addition, and the total computation time is reduced to 4.0 seconds. The speed may be increased even further by first calculating all $\rho_k' = x_i\cos\theta_l + y_i\sin\theta_l$ values and then store the corresponding array indices (ρ_k,θ_l) in one 3D integer array of size $N \cdot N \cdot M$. This array simply contains the positions of all $N \cdot N$ sinusoids (one for each pixel), as they appear in the accumulator array $H(\rho_k,\theta_l)$. With this procedure the HT can be calculated in only 2.0 seconds. An obvious drawback of this procedure is the excessive storage requirements; in the case above with N = 100 and M = 120, $2 \cdot 100^2 \cdot 120/1024^2 = 2.29$MB of free memory is required. In cases where a large number of pixels are known in advance to have the value 0, such as for EBSPs (see figure 4.2.6), the size of the pre-calculated 3D array may be reduced accordingly. For other efficient software implementations of the HT see e. g. Leavers & Sandler (1988) and Koshimizu & Numada (1991).

4.3.3 Removing Inherent Biasing from the Hough Transform

The finite extension of digital images introduces a special artifact into the Hough transform which is commonly referred to as biasing. This effect of finite image size or retina has been considered by several authors, notably Cohen & Toussaint (1977), Van Veen & Groen (1981) and Maitre (1986),

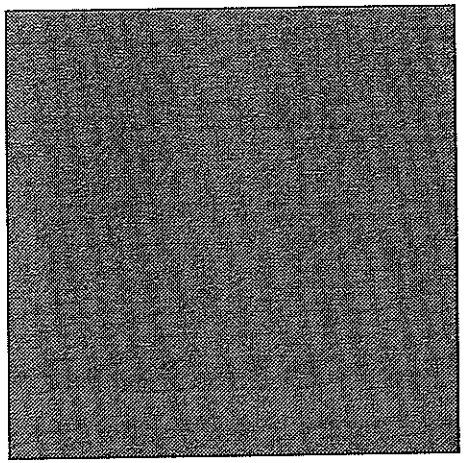

Figure 4.3.3.1 Square image of uniform intensity (100×100 pixels).

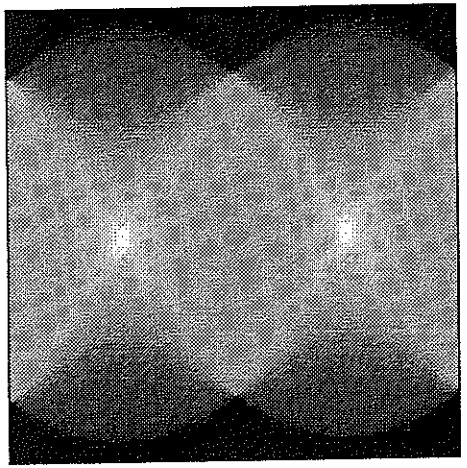

Figure 4.3.3.2 The HT of the image in figure 4.3.3.1 (120×120 pixels).

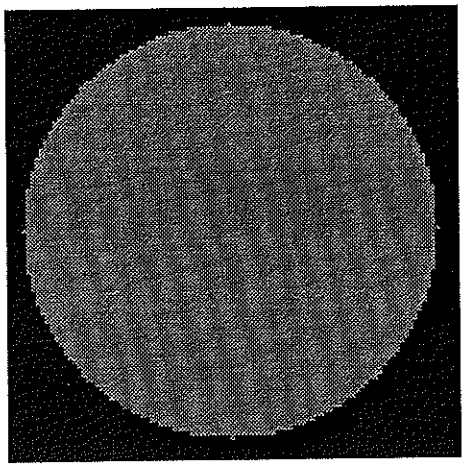

Figure 4.3.3.3 Circular image of uniform intensity (100×100 pixels).

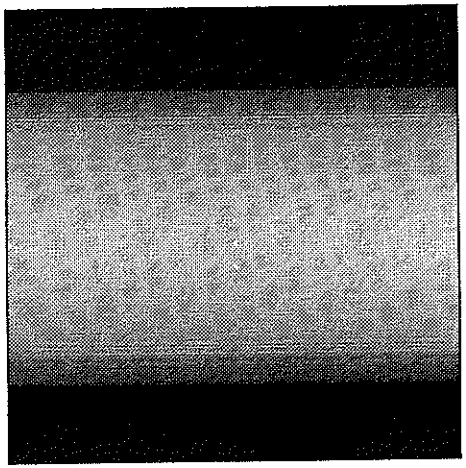

Figure 4.3.3.4 The HT of the image in figure 4.3.3.3 (120×120 pixels).

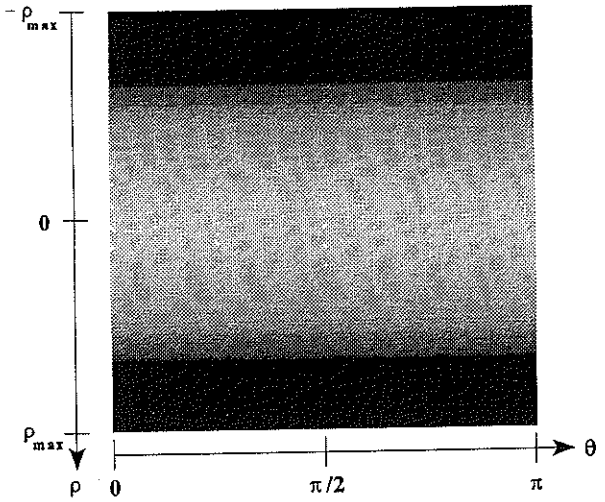

Figure 4.3.3.5 Illustration of the arrangement of the HT accumulator array. Note the direction of the ρ axis.

and is clearly observed in the HT of an image of uniform intensity, see figures 4.3.3.1-4. The arrangement of the Hough arrays $H(\rho_k,\theta_l)$ displayed above, and in the subsequent sections is illustrated in figure 4.3.3.5. Figure 4.3.3.2 and 4.3.3.4 show that a uniform image with a finite retina results in a non-uniform Hough transform with artificial maxima. In the HT of a square image (figure 4.3.3.2) the maxima are located at $(\rho,\theta) = (0,45°)$ and $(\rho,\theta) = (0,135°)$, and thus correspondsto the diagonals of the image. In the HT of the circular image (figure 4.3.3.4) the maxima are located along the line $\rho = 0$, corresponding to all lines passing through the center of the image.

The biasing effect is easily understood by considering the number of pixels that contribute votes to a particular cell of the accumulater array $H(\rho_k,\theta_l)$. Recall that the total sum of votes $\sum I(x,y)$ given to a particular cell (ρ_k,θ_l) origins from pixels along the line $\rho_k = x\cos\theta_l + y\sin\theta_l$. Because of the finite size of the image, the number of pixels lying along a given line (ρ_k,θ_l) will depend on its position and thus on its parameters (ρ_k,θ_l). In the case of a square image the number of pixels lying along a line (ρ_k,θ_l) will depend on both ρ_k and θ_l, as seen from figure 4.3.3.2. An advantage of using a circular

retina is that the number of pixels located along a particular line (ρ_k,θ_l) will depend solely on ρ_k (figure 4.3.3.4) and that the Hough space is bordered by straight lines $\rho = \pm R$, where R is the radius of the circular retina.

In practice, the biasing effect means that lines located near the center of the image will have a greater change of being detected than lines located near the edges. To give all lines an equal opportunity of being detected the biasing effect can be eliminated in a fairly easy way: Construct first an artificial image in which all pixels within the retina have the value one. The HT of this image, denoted $HTB(\rho_k,\theta_l)$, will then in each cell (ρ_k,θ_l) contain the number of pixels which contributed to that cell. By then dividing the total count in each cell of the HT by the corresponding count in HTB, $HT(\rho_k,\theta_l)/HTB(\rho_k,\theta_l)$, the HT is normalized and the biasing removed. In the original HT, the cells (ρ_k,θ_l) contain the sum of pixel values $\sum I(x,y)$ along a given line, whereas the cells of the normalized HT contain the **average** of pixel values $n^{-1}\sum I(x,y)$ along a given line. Note that the two dimensional array for bias correction HTB need only to be determined once for a given retina. The results of bias correction for a synthetic image and a circular EBSP are given below in figure 4.3.3.6-11.

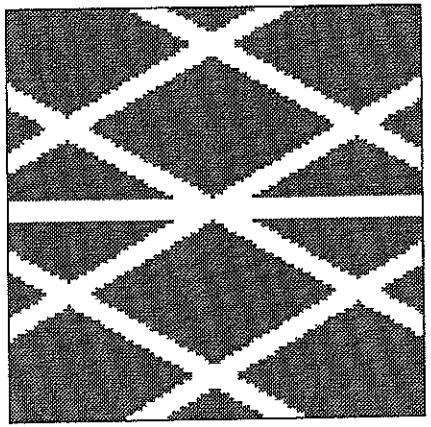

Figure 4.3.3.6 Synthetic image containing 7 bands of 5 pixels width (100×100 pixels).

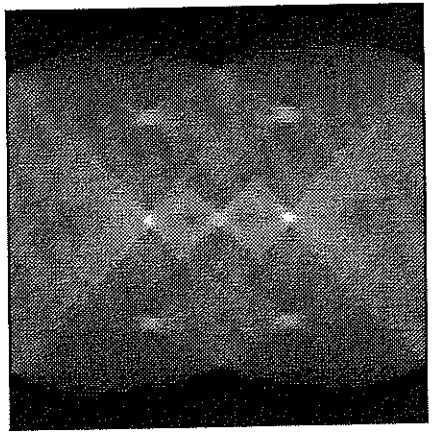

Figure 4.3.3.7 The HT of the image in figure 4.3.3.6 without bias correction (120×120 pixels).

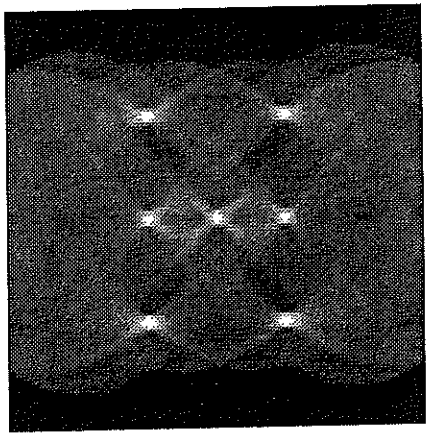

Figure 4.3.3.8 The HT of the image in figure 4.3.3.6 with bias correction (120×120 pixels).

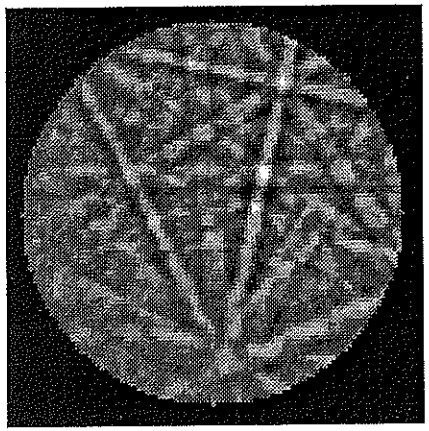

Figure 4.3.3.9 Circular EBSP image from pure copper (100×100 pixels).

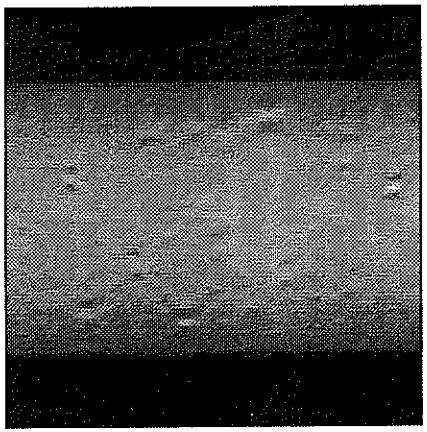

Figure 4.3.3.10 The HT of the image in figure 4.3.3.9 without bias correction (120×120 pixels).

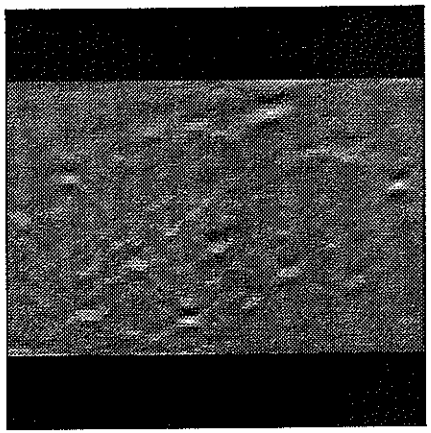

Figure 4.3.3.11 The HT of the image in figure 4.3.3.9 with bias correction (120×120 pixels).

4.3.4 Peak Detection and Localization in the Hough Transform

Once the Hough Transform has been created the pattern of counts in the accumulator array must be analyzed to estimate the presence and location of local peaks or maxima. This problem of detecting clusters in the quantized parameter space is normally solved using a simple approach like the following: Locate the highest peak in parameter space, then the next highest peak, and so on until a sufficient number of objects have been located. For obvious reasons, the problem of detecting local maxima in Hough space has attracted a lot of interest in the literature, see e. g. Leavers & Boyce (1987), Davies (1992), Risse (1989), Princen, Illingworth & Kittler (1990) and Niblack & Petkovic (1990). The main focus of this research has been on reducing the effect of noisy data and on obtaining high precision parameter estimates. However, all of this work has been concerned with the detection of one pixel wide lines in binary images, and therefore is not directly applicable to the detection of EBSP bands, which may be regarded as lines of a width ranging from ~2-10 pixels (in the reduced image of 100×100 pixels). As seen in figure 4.3.3.11, the width of the bands causes a large spreading of the corresponding peaks in the HT, and the positions of local maxima (ρ_i,θ_i) in the Hough space array are not likely to correspond exactly to the center lines of the EBSP bands. This problem is clearly illustrated by the following example. Figure 4.3.4.1 shows an synthetic circular image containing 7 bands of a width of 5 pixels, and figure 4.3.4.2 shows the normalized HT (corrected for biasing) of this image. The local maxima of the HT have been found as indicated by the black circles in figure 4.3.4.2, and the corresponding lines are displayed with black pixels in figure 4.3.4.1. It is evident from figure 4.3.4.1 that the lines obtained as the local maxima of the HT provide rather poor estimates of the parameters of the center lines of the bands. The resolution of the Hough space suggests a precision of $\Delta\theta = \pi/120 = 1.5°$ on the orientation of the lines and a precision of $\Delta\rho = \sqrt{2}\cdot 100/120 \approx 1.18$ pixels on the line location. The orientation resolution of $\Delta\theta$ corresponds

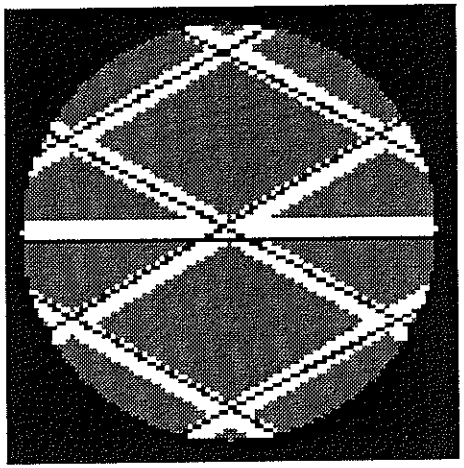

Figure 4.3.4.1 Circular image with 7 bands of 5 pixels width. The black lines correspond to the local maxima in figure 4.3.4.2 (100×100 pixels).

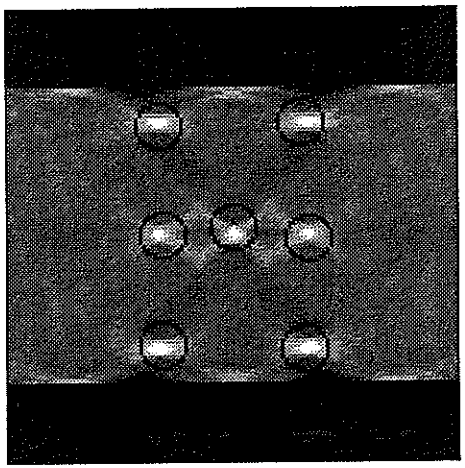

Figure 4.3.4.2 The normalized HT of the image in figure 4.3.4.1. The black circles are centered at the 7 highest local maxima of Hough space (120×120 pixels).

to a distance on the circle sphere of $\Delta d = R \cdot \Delta\theta = 46 \cdot \pi/120 = 1.20$ pixels, where R is the radius of the circle image (for a line passing through the image center). Obviously, the poor localization of the lines/bands in figure 4.3.4.1 cannot be explained from the precision imposed by the quantization of the Hough array.

To devise a method by which the center lines of bands may be extracted from the Hough transform, the shape of the corresponding peaks must be taken into account. The shape and size of peaks in Hough space have been studied by e. g. Leavers & Boyce (1987), Brown (1983), Van Veen & Groen (1981) and Davies (1992), but again these investigations have been limited to the case of lines of one pixel width. The shape of peaks in parameter space generated by bands of width w in image space may be modelled by considering the Radon transform of the 2D function illustrated in figure 4.3.4.3. Figure 4.3.4.3 shows a continuous circular image I(x,y) of radius R, defined where $x^2+y^2 \leq R^2$ and with I(x,y) = 1 within the displayed band and with I(x,y) = 0 elsewhere. The area of the band which falls inside the circular image has been approximated by a rectangle of width w and length $2\sqrt{R^2 - \rho_0^2}$ to simplify the following expressions for the Radon transform. This approximation will be adequate when $w << R$ and $\rho_0 < R-w$, i. e. when the band width is small compared with the size of the image and the band is not too close to the image border. It is easily shown (Deans, 1981) that the Radon transform $R(\rho,\theta)$ of the image above is simply the length of the line $\rho = x\cos\theta + y\sin\theta$ contained within the band (assuming that I(x,y) = 1 within the band). The Radon transform may then - in this case - be calculated on a purely geometrical basis without evaluation of complicated line integrals (equation 4.3.1.1). Relatively simple geometrical computations show that the Radon transform of the image in figure 4.3.4.3 can be partitioned into three distinct regions A, B and C in continuous parameter space (ρ,θ), as shown in figure 4.3.4.4. The three regions A, B and C of the Radon transform of a band of width w are separated by four sinusoid curves [1], [2], [3] and [4] (the curves appear almost as straight lines in figure 4.3.4.4 because this figure only covers a small area of the parameter space around the peak (ρ_0,θ_0), the area of interest). These curves, which

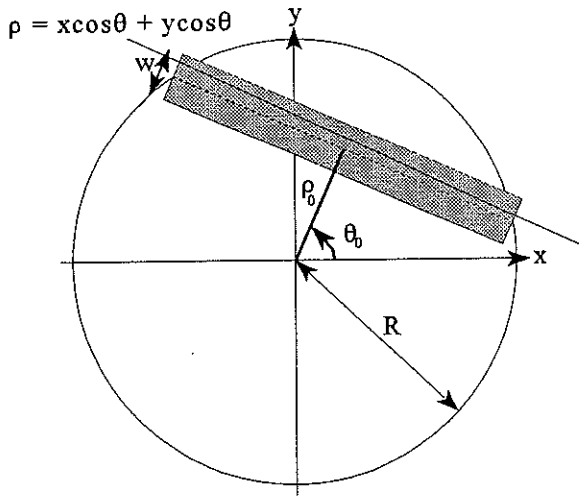

Figure 4.3.4.3 Continuous circular image with band of width w and normal parameters (ρ_0,θ_0) of center line.

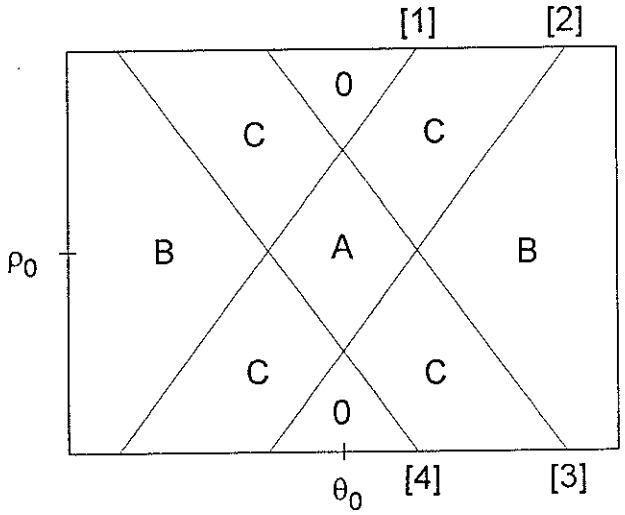

Figure 4.3.4.4 The three basic regions A, B and C of the Radon transform of a band. In the region marked 0, $R(\rho,\theta) = 0$.

correspond to the four corners of the rectangle in figure 4.3.4.3, are given by the following expressions,

$$\rho_{[1]} = (\rho_0 + \frac{w}{2})\cos(\theta - \theta_0) + \sqrt{R^2 - \rho_0^2}\sin(\theta - \theta_0) \qquad \textbf{(4.3.4.1)}$$

$$\rho_{[2]} = (\rho_0 - \frac{w}{2})\cos(\theta - \theta_0) + \sqrt{R^2 - \rho_0^2}\sin(\theta - \theta_0) \qquad \textbf{(4.3.4.2)}$$

$$\rho_{[3]} = (\rho_0 + \frac{w}{2})\cos(\theta - \theta_0) - \sqrt{R^2 - \rho_0^2}\sin(\theta - \theta_0) \qquad \textbf{(4.3.4.3)}$$

$$\rho_{[4]} = (\rho_0 - \frac{w}{2})\cos(\theta - \theta_0) - \sqrt{R^2 - \rho_0^2}\sin(\theta - \theta_0). \qquad \textbf{(4.3.4.4)}$$

In region A of the parameter space where $\rho_{[1]} \le \rho \le \rho_{[2]}$ and $\rho_{[3]} \le \rho \le \rho_{[4]}$ the Radon transform is given by

$$R_A(\rho,\theta) = \frac{2\cdot\sqrt{R^2 - \rho_0^2}}{|\cos(\theta - \theta_0)|}. \qquad \textbf{(4.3.4.5)}$$

Note that the Radon transform within region A only varies with θ and has a minimum at $\theta = \theta_0$ and a maximum where $\rho_{[1]}$ intersects $\rho_{[4]}$ and $\rho_{[2]}$ intersects $\rho_{[3]}$, i. e. for $\theta = \theta_0 \pm \text{atan}(w/2(R^2-\rho_0^2)^{1/2})$. However, the term $|\cos(\theta-\theta_0)|$ of equation (4.3.4.5) only varies slightly within region A and $R_A(\rho,\theta)$ is therefore practically constant. In region B of the parameter space the Radon transform is given by

$$R_B(\rho,\theta) = \frac{w}{|\sin(\theta - \theta_0)|}. \qquad \textbf{(4.3.4.6)}$$

Within region B the Radon transform only varies with θ and has a minimum

at $\theta = \theta_0 \pm \pi/2$ and a maximum for $\theta = \theta_0 \pm \text{atan}(w/2(R^2-\rho_0^2)^{1/2})$, i. e. where region B meets region A (at this point $R_B(\rho,\theta) = R_A(\rho,\theta)$). Region C consists of four distinct regions as illustrated in figure 4.3.4.4 and the Radon transform within each region is given by

$$R_C(\rho,\theta) = \frac{|\rho \pm \sqrt{R^2 - \rho_0^2}\sin(\theta - \theta_0) - (\rho_0 \pm \frac{w}{2})\cos(\theta - \theta_0)|}{|\sin(\theta - \theta_0)\cos(\theta - \theta_0)|}. \qquad \textbf{(4.3.4.7)}$$

Each of the four combinations of signs gives the Radon transform in the corresponding C region. Here the transform depends on both the θ and ρ parameter and has its maxima at $(\rho,\theta) = (\rho_0,\theta_0 \pm \text{atan}(w/2(R^2-\rho_0^2)^{1/2})$, i. e. where region A meets region B and C. Figures 4.3.4.5-6 show the Radon transform of a band as a 3D plot and an image respectively (in practice the figures show a discrete Radon transform, i. e. essentially a Hough transform).

The results above can be used as a guide for choosing an appropriate quantization of the Hough space array $H(\rho_k,\theta_l)$, $\Delta\theta = \pi/M_\theta$ and $\Delta\rho = \sqrt{2}N/M_\rho$. This problem of selecting a proper quantization of the parameter space has been considered by many authors, see e. g. Van Veen & Groen (1981), Risse (1989), Yuen & Hlavac (1991) and Leung, Lam & Lam (1993), but all of this work has been concerned with the detection of one pixel wide lines. The analysis above shows that the size of region A, the central part of the peak, is $S_\rho = w$ in the ρ direction and $S_\theta = 2\text{atan}(w/2(R^2-\rho_0^2)^{1/2})$ in the θ direction. In the discrete Hough space the peak will thus be spread over $n_\rho = S_\rho/\Delta\rho = wM_\rho/\sqrt{2}N$ cells in the ρ direction and $n_\theta = S_\theta/\Delta\theta = 2M_\theta\text{atan}(w/2(R^2-\rho_0^2)^{1/2})/\pi$ cells in the θ direction. A reasonable criteria for choosing M_θ and M_ρ could then be obtained by requiring that $n_\theta = n_\rho$, since this leads to the most compact peaks in Hough space. This requirement leads to the following criteria for M_ρ/M_θ:

$$\frac{M_\rho}{M_\theta} = \frac{2\sqrt{2}N}{\pi w}\text{atan}\left(\frac{w}{2\sqrt{R^2 - \rho_0^2}}\right). \qquad \textbf{(4.3.4.8)}$$

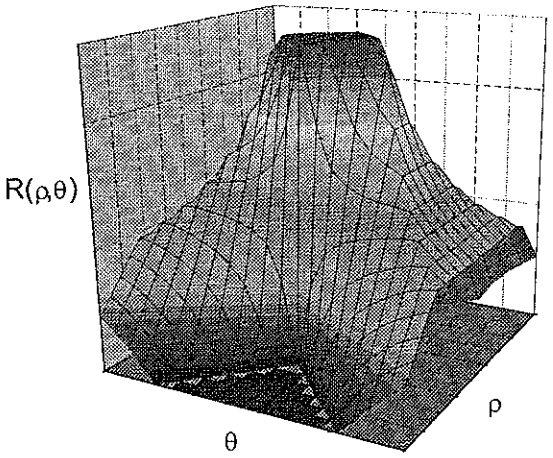

Figure 4.3.4.5 The Radon transform of a band displayed as 3D graph.

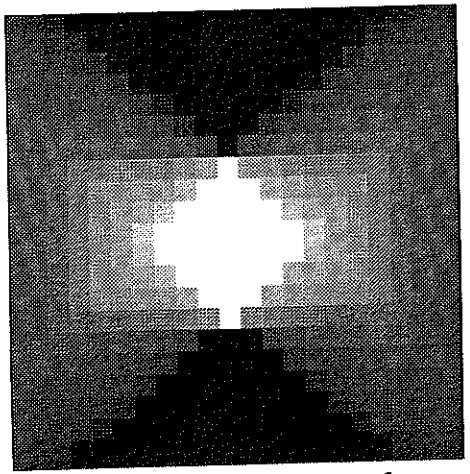

Figure 4.3.4.6 The Radon transform of a band displayed as digital image.

For the EBSP images in our set-up N = 100 and R = 46. For a typical band of width w = 5, equation (4.3.4.8) then gives $M_\rho/M_\theta = 0.978$ for a band passing through the center $\rho_0 = 0$ and $M_\rho/M_\theta = 1.129$ for a band at distance $\rho_0 = R/2$ from the center. This criteria suggests that choosing $M_\rho = M_\theta = M$ is appropriate and results in compact peaks in Hough space. The size of the Hough array M must now be chosen to ensure a reasonable compromise between precision and peak detection sensitivity. A fine quantization (large M) will - at least in theory - enable a more precise band localization, but results in greater computational costs and a larger spreading of the peaks, which complicates their detection. A coarse quantization (small M) will, on the other hand, reduce the precision that can be expected, but results in higher and more compact peaks that are more easily detected. Because EBSP bands can be quite wide and noisy, it seems appropriate to chose M as small as possible, but still large enough to ensure that the peak spread $n = wM/\sqrt{2}N$ is not smaller than one cell for the bands of the smallest width. Since the smallest band width in out set-up is in the order of 1.5 pixels, this criteria suggests a value for M of at least $\sqrt{2}N/w = \sqrt{2}\cdot 100/1.5 = 94$. Even though a quantization of the Hough space with M = 90-100 leads to quite satisfactory results, it was experienced that slightly larger values for M (120-140) resulted in a more precise band localization without significantly reducing the detection sensitivity. A value of M = 120 was found to represent a good compromise between computational load, precision and peak detection sensitivity but the exact value of M is not critical.

The shape and appearance of peaks in Radon/Hough space was studied above (see figure 4.3.4.4-6) for the highly idealized image in figure 4.3.4.3. Obviously, the EBSP band model presented in figure 4.3.4.3 is rather crude and simplified, but it still provides a good qualitative understanding of peak formation in the Hough transform of EBSPs. Figure 4.3.4.6 shows that the peak arising from Hough transformation of a band appears as a butterfly (a term often used in the literature), with its body in section A and its wings in section B and C. This butterfly-like shape is characteristic for all peaks generated by different bands in the image space, but the size of the butterfly will obviously dependent on the band width ($S_\rho = w$). Furthermore, the butterfly shape changes as the distance of the band from the origin ρ_0 changes

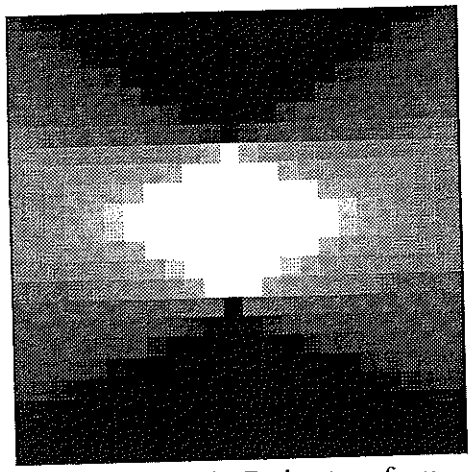

Figure 4.3.4.7 The Radon transform of a band at distance $\rho_0 = 3R/4$ from the image origin.

from 0 to ±R; the width of region A, $S_\theta = 2\text{atan}(w/2(R^2 - \rho_0^2)^{1/2})$ increases with $|\rho_0|$. Figure 4.3.4.7 shows the peak generated by a band localized at a distance $\rho_0 = 3R/4$ from the center and may be compared with figure 4.3.4.6 where $\rho_0 = 0$. It is evident that the butterfly in figure 4.3.4.7 appears slightly squeezed compared with the peak in figure 4.3.4.8, but the general shape has been preserved. Based on similar observations of the butterflies generated by one pixel wide lines, Leavers & Boyce (1987) proposed using a matched butterfly filter for enhancing the peaks in Hough space. By convolving the accumulated Hough space array with the following 3×3 convolution mask

$$\begin{bmatrix} 0 & -2 & 0 \\ 1 & 2 & 1 \\ 0 & -2 & 0 \end{bmatrix}, \qquad \textbf{(4.3.4.9)}$$

the maxima in Hough space with a butterfly-like shape are enhanced at the expense of other maxima (Leaver & Boyce, 1987). This idea was extended to the detection of broad EBSP bands by Krieger Lassen, Juul Jensen & Conradsen (1992), who designed a 13×13 butterfly mask for enhancing the

peaks in a Hough space quantized into 180×180 cells (M = 180). The size of such butterfly masks/templates must be chosen to ensure that a sufficiently large part of the peaks are covered by it, and will therefore depend on both the band width w and the Hough space quantization M. Experiments with masks of different sizes have shown that square masks of size h×h, where $h = 2[Mw/\sqrt{2}N]+3$, are well suited for enhancement of peaks generated by bands of width w in an image of size N×N when the Hough space is of size M×M. Based on the simple model for EBSP bands presented above and the corresponding Radon transform, a number of butterfly masks of different sizes were generated and tested on a number of typical EBSPs. In all cases the ideal bands were assumed to be located at the image center where $\rho_0 = 0$. Since the width of EBSP bands in our set-up varies from ~1.5 to ~10 pixels, it is obviously impossible to design a single mask that will match all the corresponding peaks in Hough space. However, it was found that the following 9×9 convolution mask, designed for optimal performance for w=4 and M = 120, gave good results over a large range of band widths:

$$\begin{bmatrix} -10 & -15 & -22 & -22 & -22 & -22 & -22 & -15 & -10 \\ -1 & -6 & -13 & -22 & -22 & -22 & -13 & -6 & -1 \\ 3 & 6 & 4 & -3 & -22 & -3 & 4 & 6 & 3 \\ 3 & 11 & 19 & 28 & 42 & 28 & 19 & 11 & 3 \\ 3 & 11 & 27 & 42 & 42 & 42 & 27 & 11 & 3 \\ 3 & 11 & 19 & 28 & 42 & 28 & 19 & 11 & 3 \\ 3 & 6 & 4 & -3 & -22 & -3 & 4 & 6 & 3 \\ -1 & -6 & -13 & -22 & -22 & -22 & -13 & -6 & -1 \\ -10 & -15 & -22 & -22 & -22 & -22 & -22 & -15 & -10 \end{bmatrix} \quad \textbf{(4.3.4.10)}$$

Returning to the problem of localizing the seven bands in the synthetic image figure 4.3.4.1, figure 4.3.4.8 shows the normalized HT (corrected for biasing) after convolution with the mask in equation (4.3.4.10). The local maxima of the filtered HT have been found as indicated by the black circles in figure

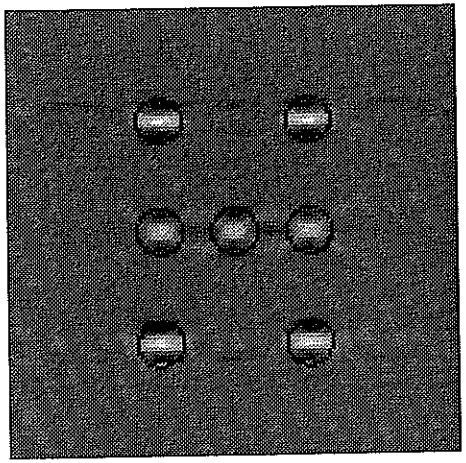

Figure 4.3.4.8 The normalized HT of figure 4.3.4.9 after convolution with butterfly mask. The center of the black circles indicate the local maxima (120×120 pixels).

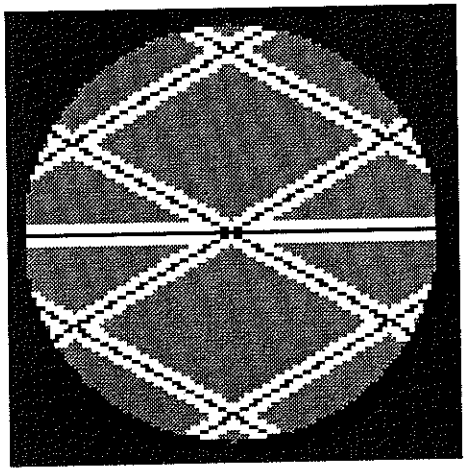

Figure 4.3.4.9 Synthetic circular image with 7 bands of 5 pixels width. The black lines correspond to the local maxima in figure 4.3.4.8 (100×100 pixels).

4.3.4.8, and the corresponding lines are displayed with black pixels in figure 4.3.4.9.

The effect of filtering the HT with the butterfly template is evident in both figures 4.3.4.8 and 4.3.4.9. There are essentially two different advantages of using this matched filtering technique for localizing peaks in the HT: First of all the filtering process reduces the effects of noisy image data by smoothing out any spurious maxima that may be generated by such data (noisy data are unlikely to generate a butterfly peak in Hough space). Secondly, the butterfly template ensures that the maxima after filtering are located at the center of the peaks so that the center lines of the bands are found. This requires, of course, that the filter matches the peaks in the HT; a requirement that can never be completely fulfilled for EBSP images.

When the local maxima of the filtered HT have been located, the precision of the detected lines can be slightly increased by performing a simple interpolation in the Hough space (this was done for the peaks detected in figure 4.3.4.8). It was found that a simple interpolation strategy based on fitting a quadratic polynomial, $y = ax^2 + bx + c$, to the peak $H(\rho_k,\theta_l)$ and its two nearest neighbors in the ρ and θ direction respectively, lead to slightly better results than simply using the maxima. Assume that a local maximum has been detected at (ρ_k,θ_l) and let $x_1 = \theta_{l-1}$, $x_2 = \theta_l$, $x_2 = \theta_{l+1}$, $y_1 = H(\rho_k,\theta_{l-1})$, $y_2 = H(\rho_k,\theta_l)$ and $y_3 = H(\rho_k,\theta_{l+1})$ denote the positions x_i and values y_i of the HT at the maximum and its two nearest neighbors in the θ direction. The interpolating quadratic polynomial going through (x_1,y_1), (x_2,y_2) and (x_3,y_3) is then given explicitly by Lagrange's classical formula (see e. g. Press *et al.*, 1988, pp. 88) and the maximum of this polynomial may then easily be found as

$$x_{max} = \frac{y_1(x_2 + x_3) + y_3(x_1 + x_2) - 2y_2(x_1 + x_3)}{2(y_1 + y_3 - 2y_2)}. \qquad \textbf{(4.3.4.11)}$$

One may then obtain sub-pixel accuracy in the Hough array by using x_{max} as an estimate of the position of the "true" peak in the θ direction. Similar, the position of the "true" peak in the ρ direction may be found from equation (4.3.4.11) when $x_1 = \rho_{k-1}$, $x_2 = \rho_k$, $x_2 = \rho_{k+1}$, $y_1 = H(\rho_{k-1},\theta_l)$, $y_2 = H(\rho_k,\theta_l)$ and

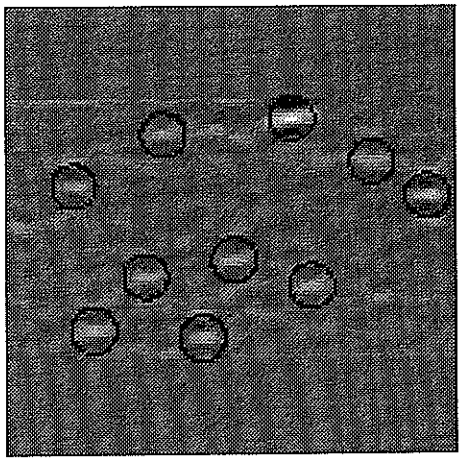

Figure 4.3.4.10 The normalized HT of the EBSP in figure 4.3.4.11 after convolution with butterfly mask. The center of the black circles represents the 10 largest local maxima (120×120 pixels).

$y_3 = H(\rho_{k+1},\theta_l)$. The positive effect of this interpolation strategy is quite significant for thin and bright EBSP bands but becomes less distinct as the width of the bands increase. It was also observed that more complicated interpolation methods involving larger neighborhoods around the peaks did not improve the band localization.

Figures 4.3.4.10-11 show the result of applying the procedure described above for localizing the bands of an EBSP. Note that the detected lines have been displayed in the image of size 400×400 pixels and not in the reduced 100×100 pixel image from which the HT was calculated. The presented result is typical for EBSP of good quality and shows that the vast majority of the bands can be located with a high precision even though the width of the bands is very diverse. However, figure 4.3.4.11 also shows that the thickest bands are significantly less accurately localized than the thinner bands. This is an inevitable consequence of the compromise made in the design of the butterfly mask, and it may be shown that if a larger mask is used (such as the 13×13

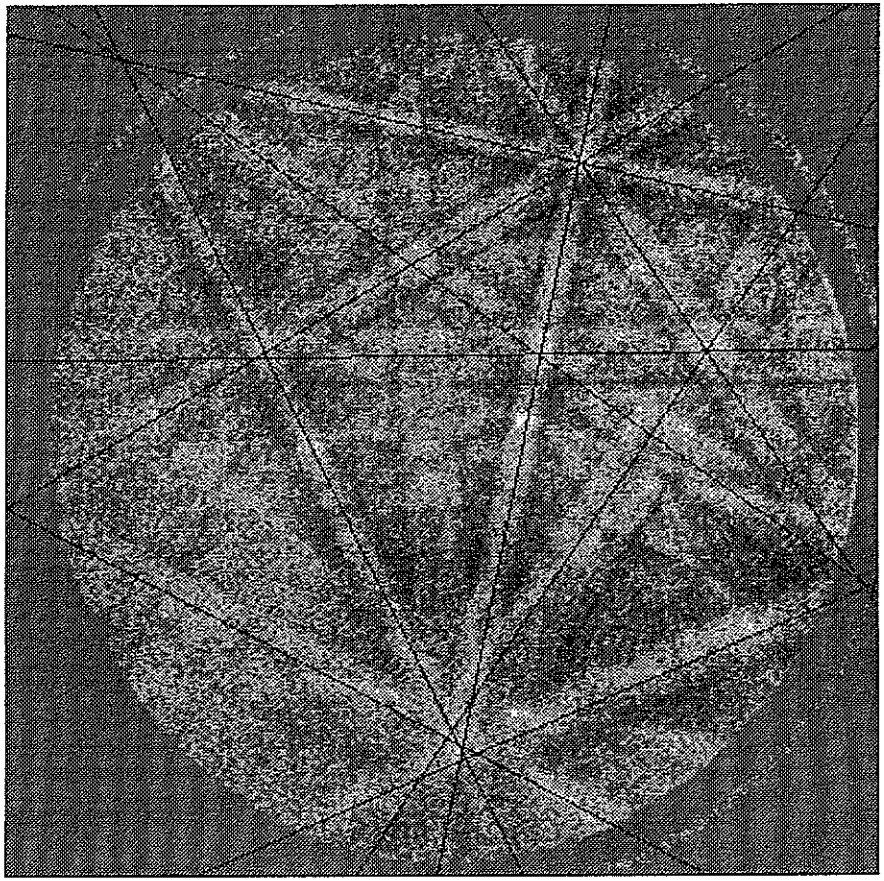

Figure 4.3.4.11 EBSP from pure copper. The black lines correspond to the local maxima in the filtered HT, figure 4.3.4.10 (400 x 400 pixels).

mask proposed in Krieger Lassen, Juul Jensen & Conradsen, 1992), the localization of the wide bands is indeed improved, but at the expense of the localization of thin lines. The Hough transform is renowned for its insensitivity to noisy data, and the filtering of the HT should further reduce the effects of noise. One would therefore expect the presented procedure to work well for EBSP images of low quality. That this is indeed the case is illustrated in figure 4.3.4.12, where 10 bands have been localized in a low quality EBSP from a deformed region in partly recrystallized cobber. Figure 4.3.4.12 shows

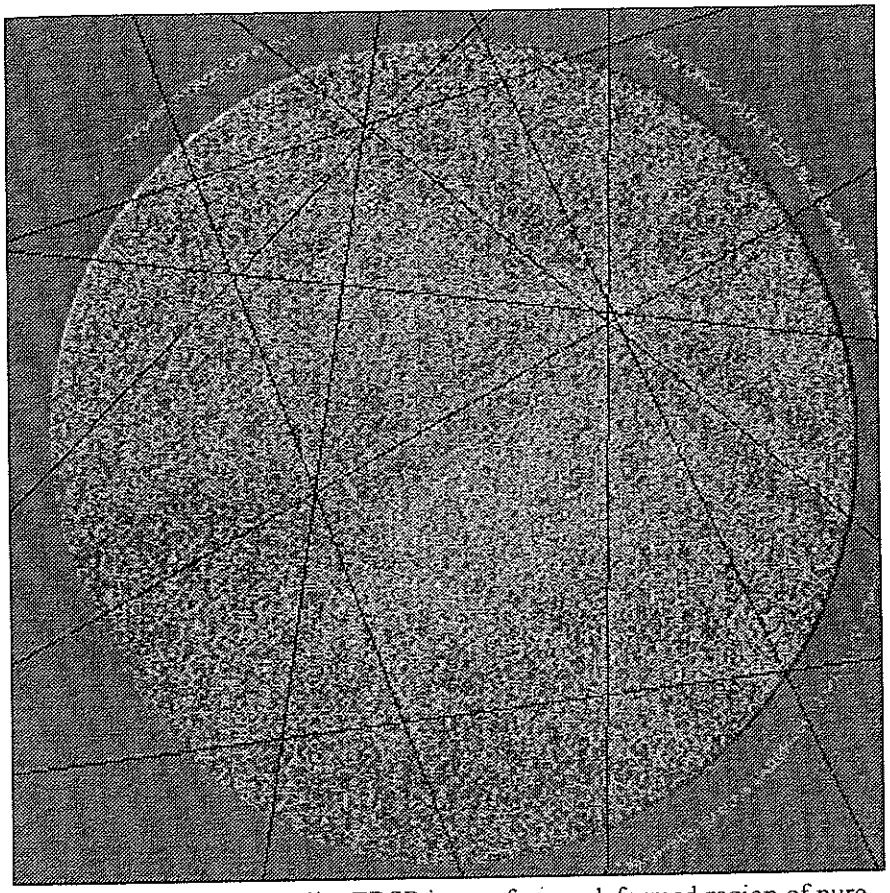

Figure 4.3.4.12 Low quality EBSP image from a deformed region of pure copper. The black lines correspond to the 10 highest maxima in the filtered HT (400×400 pixels).

that even bands, which are hardly recognized by the human eye, can be localized with good accuracy by the procedure (obviously, the accuracy of the band localization is rather difficult to judge by visual comparison in this case). This observation regarding the performance of the procedure for low quality patterns is typical, and in general, the procedure seems to be capable of competing with the human eye with regards to the detection of hardly visible bands.

The procedure presented above is capable of localizing EBSP bands with a precision and reliability that is more than adequate for obtaining a well functioning and reliable fully automated EBSP analysis system. However, there are obviously still parts of this procedure that may be improved upon. The author believes that such improvements should be made in the peak detection part of the procedure; i. e. in the part discussed in this section. For example, it seems obvious that the performance of the procedure could be improved by using butterfly masks of a variable size that would match the size of the actual peaks; i. e. some sort of adaptive template matching. However, it seems difficult to devise ways by which such a procedure could be developed. It seems more likely that an alternative procedure, which is not based on filtering the HT, could be designed. Such a procedure should - in some way - utilize information about the expected peak shape, i. e. be based on an analysis like the one presented above. For example, if the local maxima of the (unfiltered) HT are all found somewhere within region A of the butterfly peak (figure 4.3.4.4), the center of the peaks θ_0 in the θ direction may be found from the expected symmetry around θ_0. Once the center of the peaks in the θ direction has been found, it should be possible to find the corresponding center ρ_0 in the ρ direction by considering the profile of the peak in that direction. This profile should correspond to the profile of the corresponding band (something like figure 2.4.3) and would therefore show a rapid decline at the boarders of the band. The center of the peaks ρ_0 could then be found as the center between the two points in the profile, where the decline has a maximum. This procedure would not only extract information about the center lines of the bands, but would also provide estimates of their width. Initial work with the development of such a procedure has shown promising results, but further details on this work will not be presented here. It may be advantageous to combine the current butterfly filtering approach to peak/band localization, with elements of the procedure sketched above; for example in order to extract band width information.

4.4 A Measure for the Quality of EBSPs

The quality of an electron backscattering pattern may be described by the amount of noise in the image, the contrast of the bands (the band intensity relative to the background intensity), and the sharpness of the band edges. However, the quality of an EBSP is of course a rather subjective concept, which is not easily quantified, unless some strict definition is devised. The quality of EBSPs - as it would normally be defined by a human observer - is affected by many factors: The geometrical set-up (screen position relative to sample), the imaging system (phosphor screen and camera system), the working conditions (e. g. beam current, acceleration voltage), image processing (frame store and frame grabber), and the sample material (surface topography, atomic number, and crystal lattice perfection).

There are several reasons why it would be desirable to have some quantitative measure for the quality of EBSPs. In a fully automated EBSP system, where crystal orientation data is extracted from unsupervised patterns, it is important (in many cases essential) to have an idea of the reliability and precision of the orientation data. It is obvious that the quality of the patterns provides such a measure of data reliability (together with other measures, such as the overall fit between the localized bands and their indices, see section 3.3). Furthermore, the quality of the pattern contains important information about the sample material, which may be utilized in various studies. The quality of EBSPs is namely strongly affected by imperfections in the crystal lattice in which the diffraction process takes place. For example, the EBSP quality can be used to distinguish between recrystallized and deformed regions of material in partly recrystallized samples, because the larger dislocation density in the deformed regions results in a degraded pattern quality. The pattern quality measure presented in this section was partly developed with the intention of performing such investigation automatically (Krieger Lassen, Juul

Jensen & Conradsen, 1993). Other researchers have tried to measure elastic lattice strains on the basis of pattern quality (Wilkinson & Dingley, 1991; Troost, van der Sluis & Gravesteijn, 1993). The quality measure presented here is not intended for use in such investigations.

A measure for the quality of EBSPs intended for use in a fully automated system, must fulfil a few basic requirements: It should be easy to integrate into the automated system, it should require a small amount of computation time only, and it should provide a measure that agrees with the users definition of pattern quality. The measure presented in the following has been found to fulfil these requirements. Initially the digitized EBSP must go through the same preprocessing stages, that were described in section 4.2, i.e. background subtraction, pixel value stretching, correction for aspect ratio, resolution reduction, correction for background intensity variations, and extraction of circular image (figure 4.2.6). For reasons that will later become obvious, an image of 64×64 pixels is extracted from the center of the preprocessed image. Figures 4.4.1 and 4.4.2 show two EBSPs of high and low quality after preprocessing. It is evident from these figures that the image of low quality appears much more noisy than the high quality image, and it seems likely that this difference may be observed in an analysis of the frequency components of the images.

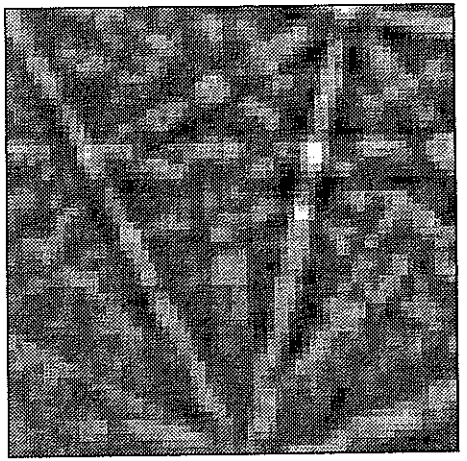

Figure 4.4.1 EBSP of high quality after preprocessing and extraction of 64×64 pixels from image center [Q=0.56].

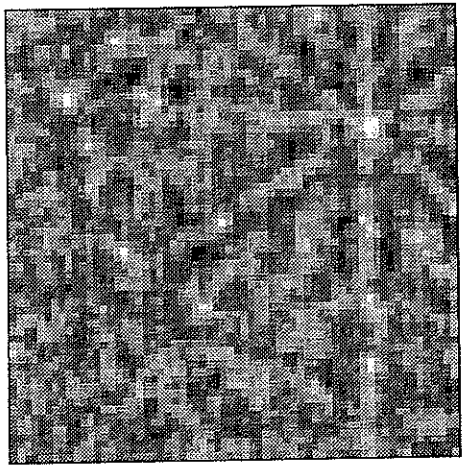

Figure 4.4.2 EBSP of low quality after preprocessing and extraction of 64×64 pixels from image center [Q=0.41].

Such an analysis can be performed via the discrete two dimensional Fourier transform of the image I(x,y)

$$F(u,v) = \frac{1}{n^2}\sum_{x=0}^{n-1}\sum_{y=0}^{n-1} I(x,y)e^{-i2\pi(ux+vy)/n}, \qquad (4.4.1)$$

where n is the image dimension, i. e. n = 64 in this case. Note that n is chosen as a power of 2 so that the Fourier transform may be calculated from the fast Fourier transform (FFT) algorithm, see e. g. Press, Flannery, Teukolsky & Vetterling (1988). The Fourier transform of an image with 64×64 pixels can be calculated via the FFT in only ~0.3 seconds on a standard 80486/33MHZ PC. The magnitude of the complex F(u,v), often referred to as the Fourier spectrum S(u,v), is then found as

$$S(u,v) = |F(u,v)| = \sqrt{[Re(F(u,v))]^2 + [Im(F(u,v))]^2}, \qquad (4.4.2)$$

where Re(F) and Im(F) refer to the real and imaginary part of F, respectively. The logarithm of the spectra of the images in figures 4.4.1 and 4.4.2 are shown in figures 4.4.3 and 4.4.4 respectively (the logarithm is useful for displaying a Fourier spectrum). Both spectra show a decline in the content of low frequency components (the center of the displayed spectra), which is introduced in the preprocessing step, where slow intensity variations are removed by subtraction of a low-pass filtered version of the image. The linear features that are observed in both spectra, but most notably in the spectrum from the high quality image (figure 4.4.3), are introduced by the EBSP bands. It may also be observed from the spectra that the high quality EBSP has a larger content of low frequency components than the low quality EBSP which has a more uniform spectrum. This observation can be clarified by considering the average values of the spectrum in non-overlapping concentric rings centered at the spectrum center (DC), see figure 4.4.5. The average values within each ring (15 rings were used) was calculated for the two spectra, and the result is seen in figure 4.4.6. The figure shows that the EBSP

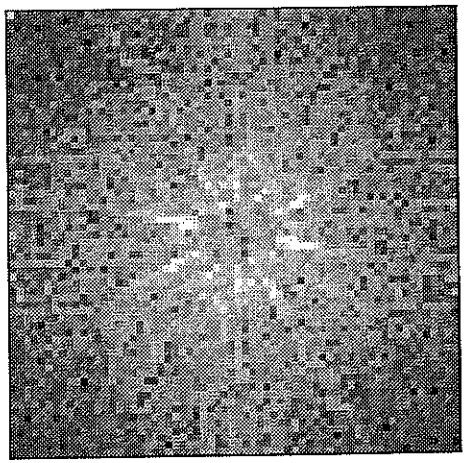

Figure 4.4.3 The logarithm of the spectrum of the high quality image in figure 4.4.1 (64 x 64 pixels).

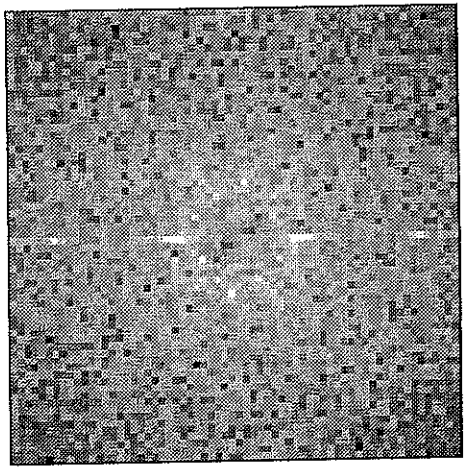

Figure 4.4.4 The logarithm of the spectrum of the low quality image in figure 4.4.2 (64 x 64 pixels).

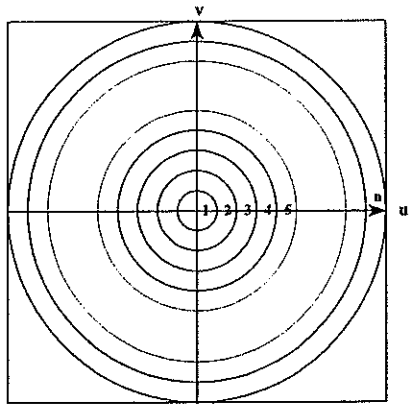

Figure 4.4.5 Partition of Fourier spectrum into n concentric rings.

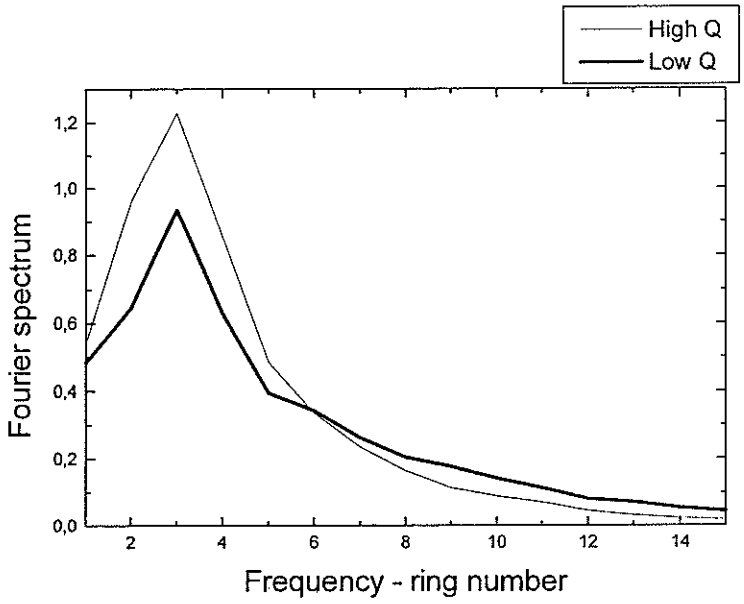

Figure 4.4.6 Average values of the Fourier spectrum in 15 rings for a high and low quality EBSP, respectively.

of high quality has a larger content of low frequency components and a lower content of high frequency components than the poor quality pattern. The frequency content of the low quality EBSP is more uniformly distributed among the different frequency components and is approaching that of white noise. A quantity which seems appropriate for measuring the observed differences in the Fourier spectrum is the inertia I of S(u,v) around the center (u,v) = (0,0) defined by:

$$I = \frac{\sum_{u=-n/2}^{n/2-1} \sum_{v=-n/2}^{n/2-1} S(u,v)(u^2 + v^2)}{\sum_{u=-n/2}^{n/2-1} \sum_{v=-n/2}^{n/2-1} S(u,v)}. \qquad \textbf{(4.4.3)}$$

Note that the inertia of the spectrum (or rather the spectrum itself) has been normalized by the total energy of the spectrum. The inertia decreases as the spectrum becomes successively more concentrated at low frequencies, and should thus be larger for low quality images than for images of higher quality. The theoretical lower bound for the intertia I is 0, which is obtained for a completely uniform image I(x,y) = K, which has a DC frequency component only. A theoretical upper bound for I is obtained when the image contains white noise, and the Fourier spectrum, therefore, becomes uniform S(u,v) = K; the maximum intertia of the spectrum I_{max} is easily found from equation (4.4.3) as

$$I_{max} = \frac{1}{n^2} \sum_{u=-n/2}^{n/2-1} \sum_{v=-n/2}^{n/2-1} (u^2 + v^2). \qquad \textbf{(4.4.4)}$$

The quantity I/I_{max} will then vary from 1 for a white noise image to 0 for a uniform image. As first suggested by Krieger Lassen, Juul Jensen & Conradsen (1993), the following quantity Q may be applied as measure for the quality of EBSPs

$$Q = 1 - \frac{I}{I_{max}}. \qquad (4.4.5)$$

For a white noise image Q = 0. For the EBSP images in our system the lower limit for Q is of the order of 0.3, which is obtained for patterns with no recognizable bands. The upper limit observed for the patterns in our system seems to be around 0.6, which is obtained for patterns of very high quality. The Q values for the images in figures 4.4.1 and 4.4.2 are 0.56 and 0.41, respectively.

The EBSP quality parameter presented above is essentially a measure for the noise level of the images, as it is observed after preprocessing and at the given resolution. It requires very little computation time and is easily integrated into the automated EBSP system, because the required preprocessing is the same as for the band localization procedure. Practical experience with the Q measure has shown that it agrees well with the pattern quality, as it is defined by a human observer. The three EBSPs shown below in figures 4.4.7-9 have Q values lying well spread between the Q values for the two EBSPs shown above, i. e. between 0.41 and 0.56. These three figures, together with figures 4.4.1 and 4.4.2, demonstrate a nice agreement between the visual quality of the images and the corresponding Q values.

The EBSP quality measure presented above may be applied for automatic recognition of deformed and recrystallized regions in partly recrystallized samples. The potential of such a method was investigated in Krieger Lassen, Juul Jensen & Conradsen (1993) for 10 different samples of partly recrystallized aluminium and copper (details are given in the reference above). An experienced operator classified ~100-200 patterns from each sample into two classes: The class of relatively low quality patterns from deformed regions of material, and the class of relatively high quality patterns from recrystallized regions of material. It is important to realize that the operator performs the classification not only on the basis of the pattern quality, but also from the pattern variations observed in the vicinity of the area from which the pattern is obtained (the diffuse patterns from deformed regions of material shift rapidly with relatively small changes in position,

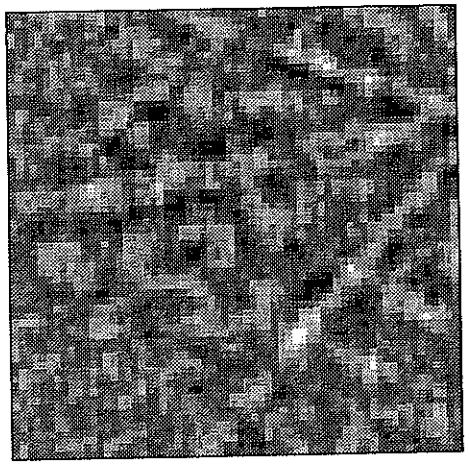

Figure 4.4.7 EBSP after preprocessing and extraction of 64×64 pixels from image center [Q=0.45].

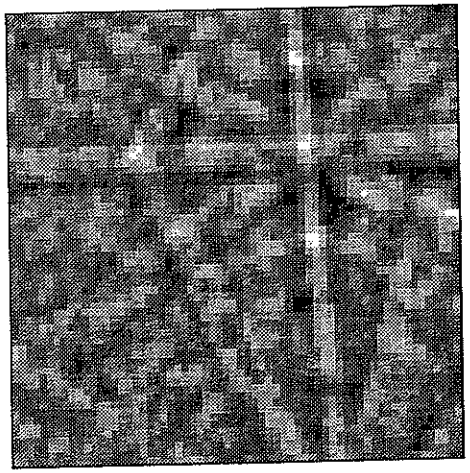

Figure 4.4.8 EBSP after preprocessing and extraction of 64×64 pixels from image center [Q=0.49].

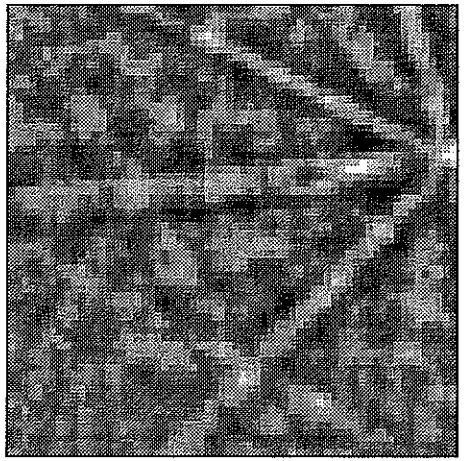

Figure 4.4.9 EBSP after preprocessing and extraction of 64×64 pixels from image center [Q=0.53].

whereas the high quality patterns from recrystallized material remain stable over a relatively large distance; this information is utilized by the experienced operator in the classification process). For each of the patterns which were classified by the operator, the quality measure Q was calculated. The result for 101 EBSPs from an aluminum sample (AA1050, cold rolled 90%, annealed isothermally at 280°C in bath, 39% volume fraction of recrystallized material) is illustrated in figure 4.4.10. This figure clearly illustrates that the patterns from recrystallized regions generally have larger Q values than the patterns from deformed regions of material. However, it may also be observed that the two populations of patterns (● for patterns from recrystallized material, ○ for patterns from deformed material) have overlapping Q values, and it would, therefore, not be possible to obtain a classification based purely on the Q values, which would result in no classification errors; i. e. devise a boundary value Q_0 that would completely separate the two populations. The line marked with an A in figure 4.4.10, indicates the boundary value Q_A, which results in the smallest number of misclassified patterns (the number of white circles above the line plus the number of black circles below the line). For the 10 samples analyzed in

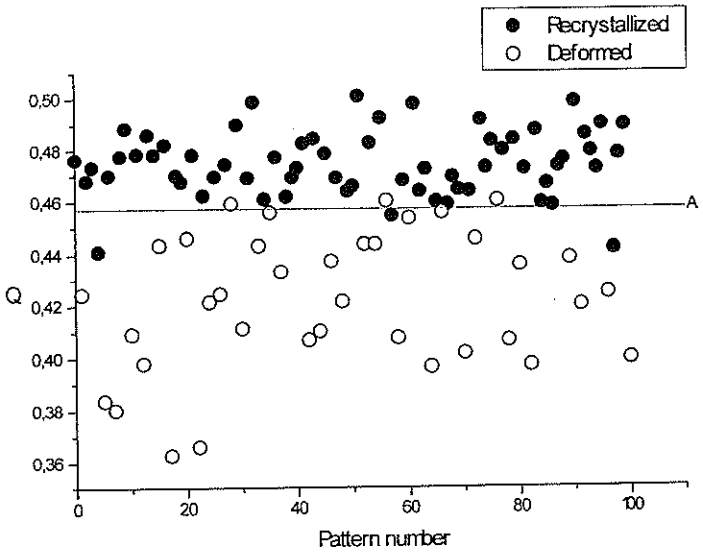

Figure 4.4.10 Quality parameter Q and corresponding classification (indicated by the black and white circles) of 101 patterns from aluminium sample (see text for details). The line marked A indicates the Q value, which results in the smallest number of misclassified patterns.

Krieger Lassen, Juul Jensen & Conradsen (1993) the percentage of misclassified patterns was found to lie from 1.0% to 11.0%. There may be several reasons why the pattern classification performed by the operator is not fully in accordance with the Q measure: As mentioned above, the operator does not base his/her classification entirely on the quality of the patterns, but also on observations of the patterns in the surrounding neighborhood. It must also be noted that a human operator is never perfect; different operators may very well produce diverging classifications, and the same operator may not be consistent. A more general problem is areas of extended recovery, which may often be observed near recrystallization interfaces (Porter & Ralph, 1983), and will produce EBSPs of high quality. Despite these problems, the preliminary investigations presented in Krieger Lassen *et al.* (1993) are promising, and indicate that EBSPs may very well

be used for automated recognition of deformed and recrystallized regions of material. The ideas presented in Krieger Lassen *et al.* (1993) can easily be extended to include more information than merely the pattern quality. If a line scan is made across a partly recrystallized sample, and the step size is chosen appropriately small, recrystallized regions of the sample would be easy to recognize from the high values of Q and the stability of the orientation measurements across the region. By combining the information about position, image quality, and crystal orientation the recognition of deformed and recrystallized regions of material becomes more certain.

The quality measure presented above is, of course, just one of many measures that could be suggested. A natural alternative would be to extract some appropriate measure from the Hough transform of the preprocessed EBSPs. The HT (or rather the normalized HT, see section 4.3) of an EBSP containing pure noise would be practically uniform, whereas the appearance of bands in the EBSP would result in the appearance of butterfly peaks in the Hough space. A quality measure based on the HT should thus in some way measure the "amount" of butterfly peaks in the normalized HT. It was suggested by Kunze, Wright, Adams & Dingley (1993) to simply use the sum of the local peak maxima of HT as a measure for pattern quality. Since the magnitude of a peak in Hough space represents a measure for the average intensity of the corresponding band in the EBSP, this seems like an intuitively appealing measure. In practice, however, the author found this measure to be less satisfying than the measure presented above (it seemed to agree less well with a visual judgement of image quality). The exact implementation of the measure is not quite clear from the paper by Kunze *et al.* (1993), and a fair comparison, therefore, cannot be given here. Another measure for the quality of EBSPs was proposed by Wright & Adams (1992). This measure, which is directly related to the output of the Burns algorithm, was reported to correspond well to a subjective measure of image quality as perceived by the human eye.

Chapter 5

The Precision of Crystal Orientations Determined from EBSPs

5.1 Introduction

The EBSP technique is a powerful tool for measuring the orientation of crystals with high spatial resolution, and it is, of course, of fundamental importance to have knowledge about the precision of the orientation data that can be obtained with this technique. It is important to realize that the orientation of a crystal is not a quantity which can be directly observed but rather must be estimated from data (here the directions of the crystal plane normals). Following standard notation, the unknown rotation matrix describing the crystal orientation is denoted $\mathbf{g}$ and its estimate is denoted $\hat{\mathbf{g}}$. In statistical language, the orientation/rotation $\mathbf{g}$ is an unknown parameter, and its estimate $\hat{\mathbf{g}}$ is subject to error caused by errors in the data. Statistics studies the process by which errors in the data are transmitted into errors in the estimate. Several authors have studied the precision of crystal orientations determined from EBSPs (Venables & bin-Jaya, 1977; Harland, Akhter & Venables, 1981; Dingley, Longden, Weinbren & Alderman, 1987; Schmidt,

Bilde-Sørensen & Juul Jensen, 1991). A general problem in these studies, however, has been a lack of statistical methodology; the uncertainty in the measured orientations was not described in a mathematical stringent way, e.g. by probability distributions or confidence limits. An explanation for this may be that the statistical analysis of data in the form of orientations/rotations is a relatively new discipline in the field of analytical statistics, and the results that have been presented in the literature on this subject (e. g. Downs, 1972; Kathri & Mardia, 1977; Chang, 1986; Prentice, 1986) are not yet widely known outside the statistical community. An introduction to, and the key references for, statistical methods for analyzing orientation data have been presented by Krieger Lassen, Juul Jensen & Conradsen (1994).

Following the notation of section 3.1, U, V and W denotes standard Cartesian coordinate systems fixed to the crystal, the pattern, and the sample, respectively. Let the unit vectors $\mathbf{n}_i$, i = 1,...,n, represent the normal to n crystallographic planes, whose traces are observed in the EBSP. In the following the crystal plane normals measured in U ($[\mathbf{n}_i]_U$), V ($[\mathbf{n}_i]_V$) and W ($[\mathbf{n}_i]_W$) will be denoted $\mathbf{u}_i$, $\mathbf{v}_i$ and $\mathbf{w}_i$, respectively. Recall that the orientation of the crystal is defined as the rotation matrix **g**, which describes the rotation from the sample system W to the crystal system U so that $\mathbf{u}_i = \mathbf{g}\mathbf{w}_i$. The rotation from the crystal system U to the pattern system V is described by **X** so that $\mathbf{v}_i = \mathbf{X}\mathbf{u}_i$, and the rotation from the pattern system V to the sample system W is described by **Y** so that $\mathbf{w}_i = \mathbf{Y}\mathbf{v}_i$. The orientation of the crystal with respect to the sample frame W, its *absolute* orientation described by **g**, is then determined from

$$\mathbf{g} = \mathbf{X}^T\mathbf{Y}^T. \qquad (5.1.1)$$

In practice the rotations **X** and **Y** must be estimated from data as $\hat{\mathbf{X}}$ and $\hat{\mathbf{Y}}$, and the estimate of the absolute crystal orientation **g** is then found as $\hat{\mathbf{g}} = \hat{\mathbf{X}}^T\hat{\mathbf{Y}}^T$. The uncertainty in the estimated orientation $\hat{\mathbf{g}}$, the *absolute* precision of the measured crystal orientations, is given by a family $\Delta\mathbf{g}$ of hopefully small rotations. The rotation matrix **Y**, which describes the rotation between the pattern and the sample system, is constant for a given sample positioned in microscope, and the relative orientations between pairs of crystallites are therefore not affected by it. The uncertainty in the estimated

rotation matrix $\hat{\mathbf{X}}$, given by a family $\Delta\mathbf{X}$ of hopefully small rotations, may therefore be referred to as the *relative* precision of the measured crystal orientations $\hat{\mathbf{g}}$.

The absolute precision $\Delta\mathbf{g}$ of a measured/estimated crystal orientations $\hat{\mathbf{g}}$ may be found as a combination of the precision $\Delta\mathbf{Y}$ of the estimated rotation $\hat{\mathbf{Y}}$ and the relative precision $\Delta\mathbf{X}$ of the estimated rotation $\hat{\mathbf{X}}$. The results presented in the following section will only be concerned with the relative precision, i. e. with $\Delta\mathbf{X}$, and the precision of $\hat{\mathbf{Y}}$ and thus the absolute precision $\Delta\mathbf{g}$ shall only be briefly discussed. The uncertainty in $\hat{\mathbf{Y}}$ is a result of the fact that it is physical impossible to position each sample with its external axes (typically RD, TD and ND) pointing in exactly the same directions relative to some completely fixed axes (typically the directions of the microscope stage). From equation (5.1.1) the rotation matrix **Y** is easily found as $\mathbf{Y} = (\mathbf{X}\mathbf{g})^T = \mathbf{g}^T\mathbf{X}^T$. The uncertainty in $\hat{\mathbf{Y}}$ may then be studied by measuring $\hat{\mathbf{X}}$ and then calculating $\hat{\mathbf{Y}} = \mathbf{g}^T\hat{\mathbf{X}}^T$ several times for the same crystal of known orientation **g**; between each measurement the sample and the phosphor screen are withdrawn from the microscope, the crystal remounted and inserted into, and aligned, in the microscope again. The observed variations in $\hat{\mathbf{X}}$ and therefore in $\hat{\mathbf{Y}} = \mathbf{g}^T\hat{\mathbf{X}}^T$ will thus reflect the uncertainty in $\hat{\mathbf{Y}}$ (**g** is constant). The problem with this method is, of course, that the observed variations in $\hat{\mathbf{X}}$ are not only introduced by variations in the sample alignment, but also caused by the inherent uncertainty in $\hat{\mathbf{X}}$ (discussed in detail in the next section). The uncertainty in $\hat{\mathbf{X}}$ is due to uncertainties in the position of the EBSP bands and the calibration parameters $[\mathbf{t}]_V = (x_0, y_0, -R)$. If the uncertainty in the calibration parameters can be ignored , the problem with the uncertainty in $\hat{\mathbf{X}}$ may - at least to some extent - be overcome by calculating $\hat{\mathbf{X}}$ several times (using many bands, see the next section) and then determine the average rotation $\langle\hat{\mathbf{X}}\rangle$. A procedure for averaging orientations/rotations can be found in Krieger Lassen, Juul Jensen & Conradsen (1994). When the rotation matrix $\hat{\mathbf{Y}} = \mathbf{g}^T\hat{\mathbf{X}}^T$ has been measured several times, the uncertainty in $\hat{\mathbf{Y}}$ can be described by fitting the sample of rotations $\hat{\mathbf{Y}}_i$ to an appropriate probability distribution. This problem, which is far from trivial, is considered in Krieger Lassen, Juul Jensen and Conradsen (1994), and in many of the references given therein

(Khatri & Mardia, 1977; Prentice, 1986; Wood, 1993). An investigation of the precision of $\hat{\mathbf{Y}}$ has not yet been carried out by the author and remains to be performed in the near future.

5.2 The Relative Precision of Crystal Orientations Determined from EBSPs

The rotation matrix $\mathbf{X}$ describes the orientation of the crystal with respect to the pattern system and can be measured or - in statistical language - estimated from n pairs of unit vectors $(\mathbf{u}_i,\mathbf{v}_i)$, $i = 1,...,n$, representing the crystal plane normals $\mathbf{n}_i$ measured in the crystal frame U and the pattern frame V, respectively. The uncertainty in the estimated rotation matrix $\hat{\mathbf{X}}$ is given by a family $\Delta\mathbf{X}$ of hopefully small rotations and may be referred to as the relative precision of the measured crystal orientations $\hat{\mathbf{g}}$. The crystal plane normals referred to the crystal system $\mathbf{u}_i$ are determined from the corresponding Miller indices $(h_ik_il_i)$, which again has been determined in the indexing process (see sections 3.1 and 3.3). The unit vectors $\mathbf{u}_i$ are thus known precisely, assuming that the indexing has been successful; possible bands which could not be correctly indexed must be eliminated prior to the estimation of $\mathbf{X}$ (see section 3.3). The crystal plane normals referred to the pattern system $\mathbf{v}_i$ are determined from the position of the bands in the pattern and the estimated calibration parameters $[\hat{\mathbf{t}}]_V = (x_0,y_0,-R)$, see equation (3.1.6). Due to the inevitable uncertainty in the position of the bands and the calibration parameters, the unit vectors $\mathbf{v}_i$ are subject to variation or error, but had they been known precisely, there would exist a matrix $\mathbf{X} \in SO(3)$ such that $\mathbf{v}_i = \mathbf{X}\mathbf{u}_i$ for each i. As described in section 3.1, a natural estimate of the unknown rotation matrix $\mathbf{X}$ can be found from the erroneous data $(\mathbf{u}_i,\mathbf{v}_i)$ by minimizing the of sum squared errors SSE(X) defined by

$$SSE(\mathbf{X}) = \sum_{i=1}^{n} |\mathbf{v}_i - \mathbf{X}\mathbf{u}_i|^2. \qquad (5.2.1)$$

The matrix $\hat{\mathbf{X}}$ which minimizes SSE(X) is denoted the least squares estimate of X, and it may be calculated as described in section 3.1.

The uncertainty in $\hat{\mathbf{X}}$ could be studied by repeatedly pointing out a number of bands in the EBSP, and then observe the resulting spread in the least squares estimates $\hat{\mathbf{X}}$. Such an approach has, however, several important limitations: First of all, some appropriate strategy for selecting the bands is needed; which, and how many bands should be used? If, for example, only two bands are used, the observed spread in the values for $\hat{\mathbf{X}}$ will be smaller if the same pair of bands is used repeatedly (e. g. $\{\mathbf{v}_i,\mathbf{v}_2\}$), than if different band pairs are used (e.g. $\{\mathbf{v}_i,\mathbf{v}_2\}$, $\{\mathbf{v}_i,\mathbf{v}_3\}$, $\{\mathbf{v}_2,\mathbf{v}_3\}$, ...). The reason for this is that, if the same pair of bands is used repeatedly, the spread in $\hat{\mathbf{X}}$ will only reflect the errors in band localization. If instead different band pairs are used, both the effect of errors in band localization and calibration parameters are observed (errors in the calibration parameters affect the vectors $\mathbf{v}_i$). Alternatively, one could choose to use repeatedly all of the bands that can be localized with a reasonable precision in the EBSP (i. e. the same combination of bands is used in each calculation of $\hat{\mathbf{X}}$). The observed spread in $\hat{\mathbf{X}}$ will then be significantly smaller, than when different combinations of only two bands are used; this seems intuitively reasonable, but is also observed in practice. However, since the same collection of bands is used in each calculation of $\hat{\mathbf{X}}$, the errors in the calibration parameters are not reflected in the observed variations in the estimated X's. A final problem with the approach outlined above is that the observed spread in the estimated X's must be summarized by a statistically meaningful measure of uncertainty, i. e. by the parameters of an appropriate probability distribution or by a confidence region. A different approach to determining the uncertainty in an estimated rotation $\hat{\mathbf{X}}$ is presented in the following. This approach largely eliminates the problems outlined above.

The probability distribution of any estimated parameter and in particular of an estimated rotation $\hat{\mathbf{X}}$, is derived from an assumed probability of the data

$(\mathbf{u}_i,\mathbf{v}_i)$ and the method of deriving the estimate. Consider here the least squares estimate $\hat{\mathbf{X}}$ obtained by minimizing SSE(**X**) defined in equation (5.2.1); other estimates could of course be defined, but the least squares estimate has some attractive mathematical properties. The problem of fitting an unknown rotation **X** to directional data $(\mathbf{u}_i,\mathbf{v}_i)$, where $\mathbf{u}_i \approx \mathbf{X}\mathbf{v}_i$, has some similarity to linear regression problems, e. g. the problem of fitting a set of data points (x_i,y_i) to a straight line model. The problem was therefore named *spherical regression* by Chang (1986), who made a comprehensive study of the statistical properties of $\hat{\mathbf{X}}$. Recent surveys on this subject have been given by Watson (1989) and Chang (1993). In order to make inference about the precision of the least squares estimate $\hat{\mathbf{X}}$ two problems must be solved: First an appropriate representation of the uncertainty in rotations must introduced; i. e. a suitable parameterization of the group of all proper rotations SO(3) must be introduced. This very fundamental problem is discussed in Chang, Stock & Molnar (1990), Hanna & Chang (1990) and Chang (1993). Secondly, a suitable model for the errors in $\mathbf{v}_i$ must be introduced.

Mathematically, a rotation of a 3D object is described by a 3×3 matrix **X** subject to the conditions: $\mathbf{X}\mathbf{X}^T = \mathbf{X}^T\mathbf{X} = \mathbf{I}$, $\det(\mathbf{X}) = 1$, where **I** is the 3×3 identity matrix, and "det" means the determinant. These equations represent six independent conditions on the nine entries of **X**, and hence the matrix **X** is uniquely defined by three parameters. A parameterization of the group of all proper rotations SO(3) (more formally known as the special orthogonal group) is a representation of each matrix in SO(3) by a triplet of numbers; that is, a unique mapping from R^3 to SO(3). Numerous parameterizations of a rotation exist, including e. g. the very popular Euler angles, unit length or normalized quarternions or the exponential parameterization, which will be used in the following. Let $\mathbf{h} \in R^3$ be a 3×1 parameter vector whose coordinates are (h_1,h_2,h_3). This vector is mapped by ϕ to a rotation $\phi(\mathbf{h}) \in SO(3)$ which represents right-hand rule rotation of $\omega = |\mathbf{h}| = (h_1^2+h_2^2+h_3^2)^{1/2}$ radians around the axis $\mathbf{h}/|\mathbf{h}|$. Define the skew-symmetric 3×3 matrix **H** by

$$\mathbf{H} = \begin{bmatrix} 0 & -h_3 & h_2 \\ h_3 & 0 & -h_1 \\ -h_2 & h_1 & 0 \end{bmatrix}. \qquad (5.2.2)$$

The exponential map ϕ of **h** is then defined by $\phi(\mathbf{h}) = \mathbf{I} + \mathbf{H} + \mathbf{H}^2/2! + \mathbf{H}^3/3! + \ldots = \exp[\mathbf{H}]$. This sum reduces to (e. g. Altman, 1986)

$$\phi(\mathbf{h}) = \mathbf{I} + \frac{\sin\omega}{\omega}\mathbf{H} + \frac{1-\cos\omega}{\omega^2}\mathbf{H}^2. \qquad (5.2.3)$$

Conversely, given a rotation **X**, the rotation angle ω and the axis $\mathbf{h}/|\mathbf{h}| = \mathbf{h}/\omega$ can be found from

$$1 + 2\cos\omega = \mathrm{Tr}(\mathbf{X})$$
$$\mathbf{X} - \mathbf{X}^T = \frac{2\sin\omega}{\omega}\mathbf{H}. \qquad (5.2.4)$$

The exponential parameterization presented above is generally applicable, but is especially well suited for describing small rotations, i. e. with $\omega = |\mathbf{h}| << 1$ and $\phi(\mathbf{h}) \approx \mathbf{I}$. Note that Euler angle parameters have a singularity at the identity **I** (the null rotation) where the Euler angle $\phi = 0°$ (not to be confused with the exponential map ϕ), and hence is not suitable for parameterizing small rotations. Another important advantage of the exponential parameterization is that it introduces only small distortions to the size and shape of a region of small rotations $\Delta\mathbf{X}$, e. g. those contained within a confidence region. "Shape and size" are properties derived from the notion of distance, and the aim is to find a parameterization with the property that the standard Euclidean measure of distance in parameter space R^3 (e. g. the distance between rotation **A** and **B** is $|\mathbf{h}_A-\mathbf{h}_B|$) corresponds to the "natural" measure of distance D(**A**,**B**) in SO(3). It may be shown (Chang, Stock & Molnar, 1990) that the only "natural" measure of distance between two rotations **A** and **B** is D(**A**,**B**) = rotation angle of $\mathbf{B}^T\mathbf{A}$, and that the exponential parameterization preserves, reasonably faithfully, these distance relationships in regions of small rotations $\Delta\mathbf{X}$.

In order to describe the probable errors in an estimated rotation $\hat{\mathbf{X}}$ in the form of a confidence region, a model for the errors in the data $(\mathbf{u}_i,\mathbf{v}_i)$ must be presented. As described above, the unit vectors $\mathbf{u}_i$ are not subject to error

(assuming a successful indexing), whereas the errors in the $\mathbf{v}_i$ vectors are caused by the inevitable uncertainty in the position of the EBSP bands and in the calibration parameters. While it may be possible to describe the uncertainty in both the position of the bands and in the calibration parameters (e. g. using a Gaussian probability distribution), it is still extremely complicated to describe - analytically - how these errors affect the calculated unit vectors $\mathbf{v}_i$. A model which can be handled analytically and seems suitable for describing the errors in the $\mathbf{v}_i$'s for EBSPs is described in the following. Assume that the $\mathbf{u}_i$'s are known without error and that the $\mathbf{v}_i$'s are symmetrically distributed around $\mathbf{X}\mathbf{u}_i$ for some unknown rotation matrix $\mathbf{X}$; i. e. the distribution of $\mathbf{v}_i$ depends only upon the distance from $\mathbf{v}_i$ to $\mathbf{X}\mathbf{u}_i$, $\mathbf{v}_i^T\mathbf{X}\mathbf{u}_i$. In addition, it is assumed that the $\mathbf{v}_i$'s are independently Fisher distributed $f(\mathbf{v}_i;\mathbf{X}\mathbf{u}_i,k)$ with modal vectors $\mathbf{X}\mathbf{u}_i$ and common concentration parameter k. The Fisher distribution (Fisher, 1953) is widely employed for modelling directional data $\mathbf{x}$ (data in the form of unit vectors, $\mathbf{x}^T\mathbf{x} = 1$) and has probability density

$$f(\mathbf{x};\mathbf{m},k) = \frac{k}{4\pi \sinh k} \exp[k\,\mathbf{m}^T\mathbf{x}] \qquad (5.2.5)$$

with respect to the uniform distribution on the unit sphere S^2 in 3-space. The modal or mean direction $\mathbf{m}$ is the unit vector which maximizes equation (5.2.5) and $k \geq 0$ is a parameter which describes the concentration of $\mathbf{x}$ around $\mathbf{m}$. For $k = 0$, $\mathbf{x}$ is uniformly distributed over the unit sphere S^2. In the case considered here, where the $\mathbf{v}_i$'s are determined from the calibration parameters and the position of EBSP bands, the assumption about Fisher distributed $f(\mathbf{v}_i;\mathbf{X}\mathbf{u}_i,k)$ errors can be shown to be suitable. The Fisher model has been verified by applying different goodness-of-fit tests (both so-called Q-Q plots and more formal procedures have been applied; see for example Fisher, Lewis & Embleton, 1987, pp. 117) to the data sets $(\mathbf{u}_i,\mathbf{v}_i)$ obtained from several different patterns. All such goodness-of-fit tests have shown a nice agreement with the Fisher model. Finally, it will be asssumed in the following that the concentration parameter k is large; that is, the errors in $\mathbf{v}_i$ are small ($\mathbf{v}_i \approx \mathbf{X}\mathbf{u}_i$). Since typical estimates of k are in the order of 3000-20000 for EBSP data, and k values from 10 to 100 usually are assumed to be large, the large k assumption seems appropriate.

On the basis of the model presented above, an approximate confidence region for the unknown rotation $\mathbf{X}$ can now be described using the exponential parameterization. A formal derivation of the error in $\hat{\mathbf{X}}$ is far beyond the scope of this presentation, but can be found in Rivest (1989), see also Chang (1987). First the unknown concentration parameter k of the Fisher distribution must be estimated from the data. For large k, a good approximation to the maximum likelihood estimate of k is (Watson, 1983)

$$\hat{k}_{MLE} = \frac{2n}{\sum_i |\mathbf{v}_i - \hat{\mathbf{X}}\mathbf{u}_i|^2}. \qquad (5.2.6)$$

However, especially for small sample sizes, the least square estimate of k can be substantially biased upwards (i. e. underestimating the errors). For sample sizes less than 16, Fisher *et al.* (1987) proposes instead the following estimate for k

$$\hat{k} = \left(1 - \frac{1}{n}\right)^2 \hat{k}_{MLE}\,, \qquad (5.2.7)$$

where n is the number of data points. Since n, typically, ranges from 2 to 12 for EBSP data (the number of bands used for estimating $\mathbf{X}$), this estimate of the concentration parameter will be used in the following. The estimated concentration parameter of the Fisher distribution $\hat{k}$ is a measure for the uncertainty in the $\mathbf{v}_i$'s and thus for the uncertainty in the calibration parameters and the position of the EBSP bands. While $\hat{k}$ directly affects the size of the confidence region for $\mathbf{X}$, the following matrix Σ will describe the shape of that region

$$\Sigma = \frac{1}{n}\sum_i \mathbf{u}_i\mathbf{u}_i^T. \qquad (5.2.8)$$

This symmetric 3×3 matrix summarizes information about the position of the points $\mathbf{u}_i$ (the vectors $\mathbf{u}_i$ may be regarded as points on the unit sphere).

Let $\sigma_1 \geq \sigma_2 \geq \sigma_3 \geq 0$ be the positive eigenvalues of Σ satisfying $\sigma_1 + \sigma_2 + \sigma_3 = 1$, and let $\mathbf{z}_1$, $\mathbf{z}_2$ and $\mathbf{z}_3$ be the corresponding eigenvectors. The eigenvector $\mathbf{z}_1$ will lie in the center of the points $\mathbf{u}_i$, and the plane defined by $\mathbf{z}_1$ and $\mathbf{z}_2$ will intersect the unit sphere in the great circle which best fits the point $\mathbf{u}_i$. If the $\mathbf{u}_i$'s are uniformly distributed over the unit sphere, $\sigma_1 = \sigma_2 = \sigma_3 = \frac{1}{3}$. A confidence region of $\mathbf{X}$ will now be described as a family of possible rotations $(\Delta\mathbf{X})\hat{\mathbf{X}}$, where $\hat{\mathbf{X}}$ is the least squares estimate of $\mathbf{X}$ and $\Delta\mathbf{X}$ represents a family of small rotations. The collection of small rotations $\Delta\mathbf{X}$ will be described using the exponential parameterization as a region in the parameter space $\mathbf{h} \in R^3$. An approximate $(1-\alpha)$ confidence region for $\mathbf{X}$ is then expressible as the following collection C of rotations (Chang, 1987)

$$C = \left\{ \phi(\mathbf{h})\hat{\mathbf{X}} \mid \mathbf{h}^T(\mathbf{I} - \hat{\mathbf{X}}\Sigma\hat{\mathbf{X}}^T)\mathbf{h} < \frac{3}{n\hat{k}} F_{1-\alpha}(3,2n-3) \right\}, \qquad \textbf{(5.2.9)}$$

where $F_{1-\alpha}(3,2n-3)$ is the $(1-\alpha)$ percentage point of the F distribution with (3,2n-3) degrees of freedom. In other words, the confidence region $C=\{\phi(\mathbf{h})\hat{\mathbf{X}}\}$ consists of all rotations obtainable by taking the estimated rotation $\hat{\mathbf{X}}$ and following it by all small rotation $\phi(\mathbf{h})$, where $\mathbf{h}$ satisfies

$$\mathbf{h}^T(\mathbf{I} - \hat{\mathbf{X}}\Sigma\hat{\mathbf{X}}^T)\mathbf{h} < \frac{3}{n\hat{k}} F_{1-\alpha}(3,2n-3). \qquad \textbf{(5.2.10)}$$

The region of parameter space $\mathbf{h} \in R^3$ satisfying equation (5.2.10) is a solid ellipsoid with axes $\hat{\mathbf{X}}\mathbf{z}_1$, $\hat{\mathbf{X}}\mathbf{z}_2$ and $\hat{\mathbf{X}}\mathbf{z}_3$ and axis lengths $\Delta\omega_i$, i = 1,2,3, given by

$$\Delta\omega_i = \sqrt{\frac{3F_{1-\alpha}(3,2n-3)}{n\hat{k}(1-\sigma_i)}}. \qquad \textbf{(5.2.11)}$$

The lengths of the ellipsoid axes are denoted $\Delta\omega_i$ to emphasize that they represent the uncertainty in $\hat{\mathbf{X}}$ measured in angles of rotation. Note that $\Delta\omega_1 \geq \Delta\omega_2 \geq \Delta\omega_3$ since $\sigma_1 \geq \sigma_2 \geq \sigma_3$. The uncertainty in $\hat{\mathbf{X}}$ is the largest in the

direction $\hat{\mathbf{X}}\mathbf{z}_1$ and the smallest (the confidence region is best constrained) in the direction $\hat{\mathbf{X}}\mathbf{z}_3$.

As an example, consider now the data obtained by automatically localizing and indexing the bands of a high quality EBSP from pure copper. The output of the EBSP analysis is 10 pairs of unit vectors $(\mathbf{u}_i,\mathbf{v}_i)$, i = 1,...,10, and the least squares estimate $\hat{\mathbf{X}}$ of the crystal orientation with respect to the pattern frame V; expressed in Euler angles $\hat{\mathbf{X}}$ is given as $(\varphi_1,\Phi,\varphi_2)$ = (84.10°,16.21°,108.21°). The concentration parameter of the Fisher distribution is then estimated from the data using equation (5.2.7) as $\hat{k}$ = 25832, and the matrix Σ, which describes the distribution of the crystal plane normals $\mathbf{u}_i$ measured in the crystal frame, is found from equation (5.2.8) as

$$\Sigma = \begin{bmatrix} 0.366667 & -0.027273 & 0.027273 \\ -0.027273 & 0.489394 & -0.180303 \\ 0.027273 & -0.180303 & 0.143939 \end{bmatrix}.$$

The eigenvalues of Σ are $(\sigma_1,\sigma_2,\sigma_3)$ = (0.5726,0.3611,0.0663) and since $F_{0.95}(3,17) = 3.20$, the three rotation angles which describe the size of the confidence region are

$$\Delta\omega_1 = \sqrt{\frac{3\cdot 3.20}{10\cdot 25832\cdot(1-0.5726)}} = 0.5343°$$

$$\Delta\omega_2 = \sqrt{\frac{3\cdot 3.20}{10\cdot 25832\cdot(1-0.3611)}} = 0.4370°$$

$$\Delta\omega_3 = \sqrt{\frac{3\cdot 3.20}{10\cdot 25832\cdot(1-0.0663)}} = 0.3615°.$$

By calculating 900 points $\mathbf{h}$ on the surface of the ellipsoid defined by equation (5.2.10), determine the corresponding rotations $\phi(\mathbf{h})\hat{\mathbf{X}}$ on the boarder of the confidence region C and converting all the rotations to Euler angles, a plot of the 95% confidence region for $\mathbf{X}$ in Euler space can be obtained. A scatter plot

of points (represented by small spheres) on the boarder of this confidence region in Euler space is given in figure 5.2.1. Recall, that in the parameter space **h** of the exponential parameterization ϕ, the 95% confidence region is a solid ellipsoid with semi-axes lengths $(\Delta\omega_1, \Delta\omega_2, \Delta\omega_3) = (0.5343°, 0.4370°, 0.3615°)$; i. e. relatively close to a solid sphere. Figure 5.2.1 shows that the Euler angle parameterization introduces a large distortion to the shape of the confidence region. Consider, for example, the rotation $(\varphi_1, \Phi, \varphi_2) = (82.69°, 16.19°, 109.78°)$ located at the boundary of the 95% confidence region. The Euclidian distance from this point in Euler space to the center of the confidence region $(\varphi_1, \Phi, \varphi_2) = (84.10°, 16.21°, 108.21°)$, the estimate of **X**, is 2.11°, which is far more than the rotation angle 0.45° between the two rotations. This clearly illustrates that the Euler angle parameterization is inappropriate for describing the uncertainty in estimated rotations, or, more generally, the distance between rotations.

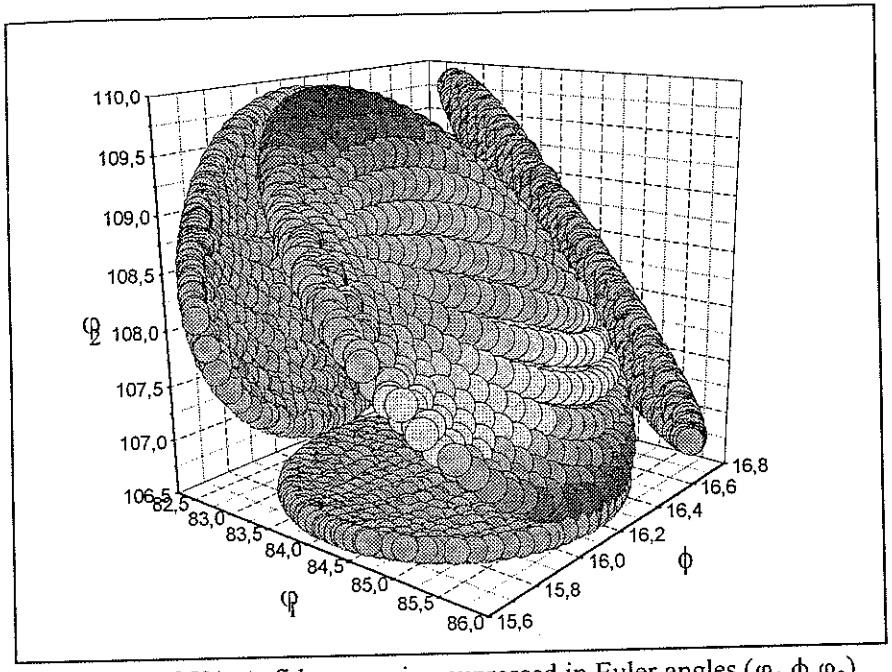

Figure 5.2.1 95% confidence region expressed in Euler angles $(\varphi_1, \Phi, \varphi_2)$ for an unknown rotation **X** determined from 10 bands in an EBSP. The circles represent points on the surface of the confidence region, and the gray areas at the three planes show the projections of the region.

In many cases, it is convenient to summarize the size of the confidence region by a single measure of precision $\Delta\omega$, as an alternative to the three quantities $\Delta\omega_i$. Such a single measure of precision may be obtained from equation (5.2.11) be setting $\sigma_i = 1/3$, which gives

$$\Delta\omega = \frac{3}{\sqrt{2\hat{k}}} \cdot \sqrt{\frac{F_{1-\alpha}(3,2n-3)}{n}}. \qquad \textbf{(5.2.11)}$$

Hence, this "average" measure of precision, corresponds to the situation where $\Delta\omega_1 = \Delta\omega_2 = \Delta\omega_3$ and the points $\mathbf{u}_i$ are uniformly distributed on the unit sphere. For the example considered above, $\Delta\omega = (3/(2\cdot 25832)^{1/2})\cdot(3.20/10)^{1/2} = 0.4278°$.

5.3 Results on the Relative Precision of Crystal Orientations Determined from EBSPs

With the statistical methodology introduced above, it is very simple to determine a statistical measure of the uncertainty in the estimated rotation matrix $\hat{\mathbf{X}}$ for each EBSP, regardless of whether the bands have been localized automatically or by a human operator. Equation (5.2.11) shows that the uncertainty $\Delta\omega$ in $\hat{\mathbf{X}}$, the relative precision of the crystal orientations $\mathbf{g}$, is dependent on the number of localized EBSP bands n and on the their precision, described through the estimated concentration parameter $\hat{k}$. The second factor of equation (5.2.11), which depends solely on n, decreases for increasing n as shown in the table 5.3.1.

n	$\sqrt{\frac{F_{0.95}(3,2n-3)}{n}}$
2	10.3853
3	1.7585
4	1.1629
5	0.9324
6	0.8024
7	0.7158
8	0.6530
9	0.6043
10	0.5654
11	0.5332

Table 5.3.1

If the estimate of concentration parameter of the Fisher distribution $\hat{k}$ is independent of the number of bands n that are being used for estimating $\mathbf{X}$ (e. g. the precision of all $\mathbf{v}_i$'s are the same), the uncertainty $\Delta\omega$ will decrease with increasing n as described by the second column of table 5.3.1. In practice, however, it turns out, that the estimated concentration parameter $\hat{k}$ generally decreases as n is increased; this effect is most significant for low quality EBSPs. The reason for this is quite obvious: The position of the bands located first by either a human operator or by the image processing procedures are likely to be more precise than the bands localized later. This observation about variations in the precision of the $\mathbf{v}_i$'s indicates, that the assumption of a common concentration parameter k in the Fisher model is not entirely true (it would however greatly complicate matters if such variations in k should be incorporated into the modelling of errors; the literature on spherical regression has not yet addressed such

problems). For n fixed, equation (5.2.12) shows that the uncertainty $\Delta\omega$ is inversely proportional to the squareroot of $\hat{k}$, and thus decreases as $\hat{k}$ increases. Since $\hat{k}$ essentially measures how well the unit vectors $\mathbf{v}_i$'s fit the spherical regression model $\mathbf{v}_i = \mathbf{X}\mathbf{u}_i$, any deviations from the model will be reflected in $\hat{k}$. This means that both errors in the calibration parameters (the pattern center and the source point to screen distance) and in the positions of the bands are reflected in the value of $\hat{k}$. Included in the errors in the position of the EBSP bands are the errors introduced by distortions in the camera lens. The significance of these errors is illustrated in figure 5.3.1. The center line of an EBSP band has carefully been located by an operator in figure 5.3.1, but while the line is positioned very close to the center of the band at the two line ends, the line is clearly not in the center of the band at the middle of the line; note the enlarged sub-images placed on top of the original image. These lens distortions, which are most profound at the boarders of the EBSP, will inevitably decrease $\hat{k}$ and increase the expected uncertainty of the estimated rotations **X**.

In order to make inference about the relative precision of crystal orientations determined from EBSPs, 100 patterns from party recrystallized pure aluminium and 100 patterns from partly recrystallized pure copper were analyzed both semiautomatically (with the band positions supplied by an experienced operator) and automatically (with the band positions determined from the image processing procedures described in section 4). The aim was primarily to compare the precision of automated analysis with that of semi-automatic analysis; e. g. to compare the precision of the bands localized automatically with that of the bands located by a human operator. A secondary aim was to study the effects of image quality (quantitatively evaluated by the measure Q presented in section 4.4) and the number of bands used for estimating **X** on the relative precision $\Delta\omega$. For semi-automatic EBSP analysis, all bands that could be localized with a reasonable precision were used; viz. from about 8 bands for patterns of very low quality up to about 11 bands for patterns of higher quality. The center lines of the bands were very carefully localized (i. e. more precisely than during normal operation) and ordered "naturally", with the most prominent bands first. For fully automatic EBSP analysis, the positions of 11 bands were found as the highest local maxima in

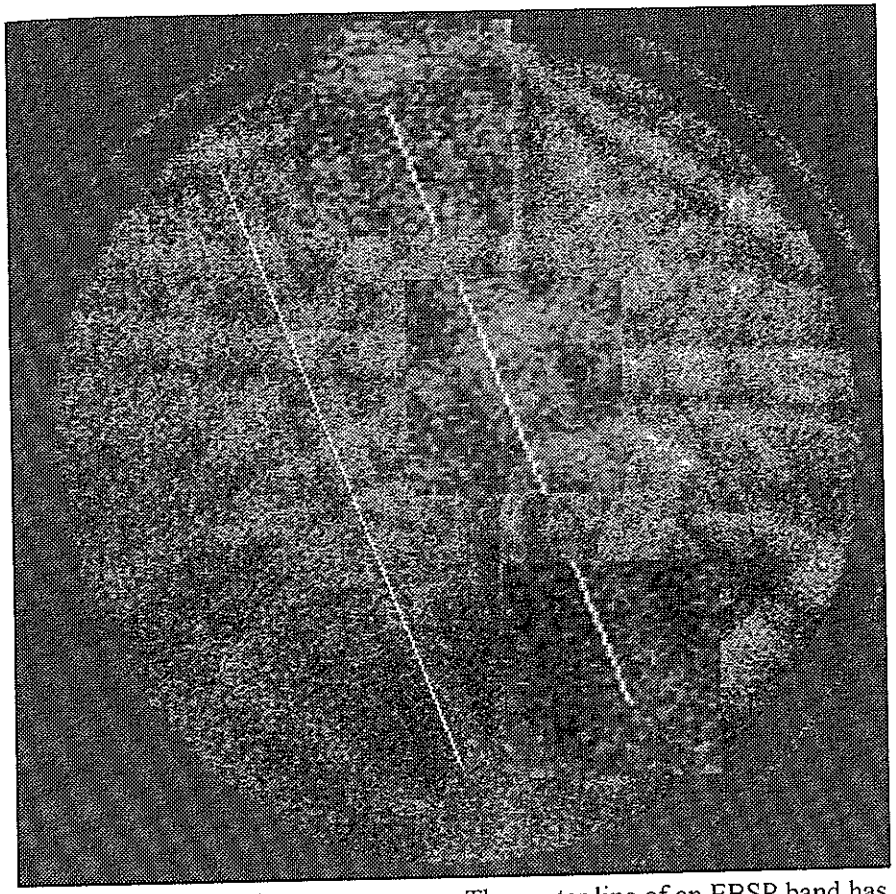

Figure 5.3.1 EBSP from pure copper. The center line of an EBSP band has been localized by an operator. The enlarged sub-images show the position of the line relative to the band at three different positions along the line (400×400 pixels).

the filtered Hough space (see section 4) and ordered according to the peak magnitude; possible erroneous bands were of course disregarded from further processing as described in section 3.3. For each pattern and for each set of manually $\{\mathbf{v}_i\}_M$ and automatically $\{\mathbf{v}_i\}_A$ localized bands, the estimate of the concentration parameter $\hat{k}$ was determined from the first two bands, the first three bands, the first four bands and so on. All estimates of the concentration

parameter $\hat{k}$ where saved to a file together with the number of bands used for the estimate and the EBSP quality parameter Q described in section 4.4. In order to study the effect of Q on $\hat{k}$ (and on the relative precision $\Delta\omega$) the patterns were divided into a number of distinct classes on the basis of their Q values and a number of distinct intervals $[Q_j;Q_{j+1}]$. For each class of patterns with similar Q values, the "average" value of the estimates $\hat{k}$ obtained from the patterns within that particular class was found as

$$\hat{k}_p = \frac{N}{\sum_{i=1}^{N} \frac{1}{\hat{k}_i}}, \qquad (5.3.12)$$

where $\hat{k}_i$, i = 1,...,N, are the estimates of k for the N patterns in a given class. The value $\hat{k}_p$ is a pooled estimate of the common concentration parameter for N samples of data $(\mathbf{u}_i,\mathbf{v}_i)$, when each sample is of the same size; i. e. equation (5.3.12) is only valid when all the $\hat{k}_i$'s are estimated from the same number of bands.

The effect of the pattern quality, described quantitatively by Q, on the relative precision $\Delta\omega$, is visualized in figure 5.3.2 for the 100 EBSP obtained from partly recrystallized pure aluminium. Note, that all the patterns are of a relatively low quality, $Q\in[0.438;0.479]$. The estimates of the concentration parameter k are very uncertain for small n (confidence intervals for k may be described, see e. g. Chang, 1987), and the curves based on only two and three bands are rather uncertain. Typical values for $\Delta\omega$ based on only two bands are 8° and 10° for manually and automatically localized bands, respectively. Figure 5.3.2 clearly displays a strong correlation between the relative precision and the pattern quality measure Q. The relative uncertainty $\Delta\omega$ for both manually and automatically localized bands decreases as the quality parameter Q increases; an effect which is most distinct when the number of bands n is small. Note, that figure 5.3.2 also provides a quantitative indication of the value or validity of the EBSP quality measure Q. Figure 5.3.2 also shows that automatically localized bands are generally less precise than manually localized bands, and generally provide less precise estimates of **X** under the same conditions (the same n and Q). When 10 automatically detected bands

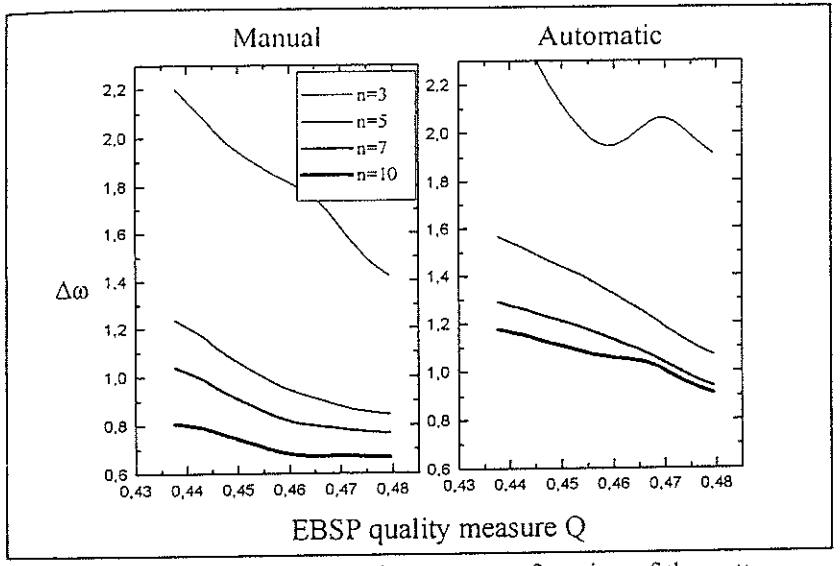

Figure 5.3.2 The relative precision $\Delta\omega$ as a function of the pattern quality parameter Q for 3, 5, 7 and 10 bands respectively. The curves have been determined on the basis of 100 EBSPs from partly recrystallized aluminium.

are being used for estimating **X** (in automated EBSP analysis, the computation time is practically not affected by the number bands that are being localized, and one would therefore choose n large to provide the smallest uncertainty $\Delta\omega$) the relative precision is comparable to the precision obtained, when 5 bands are localized manually. When an operator carefully localizes 10 bands, the uncertainty in **X** is from 0.23° to 0.37° smaller than when **X** is estimated from automatically detected bands. Figure 5.3.3 is similar to figure 5.3.2 but is based on 100 EBSP from partly recrystallized copper. These patterns were generally of a significantly better quality than the patterns from aluminium, and the quality measures Q for the EBSPs were all within the interval [0.498;0.560]. In comparison with the curves in figure 5.3.2, figure 5.3.3 indicates that the influence of the quality parameter Q on the relative precision $\Delta\omega$ is less distinct for patterns of high quality. Especially for automatically localized bands, the uncertainty $\Delta\omega$ decreases only little as the pattern quality

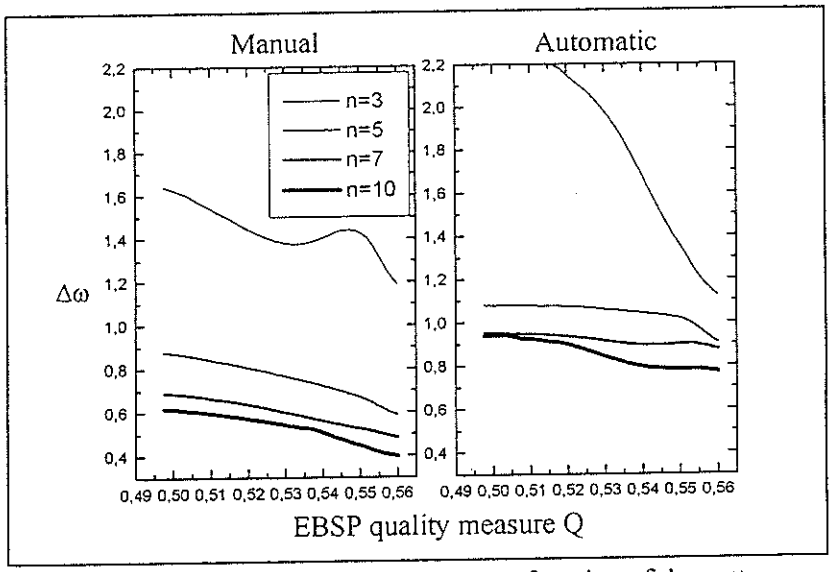

Figure 5.3.3 The relative precision $\Delta\omega$ as a function of the pattern quality parameter Q for 3, 5, 7 and 10 bands respectively. The curves have been determined on the basis of 100 EBSPs from partly recrystallized copper.

measure increases. As with figure 5.3.2, figure 5.3.3 shows that automatically localized bands generally provide less precise estimates of **X** than bands carefully localized by a human operator, assuming identical conditions (the same n and Q). When 10 automatically detected bands are used for estimating **X**, the relative precision is comparable with the precision obtained, when 4 to 5 bands are localized manually. When an operator carefully localizes 10 bands, the uncertainty in **X** is about 0.35° smaller than when **X** is estimated from 10 automatically detected bands.

The effect of the number of bands n on the relative precision $\Delta\omega$ is illustrated in figure 5.3.4 for the 100 EBSPs obtained from partly recrystallized aluminium. As one would intuitively expect, the uncertainty in the estimated rotation **X** decreases rapidly as the number of bands n used for obtaining the estimate is increased. The influence of n on the values for $\Delta\omega$ is observed to be very similar for patterns of varying quality and for bands

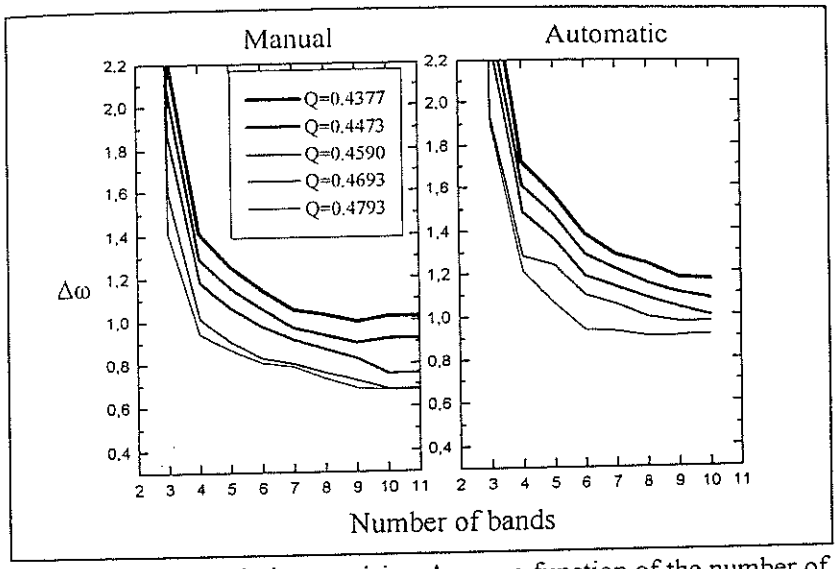

Figure 5.3.4 The relative precision $\Delta\omega$ as a function of the number of EBSP bands used for estimating **X**, for five different masures of the pattern quality Q. The curves have been determined on the basis of 100 EBSPs from partly recrystallized aluminium.

localized manually and automatically. Figure 5.3.4 also shows that the benefit from increasing the number of bands used for estimating **X** above say 8 is relatively small, notably for manually localized bands. When all 10 of the automatically localized bands are used for estimating **X**, the expected uncertainty is seen to be about 0.25° larger than if the bands had been localized manually. The corresponding graphs determined on the basis of the 100 EBSPs from partly recrystallized copper are seen in figure 5.3.5. These graphs display basically the same pattern described above, though the graphs for automatically localized bands have a smaller slope when the number of bands is above 6; i. e. the benefit from using more than 6 to 7 bands for estimating **X** is less distinct for high quality EBSPs (figure 5.3.5) than for EBSPs of lower quality (figure 5.3.4), when the bands are detected automatically. Figure 5.3.5 shows that the highest precision that can be expected for the estimate of **X** is $\Delta\omega \approx 0.75°$ when the estimate is based on

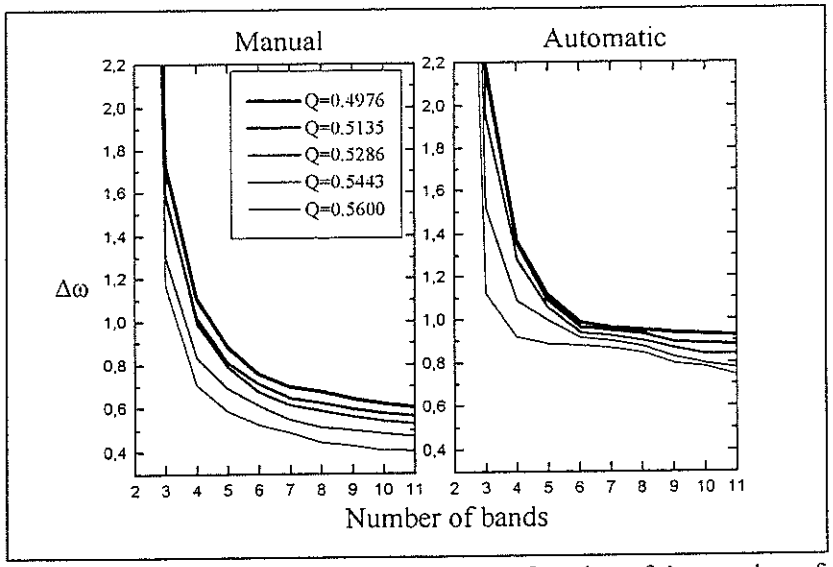

Figure 5.3.5 The relative precision $\Delta\omega$ as a function of the number of EBSP bands used for estimating $\mathbf{X}$, for five different masures of the pattern quality Q. The curves have been determined on the basis of 100 EBSPs from partly recrystallized copper.

the positions of 11 automatically localized bands, and the pattern is of a high quality (Q = 0.56). With an EBSP of similar high quality, the highest precision that can be expected for $\hat{\mathbf{X}}$ is $\Delta\omega = 0.41°$ when the estimate is based on 11 bands, which have been carefully localized by a human operator. These values for the expected relative precision, which reflect the precision of the band positions (including the uncertainties introduced by image distortions) and the uncertainty of the calibration parameters may be regarded as characteristic for our EBSP system when the system has been carefully calibrated. The difference between the relative precision that can be expected for manually and automatically localized bands shows that automatically detected bands are in general less precisely localized than bands positioned by a careful operator. In practice, however, one could hardly expect an operator to carefully point out the positions of 11 bands in each EBSP, due to the extensive amounts of time and patience this would require. If instead the operator could be expected

to carefully localize 3 or 4 bands in each EBSP, the expected precision for $\hat{\mathbf{X}}$ for a high quality pattern (Q = 0.56) would be $\Delta\omega = 1.17°$ and $\Delta\omega = 0.70°$ for 3 and 4 bands respectively. Hence, it may be concluded that for high quality patterns, the relative precision of crystal orientations determined from automatically analyzed EBSPs is similar to the precision that can be obtained when four bands are carefully localized by an operator. Figure 5.3.4 and figure 5.3.5 also shows that the difference between the relative precision obtained for manually and automatically localized bands is slightly smaller for EBSPs of low quality than for EBSPs of high quality. Where the difference in $\Delta\omega$ is typically 0.35° for high quality patterns, the difference is only about 0.20° for patterns of low quality. It may also be observed that for low quality patterns, the relative precision of crystal orientations determined from automatically localized EBSP bands is similar to the precision that can be obtained when five bands are being carefully localized by an operator.

The results presented above illustrate the type of information that can be extracted by performing a statistical analysis of the data $(\mathbf{u}_i,\mathbf{v}_i)$ obtained from EBSPs. This kind of analysis makes it possible to describe the uncertainties $\Delta\omega$ in the estimated rotations $\hat{\mathbf{X}}$ (the relative precision of the measured crystal orientations), study the effects that pattern quality and the number of bands have on $\Delta\omega$, and compare the uncertainties obtained in a fully automated system with those obtained in a semi-automatic system. Furthermore, it would be possible to directly compare the precision $\Delta\omega$ obtained from different image processing procedures used for extracting the bands of EBSPs, or evaluate the possible benefit or drawback of certain changes to the current EBSP system. For example, it would undoubtedly be reflected in the uncertainties $\Delta\omega$, if the current camera system were replaced by a system with no image distortions. It would even be possible, though probably not very useful, to compare the precision of the orientation data collected by different operators. A more useful application of the statistical analysis presented above would be to determine the relative precision $\Delta\omega$ for each EBSP during fully automated EBSP analysis; the calculation of $\Delta\omega$ requires very little computing time. By saving the values for $\Delta\omega$ together with the estimated crystal orientations $\mathbf{g}$, a very good measure of both precision and reliablity is available when the collected orientation data are to be analyzed.

Note, that if the indexing process - for some reason - has failed for one or several bands, this will be observed as a very small value for the estimate $\hat{k}$ (the term $|\mathbf{v}_i - \mathbf{X}\mathbf{u}_i|$ will be abnormally large for an incorrectly indexed band) and a very large value for the uncertainty $\Delta\omega$.

The results presented in this section on the relative precision of crystal orientations determined from EBSPs can not be compared, unfortunately, with other results reported in the literature (Venables & bin-Jaya, 1977; Harland, Akhter & Venables, 1981; Dingley, Longden, Weinbren & Alderman, 1987; Schmidt, Bilde-Sørensen & Juul Jensen, 1991). The values reported for the relative precision in these references are either based on a different definition of the precision concept or based on some, not further specified, definition. With a more widespread employment of statistical methods for analysing orientation data it will become easier, hopefully, to compare results obtained by different research groups in the future.

Chapter 6

Conclusion

The present thesis has described the development, implementation, and performance of an automatic technique for measuring crystallographic orientation with high spatial resolution in polycrystalline materials from electron backscattering patterns (EBSPs). The main results presented in this work will be summarized shortly in the following.

An image recognition procedure which enables the localization of 8 to 12 bands in typical EBSPs has been developed. The procedure is based on the Hough transform and can be implemented in a computationally efficient way. The ability of the procedure to correctly and precisely localize the bands of EBSPs has been demonstrated, even in the case of very low quality patterns.

A fully automatic procedure which determines the indices of the reflected EBSP bands has been described. This indexing procedure is robust in the presence of erroneous band positions and computationally efficient. It allows bands, which have been poorly localized, to be disregarded from further processing.

When a number of the EBSP bands have been automatically localized and indexed, the orientation of the crystal can be determined. A procedure, which allows the orientation of the crystal to be calculated in an optimal (in a least squares sense) way, has been devised. The procedure is not new but seem to be unknown in this scientific area.

The problem of measuring or estimating the calibration parameters of an EBSP set-up is thoroughly discussed in this thesis. A novel calibration

procedure based on the positions and indices of at least four bands or zone axes in an arbitrary EBSP has been developed. The procedure eliminates the need for special calibration specimens or specialized attachments to the EBSP system. The accuracy by which the calibration parameters can be determined with this procedure is shown to be competitive with that of other procedures.

A simple quantitative measure of the quality of EBSPs has been developed. This measure requires very little computation and is shown to agree well with the pattern quality as it is perceived by the human eye. The possibility of applying this measure for automated recognition of deformed and recrystallized areas in partly recrystallized samples has been studied, and promising preliminary results have been obtained. The measure has also been shown to be correlated with the relative precision of the measured crystal orientations.

By combining automated localization and indexing of EBSP bands with a computer-controlled motorized microscope stage, a fully automatic system for measuring the microtexture of polycrystals has been obtained. The reliability and precision of the crystal orientations, which can be collected with such a system, is, of course, of great importance. The reliability of the automatically determined crystal orientations could be defined and measured as the fraction of orientations which has a distance - rotation angle - larger than some given threshold (e. g. 5°) from the manually determined orientations. Such a quantitative analysis of the reliability of the automated system has not yet been performed, since it would require the measurements (both manually and automatically) of a very large number of crystallites. Practical experience with automated measurements, however, has shown the system to be very robust and reliable. The precision of both manually and automatically measured crystal orientations has been thoroughly discussed in this thesis. In particular, results on the relative precision of the estimated crystal orientations have been presented. The use of newly developed statistical methods for analyzing orientation data, has made it possible to compare the precision of manually and automatically measured crystal orientations, as well as studying the effect which the number of bands and the pattern quality has on the precision. Typical values for the relative precision of crystal orientations measured from EBSPs are shown to be of the order of

~0.5° for manually localized bands and ~0.8° for automatically localized bands, when about 10 EBSP bands are used for the measurements. It must, therefore, be concluded that an experienced and careful human operator is able to localize the EBSP bands with a higher precision than the current pattern recognition procedure. In practice, however, the patience and valuable time of the operator limit the number of bands which he or she is willing to localize to less than typically 5. In this more realistic situation, the relative precision of the measured crystal orientations obtained for automatically analyzed patterns is - at least - as good as when the patterns have been analyzed semi-automatically. It may, therefore, be concluded that the automated system described in this thesis is capable of measuring crystal orientations with a precision which compares well with the precision obtained by a typical operator of a semi-automatic system.

References

Alam, M. N., Blackman M. & Pashley, D. W. (1954) High-angle Kikuchi patterns. *Proceedings of the Royal Society* A, **221**, pp.224-242.

Altman, S. L. (1986). *Rotations, Quaternions and Double Groups*, Clarendon Press, Oxford.

Ballard, D. H. (1981). Generalizing the Hough transform to detect arbitrary shapes. *Pattern Recognition*, **13**, pp.111-122.

Ballard, D. H. & Brown, C. M. (1982). *Computer Vision*. Prentice-Hall, London.

Boisen, M. B. & Gibbs, G. V. (1985). *Reviews in Mineralogy Vol. 15: Mathematical Cystallography*. Mineralogical Society of America, Washington.

Brown, C. M. (1983). Inherent bias and noise in the Hough transform. *IEEE Transactions on Pattern Analysis and Machine Intelligence*, **5**, pp.493-505.

Burns, J. B., Hanson, A. R. & Riseman, E. M. (1986). Extracting straight lines. *IEEE Transactions on Pattern Analysis and Machine Intelligence*, **8**, pp.425-455.

Chang, T. (1986). Spherical regression. *The Annals of Statistics*, **14**, pp.907-924.

Chang, T. (1987). On the statistical properties of estimated rotations. *Journal of Geophysical Research* B, **92**, pp.6319-6329.

Chang, T., Stock, J. & Molnar, P. (1990). The rotation group in plate tectonics and the representation of uncertainties of plate reconstructions. *Geophysical Journal International*, **101**, pp.649-661.

Chang, T. (1993). Spherical regression and the statistics of tectonic plate reconstructions. *International Statistical Review*, **61**, pp.299-316.

Cohen, M. & Toussaint, G. T. (1976). On the detection of structures in noisy pictures. *Pattern Recognition*, 9, pp.95-98.

Davies, E. R. (1992). Simple two-stage method for accurate location of Hough transform peaks. *IEE Proceedings-E*, **139**, pp.242-248.

Day, A. (1994). Ph. D. thesis. University of Bristol, in preparation.

Deans, S. R. (1980). Hough transform from the Radon transform. *IEEE Transactions on Pattern Analysis and Machine Intelligence*, 3, pp.185-188.

Deans, S. R. (1983). *The Radon transform and some of its application*. John Wiley & Sons, New York.

Dingley, D. J. (1981). A comparison of diffraction techniques for the SEM. *Scanning Electron Microscopy*, **IV**, pp.273-286.

Dingley, D. J. (1984). Diffraction from sub-micron areas using electron backscattering in a scanning electron microscope. *Scanning Electron Microscopy*, **II**, pp.569-575.

Dingley, D. J. & Baba-Kishi, K. (1986). Use of electron back scatter diffraction patterns for determination of crystal symmetry elements. *Scanning Electron Microscopy*, **II**, pp.383-391.

Dingley, D. J., Longden, M., Weinbren, J. & Alderman, J. (1987). On-line analysis of electron back scatter diffraction patterns. I. Texture analysis of zone refined polysilicon. *Scanning Microscopy*, **1**, pp.451-456.

Downs, T. D. (1972). Orientation statistics. *Biometrika*, **59**, pp.665-676.

Duda, R. D. & Hart, P. E. (1972). Use of the Hough transform to detect lines and curves in pictures. *Communications of the ACM*, **15**, pp.11-15.

Edington, J. W. (1975). *Electron diffraction in the electron microscope*. The Macmillan Press, London.

Fisher, N. I., Lewis, T. & Embleton, B. J. J. (1987). *Statistical analysis of spherical data*, University Press, Cambridge.

Fisher, R. A. (1953). Dispersion on a sphere. *Proceedings of the Royal Society* A, **217**, pp.295-305.

Fischler, M. A. & Bolles, R. C. (1981). Random sample consensus: A paradigm for model fitting with applications to image analysis and automated cartography. *Communications of the ACM*, **24**, pp.381-395.

Goodall, C. (1991). Procrustes methods in the statistical analysis of shape, *Journal of the Royal Statistical Society* B, **53**, pp.285-339.

Golub, G. H. & Van Loan, C. F. (1983). *Matrix computations*. North Oxford Academic, Oxford.

Hanna, M. S. & Chang, T. (1990). On graphically representing the confidence region for an unknown rotation in three dimensions, *Computers and Geosciences*, **16**, pp.163-194.

Harland, C. J., Akhter, P. & Venables, J. A. (1981). Accurate microcrystallography at high spatial resolution using electron back-scattering patterns in a field emission gun scanning electron microscope. *Journal of Physics* E: *Scientific Instruments*, **14**, pp.175-182.

Hjelen, J. (1990). *Teksturutvikling i aluminium, studert ved elektronmikrodiffraksjon (EBSP) i scanning elektronmikroskop*. Dr. Scient. thesis, The Institute of Physics, The university of Trondheim, Norway. pp.139.

Hjelen, J., Ørsund, R., Hoel, E., Runde, P., Furu, T. & Nes, E. (1993). EBSP, progress in technique and applications. *Textures and Microstructures*, **20**, pp.29-40.

Hjelen, J. & Qvale, A. H. (1993). Imaging of electron backscatter diffraction pattern (EBSP) using high resolution imaging technique. *SCANDEM '93*, ed. G. Karlsson, SSEM, Lund, pp.105-106.

Holt, R. J. & Netravali, A. N. (1991). Camera calibration problem: Some new results. *Computer Vision, Graphics and Image Processing: Image Understanding*, **54**, pp.368-383.

Hough, P. V. C. (1962). A method and means for recognizing complex patterns, U.S. Patent 3,069,654.

Humphreys, F. J. (1988). Experimental techniques for microtexture determination. *ICOTOM 8*, Eds. J. S. Kallend and G. Gottstein, TMS, Warrendale, pp.171-182.

Ibrahim, M. K., Ngau, E. C. L. & Daemi, M. F. (1992). Weighted Hough transform. *Journal of the Society of Photo-Optical Instruments and Engineering*, **1607**, pp.237-241.

Illingworth, J. & Kittler J. (1988). A survey of the Hough transform. *Computer Vision, Graphics and Image Processing*, **44**, pp.87-116.

Joy, D. C., Newbury, D. E. & Davidson, D. L. (1982). Electron channeling patterns in the scanning electron microscope. *Journal of Applied Physics*, **53**, pp.R81-R122.

Juul Jensen, D. & Schmidt, N. H. (1990). An automatic on-line technique for determination of crystallographic orientations by EBSP. *Recrystallization '90*, Ed. T. Chandra, TMS, Pennsylvannia, pp.219-224.

Juul Jensen, D. (1993). Automatic EBSP analysis for recrystallization studies. *Textures and Microstructures*, **20**, pp.55-65.

Khatri, C. G. & Mardia, K. V. (1977). The von Mises-Fisher matrix distribution in orientation statistics. *Journal of the Royal Statistical Society* B, **39**, pp.95-106.

Klepeis, S. J., Benedict, J. P. & Anderson, R. M. (1988). *Specimen preparation for transmission electron microscopy of materials*. Eds. Bravman *et al.*, MRS, Pittsburgh, pp.179-184.

Koshimizu, H. & Numada, M. (1991). FIHT2 algorithm: A fast incremental Hough transform. *IEICE Transactions* E, **74**, pp.3389-3393.

Krieger Lassen, N. C., Juul Jensen, D. & Conradsen, K. (1992). Image processing procedures for analysis of electron back scattering patterns. *Scanning Microscopy*, **6**, pp.115-121.

Krieger Lassen, N. C. (1992). Automatic crystal orientation determination from EBSPs. *Micron and Microscopica Acta*, **23**, pp.191-192.

Krieger Lassen, N. C. & Juul Jensen D. J. (1993). Automatic local texture measurements by EBSP. *Materials Science Forum*, **113-115**, pp.679-684.

Krieger Lassen, N. C. & Bilde-Sørensen, J. B. (1993). Calibration of an electron back-scattering pattern set-up. *Journal of Microscopy*, **170**, pp.125-129.

Krieger Lassen, N. C., Juul Jensen, D. & Conradsen, K. (1993). Automatic recognition of deformed and recrystallized regions in partly recrystallized samples using electron back scattering patterns. *ICOTOM 10*, Ed. H. J. Bunge, in press.

Krieger Lassen, N. C., Juul Jensen, D. & Conradsen, K. (1994). On the statistical analysis of orientation data. *Acta Crystallographica* A, accepted for publication.

Kunze, K., Wright, S. I., Adams, B. L. & Dingley, D. J. (1993). Advances in automatic EBSP single orientation measurements. *Textures and Microstructures*, **20**, pp.41-54.

Leavers, V. F. & Sandler, M. B. (1988). An efficient Radon transform. *4th BPRA meeting,* Cambridge.

Leavers, V. F. & Boyce, J. F. (1987). The Radon transform and its application to shape parameterization in machine vision. *Image and Vision Computing*, **5**, pp.161-166.

Leavers, V. F. (1992). *Shape detection in computer vision using the Hough transform*. Springer-Verlag, London.

Leavers, V. F. (1993). Which Hough transform ?. *Computer Vision, Graphics and Image Processing: Image Understanding*, **58**, pp.250-264.

Leung, D. N. K., Lam, L. T. S. & Lam, C. Y. (1993). Diagonal quantization for the Hough transform. *Pattern Recognition Letters*, **14**, pp.181-189.

Maitre, H. (1986). Contribution to the prediction of performances of the Hough transform. *IEEE Transaction on Pattern Analysis and Machine Intelligence*, **8**, pp.669-674.

MacKenzie, J. K. (1957). The estimation of an orientation relationship, *Acta Crystallographica* A, **10**, pp.61-62.

Niblack, W. (1985). *An introduction to digital image processing*. Strandberg, Birkerød.

Niblack, W. & Petkovic, D. (1990). On improving the accuracy of the Hough transform. *Machine Vision and Applications*, **3**, pp.87-106.

Porter, A. J. & Ralph, B. (1983). Recrystallization of a nickel-base superalloy: Kinetics and microstructural development. *Material Science and Engineering*, **59**, pp.69-76.

Prentice, M. J. (1986). Orientation statistics without parametric assumptions. *Journal of the Royal Statistical Society* B, **48**, pp.214-222.

Press, W. H., Flannery, B. P., Teukolsky, S. A. & Vetterling, W. T. (1988). *Numerical Recipes in C, The Art of Scientific Computing*. University Press, Cambridge.

Princen, J., Illingworth, J. & Kittler, J. (1990). Hypothesis testing: A framework for analysing and optimizing the Hough transform performence, *Proc. 3rd Int. Conf. on Computer Vision*, Osaka.

Radon, J. (1917). Über die bestimmung von funktionen durch ihre integralwerte längs gewisser mannigfaltigkeiten. *Berichte Sächsische Akademie der Wissenschaften. Leipzig, Math.-Phys. Kl.*, **69**, pp.262-267.

Randle, V. (1992). *Microtexture Determination and Its Applications*. The Institute of Materials, London.

Risse, T. (1989). Hough transform for line recognition: Complexity of evidence accumulation and cluster detection. *Computer Vision, Graphics and Image Processing*, **46**, pp.327-345.

Rivest, L-P. (1989). Spherical regression for concentrated Fisher-von Mises distributions. *The Annals of Statistics*, **17**, pp.307-317.

Schmidt, N. H. & Olesen, N. Ø. (1989). Computer-aided determination of crystal-lattice orientation from electron-channeling patterns in the SEM. *Canadian Mineralogist*, **27**, pp.15-22.

Schmidt, N. H., Bilde-Sørensen, J. B. & Juul Jensen, D. (1991). Band positions used for on-line crystallographic orientation determination from electron back scattering patterns. *Scanning Microscopy*, **5**, pp.637-643.

Schwarzer, R. A. (1990). Measurement of local textures with transmission and scanning electron microscopes. *Textures and Microstructures*, **13**, pp.15-30.

Troost, K. Z., Van der Sluis, P. & Gravesteijn, D. J. (1993). Microscale elastic-strain determination by backscatter Kikuchi diffration in the scanning electron microscope. *Applied Physics Letters*, **62**, pp.1110-1112.

Van Veen, T. M. & Groen, F. C. A. (1981). Discretization errors in the Hough transform. *Pattern Recognition*, **14**, pp.137-145.

Venables, J. A. & Harland, C. J. (1973). Electron back-scattering patterns - A new technique for obtaining crystallographic information in the scanning electron microscope. *Philosophical Magazine*, **27**, pp.1193-1200.

Venables, J. A. (1976). *Developments in electron microscopy and analysis*, Ed. J. A. Venables, Academic Press, pp.23.

Venables, J. A. & bin-Jaya, R. (1977). Accurate microcrystallography using electron back-scattering patterns. *Philosophical Magazine*, **35**, pp.1317-1332.

Watson, G. S. (1983). *Statistics on spheres*. Wiley, New York.

Watson, G. S. (1989). Statistics of rotations. *Probability measures on groups IX, Lecture notes in mathematics*, Ed. H. Heyer, Springer-Verlag, Berlin, pp.398-413.

Wilkinson, A. J. & Dingley, D. J. (1991). Quantitative deformation studies using electron back scatter patterns. *Acta Metallurgica et Materialia*, **39**, pp.3047-3055.

Wood, A. T. A. (1993). Estimation of the concentration parameters of the Fisher matrix distribution on SO(3) and the Bingham distribution on S_q, $q \geq 2$. *Australian Journal of Statistics*, **35**, pp.69-79.

Wright, S. I., Zhao, J. & Adams, B. L. (1991). Automated determination of lattice orientation from electron backscattered Kikuchi diffraction patterns. *Textures and Microstructures*, **13**, pp. 123-131.

Wright, S. I. & Adams, B. L. (1992). Automatic Analysis of Electron Backscatter Diffraction Patterns. *Metallurgical Transactions* A, **23**, pp.759-767.

Young, C. T. & Lytton, J. L. (1972). Computer generation and identification of Kikuchi projection. *Journal of Applied Physics*, **43**, pp.1408-1417.

Yuen, S. Y. K. & Hlavac, V. (1991). An approach to the quantization of Hough space. *7th Scandinavian conference on image analysis*, pp.733-740.

Ph. D. theses from IMM

1. Rasmus Larsen. (1994). *Estimation of visual motion in image sequences.* 143 pp.
2. Jens Moberg Rygaard. (1994). *Design and optimization of flexible manufacturing systems.* 232 pp.
3. Niels Christian Krieger Lassen. (1994). *Automated determination of crystal orientations from electron backscattering patterns.* 136 pp.